UNIVERSITÉ DU QUÉBEC À MONTRÉAL

ON THE LARGE SCALE CONTROL MECHANISMS OF ARCTIC SEA ICE AND PERMAFROST USING REGIONAL CLIMATE MODELS

THESIS

PRÉSENTED

AS PARTIAL REQUIREMENT

FOR PHD DEGREE IN EARTH AND ATMOSPHERIC SCIENCES

BY

JEAN-PHILIPPE PAQUIN

JANUARY 2014

UNIVERSITÉ DU QUÉBEC À MONTRÉAL

ÉTUDE DES MÉCHANISMES DE GRANDE ÉCHELLE INFLUENÇANT LA GLACE DE MER ARCTIQUE ET LE PERGÉLISOL À L'AIDE DE MODÈLES RÉGIONAUX DE CLIMAT

THÈSE

PRÉSENTÉE

COMME EXIGENCE PARTIELLE

DU DOCTORAT EN SCIENCES DE LA TERRE
ET DE L'ATMOSPHÈRE

PAR

JEAN-PHILIPPE PAQUIN

JANVIER 2014

REMERCIEMENTS

Je tiens à remercier tout d'abord ma directrice de thèse, Laxmi Sushama. L'accomplissement de ce travail de recherche n'aurait pu être possible sans son support au cours des cinq dernières années. Un merci spécial à mes collaborateurs suédois Ralf Döscher et Torben Königk ainsi que l'ensemble de l'équipe du Centre Rossby qui, malgré un océan de distance, ont toujours trouvé le temps de m'épauler dans mes recherches sur l'océan et la glace de mer.

D'autres professeurs et collègues chercheurs ont aussi contribué par les nombreuses discussions constructives au succès de ce travail, en particulier : Bruno Tremblay, Michelle Garnaud, Richard Harvey, Colin Jones, Bernard Dugas et, bien évidemment, René Laprise.

Le travail présenté dans cette thèse n'aurait pu être accompli sans le support de Katja Winger qui a toujours su prendre le temps de m'aider avec les nombreux défis techniques que représente l'utilisation du MRCC5 et le développement d'un nouveau paramétrage. Je voudrais aussi remercier les autres membres de l'équipe de soutien et d'enseignement de l'UQAM : Eva Monteiro, Georges Huard, Nadjet Labassi, Adelina Alexandru et Delphine Person.

Le travail et la vie à l'UQAM n'auraient été aussi agréables sans la présence de nombreux collègues, rapidement devenus amis et parfois même confidents. Je vous salue et vous remercie, vous tous, et plus particulièrement Danahé et Marko pour votre soutien quand le ciel était moins bleu mais surtout pour tous les bons moments que nous avons passés ensemble au cours de ces nombreuses années… et aussi pour les années à venir!

Je voudrais remercier ma famille, toujours présente pour m'encourager et me soutenir dans ce projet ambitieux qu'est le doctorat. Finalement, un merci sans mesure à ma

conjointe, Isabelle, pour son soutien indéfectible tout au long des années et pour avoir accepté de vivre avec moi notre prochaine expérience de Vie à Halifax!!!

Quoique l'UQAM soit une institution de langue française, cette thèse est essentiellement présentée en anglais afin d'élargir le bassin de lecteurs et de réviseurs externes. Je présente mes sincères excuses aux lecteurs de cet ouvrage pour qui ce pourrait être problématique.

TABLE OF CONTENT

LIST OF FIGURES

LIST OF TABLES

LIST OF ACRONYMS

ACIA	Arctic Climate Impact Assessment
AIDJEX	Arctic Ice Dynamics Joint Experiment
ALT	Active Layer Thickness
AO	Arctic Oscillation
AOGCM	Coupled Atmosphere-Ocean General Circulation Model
CAA	Canadian Arctic Archipelago
CALM	Circumpolar Active Layer Monitoring programme
CAM	Community Atmospheric Model
CCSM	Community Climate System Model
CLASS	Canadian Land Surface Scheme
CLM	Community Land Model
CMC	Canadian Meteorological Centre
CMIP	Coupled Model Intercomparison Project
CORDEX	COordinated Regional Downscaling Experiment
CRCM5	Fifth-generation of the Canadian Regional Climate Model
CRU	Climatic Research Unit
DDF	Degree-day freezing index
DDT	Degree-day thawing index
EOF	Empirical Orthogonal Functions
ERA	European Re-Analysis
GPCC	Global Precipitation Climatology Center
IGBP-DIS	International Geosphere-Biosphere Progamme Data Information System
IPA	International Permafrost Association
IPCC	Intergovernmental Panel on Climate Change
JULES	Joint UK Land Environment Simulator
LBC	Lateral boundary condition
LHF	Latent heat flux
LSM	Land Surface Model
MRCC5	Modèle Régional Canadien du Climat de cinquième génération
NAM	Northern Annular Mode

NAO	North Atlantic Oscillation
NSIDC	National Snow and Ice Data Center
OHT	Ocean heat transport
PHC	Polar science center Hydrographic Climatology
RCA	Rossby Centre Atmospheric model
RCAO	Rossby Centre Atmosphere-Ocean
RCM	Regional Climate Model
RCO	Rossby Centre Ocean model
RILE	Rapid Ice Loss Event
SHF	Sensible heat flux
SIC	Sea ice cover
SLP	Sea level pressure
SMHI	Swedish Meteorological and Hydrological Institute
SOC	Soil organic content
SST	Sea surface temperature
SWE	Snow water equivalent
T2M	2 m-air temperature
UDel	University of Delaware
WCRP	World Climate Research Program

RÉSUMÉ

La complexité des processus physiques et les nombreuses rétroactions entre les différentes composantes du système climatique présentent des défis particuliers à la simulation du climat arctique. Cette thèse propose d'approfondir certains aspects du climat de l'Arctique avec une attention particulière sur les interactions et les rétroactions entre les composantes majeures du système climatique de l'Arctique et comment celles-ci sont influencées par le changement climatique. En premier lieu, un analyse détaillée des mécanismes physiques responsables de la simulation d'évènements de perte rapide de la glace de mer, *i.e.* une diminution abrupte de la couverture de glace de mer en septembre, est effectuée pour trois projections climatiques effectuées par le Modèle Régional Atmosphère-Océan du Centre Rossby (RCAO). Deux processus importants, agissant à différentes échelles temporelles, sont identifiés comme responsables de la simulation de tels évènements, soit la diminution progressive de l'épaisseur de la glace de mer qui a pour effet de rendre la glace de mer plus vulnérable à la fonte et la présence d'anomalies dans le transport de chaleur atmosphérique et océanique au-dessus du secteur Atlantique de l'Océan Arctique. Notre analyse démontre que la propagation d'une anomalie importante dans la circulation atmosphérique de grande échelle à partir de la frontière latérale située dans l'Atlantique est responsable de la synchronisation des évènements autour de 2040 se produisant dans chacune des trois projections climatiques effectuées avec RCAO. Cette anomalie de circulation a pour origine les champs atmosphériques provenant d'une projection climatique unique d'un MCCG utilisée comme données de pilotage pour toutes les projections de RCAO. Au-dessus du Secteur Pacifique de l'Océan Arctique, une anomalie dans le transport de la glace de mer, poussant la glace de la côte de l'Alaska vers le centre de la mer de Beaufort provoque une rétroaction positive glace de mer-albédo (*Sea ice-albedo feedback*) favorisant une fonte plus prononcée de la glace durant la même période.

Le second aspect traité dans cette thèse a pour objectif d'évaluer la sensibilité des régimes thermiques et hydrauliques du sol des continents bordant l'Arctique, donc par conséquent le pergélisol, à la formulation du modèle et de la neige ainsi que leur impacts sur le climat de surface en Arctique. Plus précisément, nous évaluons la sensibilité des régimes thermiques et hydrauliques du sol à la configuration verticale et la profondeur totale de la colonne de sol, à l'ajout d'un paramétrage pour la représentation de la matière organique ainsi que différentes formulations de la relation entre la conductivité thermique et la densité de la neige à l'aide d'expériences en mode non-couplé du schéma de sol Canadian LAnd Surface Scheme (CLASS). Les résultats démontrent des améliorations successives de la simulation de la température du sol résultant de l'augmentation de la profondeur totale de la colonne de sol, de l'implémentation du paramétrage de la matière organique du sol ainsi que d'une diminution de la conductivité thermique de la neige. Les effets de ces améliorations apportées au schéma de sol sur le climat simulé, en particulier sur le bilan énergétique de surface, sont analysés plus en profondeur à l'aide d'expériences effectuées avec le Modèle Régional Canadien du Climat de cinquième génération (MRCC5). L'implémentation du paramétrage de la matière organique du sol a pour effet en augmentation marquée des flux de

chaleurs sensible et latente dont les proportions respectives sont fonctions de la disponibilité de l'humidité du sol et du niveau de saturation. Quoique les différences obtenues dans les flux turbulents de surface soient statistiquement significatives, peu de changements sont notés dans le climat de surface au-dessus des régions couvertes par du pergélisol continu ou discontinu. Les résultats du MRCC5 montrent que la variabilité interannuelle de la couche active du sol (CAS; *i.e.* la profondeur de dégel maximale annuelle) est directement liée aux variations de la température de l'air en surface et montre une dépendance annuelle. La surestimation de la profondeur de la CAS est fort probablement causée par la présence de biais chauds observés dans la climatologie simulée du MRCC5 puisque les tendances simulées ne montrent pas de différences significatives avec celles des observations.

Mots-clés :

Modèles régionaux de climat, Arctique, glace de mer, pergélisol

ABSTRACT

The climate simulation of the Arctic region presents distinct challenges because of the complexity of processes and feedbacks between the various components of the climate system. This thesis focuses on understanding some selected aspects of the Arctic climate, particularly the interactions and feedbacks between the major components of the Arctic climate system and how they are affected by climate change. To this effect, firstly, the physical mechanisms responsible for the Rapid Ice Loss Events (RILEs), i.e. the abrupt reduction of the September sea ice cover, in the Rossby Centre Ocean-Atmosphere (RCAO) regional climate model simulations are investigated. Two major processes, occurring at different timescales, are found responsible for the RILEs in the three RCAO climate projections considered in this study: the long-term thinning of the sea ice leading to increased vulnerability of the ice cover, and the anomalous atmospheric and oceanic heat transport through the Atlantic Sector of the Arctic Ocean. Investigation across the three RCAO projections reveals that a strong large-scale atmospheric circulation anomaly originating from the driving GCM realization propagating through the Atlantic lateral boundary of the regional model is responsible for the synchronicity of the simulated RILEs around 2040. Over the Pacific Sector of the Arctic Ocean, anomalous sea ice drift from the Alaska coast towards the Beaufort Sea triggers a sea ice-albedo feedback leading to increased sea ice melt over the same period.

The second major aspect investigated in this thesis is the sensitivity of the Arctic soil thermal and moisture regimes over the continental areas surrounding the Arctic Ocean, and therefore near-surface permafrost, to soil and snow formulations in land surface models and their impact on the surface climate. More precisely, the sensitivity of the soil thermal and moisture regimes to soil layer configuration and depth, representation of soil organic carbon (organically rich soils) and snow conductivity formulation are explored in stand-alone simulations with the Canadian LAnd Surface Scheme (CLASS). Results showed major improvements of the simulated soil temperatures and a reduction of the annual maximum thawing depth with deeper soil model, representation of soil organic carbon and modified snow thermal conductivity. The impact of the above improvements on the surface climate, particularly surface energy partitioning, is further investigated using the fifth-generation of the Canadian Regional Climate Model (CRCM5). The implementation of the soil organic carbon increases both latent and sensible heat fluxes, as function of the available soil moisture and saturation level. Despite statistically significant changes in the surface energy partitioning, little significant changes were noted in the surface climate over the continuous and discontinuous permafrost region. The inter-annual variability of the active layer thickness (ALT; i.e. the maximum annual thaw depth) within the CRCM5 experiments is found tightly linked with the surface air temperatures and shows yearly dependence. The overestimation of the simulated ALTs is likely caused by a warm bias noted in the CRCM5 surface climate, while simulated trends in surface climate are not significantly different from those observed.

Key words:

Regional climate model, Arctic, sea ice, near-surface permafrost

INTRODUCTION

> *"The Arctic biological, climatologic, hydrologic subsystems and their thermal regimes are fully coupled and cannot be completely understood or isolated individually. (...) No single piece of the system is independent, and to fully understand even a part of the system, we need to understand the whole."*
>
> – Hinzman et al. (2005)

General context

In the past decades, the Arctic climate has shown some undeniable signs of change. The Arctic average annual temperatures have already risen by about 2 °C to 3 °C since the 1950s and the winter temperatures by up to 4 °C (ACIA 2004) with a more pronounced warming over land (Chapman and Walsh 2007). Although large inter-annual to inter-decadal variability in temperatures is present in the Arctic (ACIA 2004), significant part of the warming in the Polar Regions was attributed to human influence (Gillett et al. 2008).

The Arctic region is expected to warm strongly as a result of the anthropogenic climate change, mainly due to the positive feedbacks associated with a decrease of the surface albedo caused by the shrinking snow and ice cover. Climate change projections realized with coupled atmosphere-ocean general circulation models (AOGCMs) for the 21st Century suggest maximum warming for the Arctic region (IPCC AR4 2007; ACIA 2004). Although all models agree on the warming of the Arctic, large uncertainties remains as can be seen in the large spread amongst the individual model projections (ACIA 2004).

Understanding the environmental conditions in the Arctic is a non-trivial task. The isolated location and rigorous climate pose supplementary challenges for observational study of the climate and the environment. A growing interest exists to understand the Arctic climate and its interactions with the different ecosystems. The Arctic countries are also interested in the evolution of the Arctic climate to assure the protection of its unique habitats or for economic development. The economic development might threaten the unique and fragile ecosystems of the region. Therefore, the scientific community strongly recommends that

more research be conducted to insure a durable exploitation of the natural resources of the Arctic, with limited success until now.

Studying the Arctic climate is challenging due to the presence of large natural variability combined with the effects of increased greenhouse gases concentration due to human activity. The combination of both signals and the limited availability, both in space and time, of *in-situ* observations of the Arctic pose problems and therefore the numerical modelling approach offers some advantages.

The overall goal of this thesis is to address some uncertainties in the actual understanding of different aspects of the Arctic climate, namely the Rapid Ice Loss Events and the evolution and sensitivity of near-surface permafrost. The main tools used for this are Regional Climate Models (RCM) and observation datasets where available. A brief description of the Arctic climate components, their interactions and representation in climate models is given below to better understand the context in which these studies were performed.

The Arctic climate system

The most fundamental characteristic of the Arctic is the 24-hour summer daylight or winter darkness with the number of days in these extremes increasing with latitude (Serreze and Barry 2005). The geographical configuration of the Arctic region is characterized by a central ocean, nearly enclosed by the continental masses of North America and Eurasia (Fig. I.1), reducing the oceanic exchanges with the lower latitudes. The multiple interactions between the atmosphere, land and ocean make the Arctic an interesting but challenging region to study.

The Arctic Ocean covers significant area of the northern hemisphere high latitudes and plays a major role in defining the Arctic climate. The main singularity of the Arctic Ocean compared to the other oceans of the world is the presence of sea ice and its variability. The sea ice greatly affects the surface heat and moisture exchanges between the ocean and the atmosphere due to its important insulating properties, thereby modulating the climate (Washington and Meehl 1996). Due to the high albedo of the sea ice and snow compared to

open water, sea ice also acts as a reflective barrier limiting the absorption of incoming solar energy within the Arctic climate system (Peixoto and Oort 1992). Since sea ice is sensitive to changes in the ocean and the atmosphere temperatures, it acts as a good proxy of the variability in the thermal state of the region. The Arctic sea ice not only affects the atmospheric boundary layer by modulating the energy exchanges, it also has an impact on the ocean near-surface stratification. Indeed, the sea ice formation and melt affect the ocean surface layer stratification by the release of brine and freshwater, respectively, modulating the water density in the ocean surface layer (Serreze and Barry 2005).

The ocean surface currents and sea ice motion are dependent on the near-surface winds and therefore the regional atmospheric circulation and its variability (Rigor et al. 2002). The atmospheric large-scale circulation in the Arctic is characterized by three centers of action: the Icelandic Low, the Aleutian Low and the Siberian High with its extension into the Arctic (Beaufort High). The variability in the intensity of these centers of actions has an important influence not only on the near-surface circulation, but also on the poleward transport of heat and moisture from the lower latitudes (Hurrell et al. 2003). Sea ice distribution in the Arctic Ocean is also a direct consequence of the near-surface winds, with ice convergence leading to thicker ice along the Canadian Arctic Archipelago (Bourke and Garret 1987) and important sea ice exports through Fram Strait (Kwok and Rothrock 1999; Dickson et al. 2000; Hilmer and Jung 2000; Dickson et al. 2007; Condron et al. 2009; Wang et al. 2009; Tsukernik et al. 2010). The sea level pressure patterns exhibit large inter-annual to inter-decadal variability. The dominant patterns of variability are commonly know as the North Atlantic Oscillation (NAO), the Arctic Oscillation (AO) or the Northern Annual Mode (NAM), depending on the region over which the empirical orthogonal function analysis (EOF) is performed. The EOF analyses are used to extract the dominant modes of variability of the sea-level pressure over the high latitudes. Although there are some limitations in the physical interpretation of such mathematically derived patterns (Tremblay 2001; Hurrell et al. 2003), the EOF analysis showed great capability in relating to physical mechanisms of the Arctic variability, through changes in the sea ice motion (Karcher et al. 2005) and the variability of the second EOF pattern, the dipole anomaly, strongly correlated with the sea ice exports through Fram Strait (Wang et al. 2009), surface temperature anomalies over land (Hurrell et al. 2003), summer cyclone activity in the Nordic Seas and in the Central Arctic (Serreze and Barrett 2008;

Simmonds et al. 2008), precipitation over the Arctic region (Peterson et al. 2006), the freshwater content of the Beaufort Gyre (Proshutinsky et al. 2009; Condron et al. 2009), the river discharge in the Arctic (Peterson et al. 2002) and the observed salinity of the Siberian shelves (Steele and Ermold 2004).

The northern portion of the continental masses of North America and Eurasia are characterized by low vegetation with a marked latitudinal gradient from the Boreal forest in the southern part of the Arctic land, towards tundra in the northernmost latitudes and along the Arctic coastal regions. The limited annual-mean solar radiation, cold temperatures and small amount of annual precipitation act as limiting factors for the growth of vegetation.

Due to the cold temperatures in the Arctic, permafrost – defined as ground that stays frozen for 24 consecutive months – covers approximately one quarter of all the exposed land of the Northern Hemisphere (Zhang et al. 1999). The presence of permafrost affects significantly the hydrology by limiting the soil infiltration capacity, thereby directly influencing the drainage system. Soil temperatures, hence permafrost, are sensitive to changes in the near-surface air temperatures and snow cover and, as for sea ice, act as a good proxy to study the long-term changes in the climate.

Observed climate variability and climate change in the Arctic

This section briefly describes the climate variability and the observed climate change in the Arctic region. The limited availability of observations in time and space, especially before the satellite era, makes the analysis of such observational data a challenge, since the signals of inter-annual variability and climate change are combined in most of the available time series. Nevertheless, clear signs of accelerated changes were observed over the recent years and some of the important findings are briefly summarized here.

The September Arctic sea ice cover has shown significant reduction trends with estimates of –12.9% per decade over the 1976–2006 period (Stroeve et al. 2012). Minimum historical September sea ice cover were observed in 2007, 2011 and 2012, showing an acceleration in the sea ice cover decline over the Arctic (Comiso et al. 2008; NSIDC). More importantly, sea ice thickness and volume have been rapidly decreasing over the past decades

(Kwok and Rothrock 2009; Kwok et al. 2009), as seen also in the marked decrease in thick perennial sea ice volume since the 2000s (Nghiem et al. 2007). The anomalous sea ice motion responsible for Fram Strait ice exports is primarily driven by sea-level pressure anomalies (Tsukernik et al. 2010) illustrating the strong physical coupling between the sea ice and the atmosphere. Although large-scale atmospheric anomalies and upward trend in the NAM index play a role in the sea ice cover reduction, they cannot account entirely for the recent trends (Deser and Teng 2008).

Different mechanisms are responsible for the decrease in sea ice for different regions of the northern hemisphere high latitudes. The changes in the sea ice edge location over the Barents Sea are related to an increase in the sea surface temperatures (SSTs) combined with enhanced southerly winds, while changes over the Bering Sea are mainly influenced by the anomalies in the easterly winds (Francis and Hunter 2007). Over the Pacific Sector of the Arctic Ocean, detailed analysis of the September 2007 sea ice cover minimum showed enhanced heat transport through Bering Strait (Woodgate et al. 2010) likely causing early melt along the Alaska coast and triggering a sea ice-albedo feedback. Reduced cloudiness over the region enhanced the ocean absorption of solar radiation in 2006–2007 (Kay et al. 2008), increasing the heat content of the ocean and energy used for bottom melting of the ice. These complex physical mechanisms and interactions are difficult to assess solely based on observations due to their limited availability, especially for ocean and sea ice. Nevertheless, Perovich et al. (2008), using ice mass balance buoy observations, showed large amounts of bottom melting of the sea ice in the Beaufort Sea in the summer of 2007, directly linked to the increased heat content of the ocean caused by enhanced absorption of solar radiation. Over the Central Arctic Ocean, sea ice cover reduction is responsible for a surface-based amplification of the lower tropospheric warming over the 1989–2008 period (Serreze et al. 2009; Screen and Simmonds 2010). This Arctic amplification due to sea ice retreat is another illustration of positive feedbacks enhancing the warming and further reducing the sea ice cover.

The combination of observational evidence on the recent sea ice cover and thickness suggests a growing non-linear response of sea ice cover and volume to external climate forcing (Fig. I.2). With the extensive open water observed in recent Septembers, the Arctic

Ocean shows increasing proportion of thin first-year ice in spring (Maslanik et al. 2007). The dynamical forcings acting on the ice by the winds, the ocean circulation and waves more effectively break the thinner first-year ice, leading to a more fragmented sea ice cover early in spring. This increased fraction of open water allows for more shortwave radiation to be absorbed at the ocean's surface, thus warming the upper ocean water, increasing the sea ice melt from at the ocean-ice interface during spring and summer. These interactions, supported by observational evidence, strongly suggest an increased contribution of the sea ice-albedo feedback in the recent years minimum observed in the sea ice cover and accelerated rate of decline (Lindsay and Zhang 2006; Perovich et al. 2007, 2008). Finally, as the Arctic climate has been warming for all seasons (Serreze et al. 2009), the likelihood of cold conditions is diminished. These warmer conditions decrease the possibility of temporary recovery of the sea ice cover and thickness through natural climate variability (Stroeve et al. 2012).

Over land, the permafrost temperatures have increased by up to 3 °C since the 1980s in the Arctic (Lemke et al. 2007). Large spatial variability of the warming is observed across the Arctic from maximal increases of 3 °C to 4 °C in the coastal area of Alaska, to smaller increases between 0.3 °C to 1 °C in the Yukon River valley (Osterkamp 2007). Across the Arctic, permafrost temperatures generally increased with the exception of Northern Québec sites that showed cooling of the order of -0.05 °C yr^{-1} from the mid 1980s to early 1990s (Allard et al. 1995), in good agreement with surface temperature changes. Despite the cold annual temperatures in the Arctic, some regions, especially in Alaska, showed signs of permafrost degradation clearly visible from aerial photographs (Jorgenson et al. 2006). Observational studies demonstrated that permafrost temperatures are primarily sensitive to changes in the near-surface air temperature and in the length of the freeze and thaw seasons, while snow cover and duration play an important but secondary role (Zhang et al. 2007; Lemke et al. 2007; Frauenfeld and Zhang 2011).

The impacts of near-surface permafrost degradation are manifold. The thawing of ice-rich permafrost – where large fraction of the soil volume is occupied by ice – causes subsidence of the soil surface, dramatically changing the landscape. The thawing of ice-rich permafrost can lead to the formation of thermokarst ponds, which has impacts on the vegetation cover by flooding the roots and destroying the trees, transforming forested areas

into bogs (Hinzmann et al. 2005).

Permafrost degradation can also dramatically change the surface and sub-surface hydrology. Ice-rich permafrost prevents the infiltration of surface waters, increasing the surface soil moisture. If the permafrost degrades, soil water can in some cases infiltrate and reach the groundwater network causing partial or complete drainage of lakes (Yoshikawa and Hinzmann 2003; Smith et al. 2005). Drying of lakes and ponds changes the redistribution of surface energy from latent to sensible heat fluxes and thus feedback on the near-surface atmospheric conditions.

Rivers can also be affected by the changes in air temperature, precipitation and permafrost degradation. Over the 1936–1999 period, Peterson et al. (2002) showed a 7% increase in the river discharge from the six largest rivers across the Arctic. The increased discharge was related to the changes in the NAO and to the global temperature increase, showing the interdependence and complexity of the Arctic climate system response to changes in the natural variability and the anthropogenic climate change. Inconsistencies between the changes in river discharge and in precipitation raised questions about the quality of the observed fields, especially for the Yenisey River where the increased discharge could not be explained by the observed decrease in precipitation (Berezovskaya et al. 2004). Such inconsistencies are difficult to ascertain solely based on observations due to the limited networks of precipitation gauges and the quasi-absence of reliable data on other hydrologic parameters such as the evaporation, available only at some few measured stations and subject to large uncertainties in model estimates. Moreover, important regional differences exist in river discharge trends across the Arctic, with upward trends over Siberia, while North American Rivers show downward trends in the Hudson Bay region (McClelland et al. 2006; Déry and Wood 2005; Déry et al. 2005; Déry et al. 2009). Changes in the river discharge are also sensitive to the accelerated glacier melt occuring in the high latitudes. As such, river basins with an important glacial component generally show positive trends in runoff while basins with smaller or no glaciers generally show decreasing trends (Hinzmann et al. 2005). Finally, changes in river discharge might also affect the Arctic Ocean by changing the freshwater fluxes and its spatial distribution into the surface layer of the ocean, thereby changing the water density, which is just another illustration of the potential feedbacks

between the different climate components (Peterson et al. 2006).

Soil biological processes are also sensitive to changes in the atmosphere and soil temperatures and to permafrost degradation. In the Arctic, cold temperatures inhibit the decomposition of dead vegetation, forming over time important peat deposits, reaching depths of over 30 m in some cases (Tarnocai et al. 2009). This accumulation results in the presence of large amounts of carbon sequestered in the Arctic soils, evaluated at ~1672 Pg of carbon, with approximately 88% of that carbon located in perennially frozen soils and deposits (Tarnocai et al. 2009). While frozen, this carbon is relatively inactive but represent one of the least understood but important potential carbon-climate feedbacks because of the magnitude of the carbon pool it represents (Schuur et al. 2008). Since most of the microbial activity occurs in the seasonally thawed active layer (Schuur et al. 2008), increases in temperatures and permafrost degradation will increase the decomposition of the soil organic carbon, released in carbon dioxide or methane form depending on the type of decomposition, i.e. aerobic or anaerobic. The carbon transfer from the soil carbon pool towards the atmosphere is dependent on many factors, with the changes in the soil temperatures playing a primary role (Schuur et al. 2008; O'Connor et al. 2010).

In summary, the Arctic Climate and its changes are composed of complex interactions and feedbacks between most of its components. Although the major interactions present between the atmosphere, ocean and land components are mostly addressed by the physics of climate, the understanding of local scale feedbacks requires a multidisciplinary approach involving hydrology, glaciology and biology.

The main challenge in the study of the Arctic climate and climate changes resides in the limited observational networks and the short time period for which these observations are available. Prior to the satellite era, the observational data was mostly available from few long-term stations dispersed in the Arctic region or through field campaigns such as the Arctic Ice Dynamics Joint Experiment (AIDJEX) campaign in the 1970s and the Russian North Pole Drifting Station program. The combination of a sparse observational dataset and high variability makes it difficult to distinguish between the signals of climate variability and climate change with confidence (ACIA 2004).

In this context, the development of numerical models significantly aided comprehension of the key physical processes and mechanisms that determine the Arctic climate. An important advantage of the modeling approach over direct observations is that it provides continuous data in space and time of physically coherent variables essential to study the evolution of various components of the climate system. Although numerical models were traditionally developed separately for various major climate components such as ocean and sea ice, atmosphere, land surface, more efforts are now being dedicated to the interactive coupling of these components to better understand the interlinkages and feedbacks.

Scientific objectives and thesis presentation

This thesis is composed of two main chapters, each representing a paper accepted or submitted for publication in a peer-reviewed journal. The first chapter, entitled "Causes and consequences of mid-21st Century Rapid Ice Loss Events simulated by the Rossby Centre Regional Atmosphere-Ocean model" published in Tellus A, is an analysis of the factors and mechanisms responsible for the Rapid Ice Loss Events (RILEs) as simulated in three climate projections of the regional model from the Swedish Meteorological and Hydrological Institute (SMHI). The second chapter, entitled "On the simulated Arctic near-surface permafrost and climate sensitivity to soil and snow formulations" focuses on the evaluation of the near-surface permafrost and its sensitivity to the representation of soil organic carbon, soil column depth and snow thermal conductivity using a physically based land surface scheme and a regional climate model – the fifth-generation of the Canadian Regional Climate Model (CRCM5). These studies are part of a larger effort at the Centre ESCER (Étude et Simulation du Climat à l'Échelle Régionale) at Université du Québec à Montréal (UQAM) to develop a fully coupled regional climate model that will include, in the future, all physical components of the Arctic Climate system. Work is underway by colleagues at ESCER to develop and implement a lake-river system, dynamic glacier model and to achieve an coupled atmosphere-ocean system. A brief introduction and motivation for each of the chapters is presented below.

As presented earlier, Rapid Ice Loss Events (RILEs) were observed in 2007, 2010 and 2012, mainly occurring over the Pacific Sector of the Arctic Ocean. The AOGCMs

participating in the World Climate Research Programme (WCRP) Coupled Model Intercomparison Project Phases 3 and 5 (CMIP3, CMIP5) underestimate the observed decreasing trends in sea ice cover (Stroeve et al 2007, 2012). Although improvements in the representation of the sea ice cover were achieved in CMIP5, the models do not appear to agree on when the Arctic Ocean might become seasonally ice-free (Stroeve et al. 2012). In some models, the simulated transition from perennial sea ice cover to nearly ice-free summers occurs in an abrupt and short transition period. During these transition periods, the simulated decreasing trends in summer sea ice cover are similar to the observed trends over the past decade. Amongst the CMIP models, only few models show such RILEs, but usually around the middle of the 21st Century (i.e. Holland et al. 2006), while trends over the recent decade are generally underestimated. Understanding the physical mechanisms leading to such RILEs could improve our understanding of the sea ice decline of the last decade and is necessary for climate model improvements. In the context of future climate projections, the state of the Arctic Ocean sea ice cover will play a major role in defining the climate change of the region, and it is essential to understand its interconnections to the global climate in order to reduce the uncertainties associated with future projections.

In that context, the Rossby Centre Atmosphere-Ocean (RCAO) regional climate model is one of the few models to simulate such RILEs. Three climate projections were performed over the 1960–2080 period driven at the atmospheric lateral boundary conditions (LBC) by the same realization of the Max Planck Institute's AOGCM ECHAM5-MPI/OM. Results showed sea ice loss events occurring around 2040 in each projection, although no RILEs were present in the ECHAM5-MPI/OM projection. The common LBCs and the noted synchronicity between the events in each projection allowed an in-depth study of the physical mechanisms causing the events, as well as the role played by the external forcing imposed at the LBCs of the RCM.

The rapid decrease of sea ice cover could also have important potential impacts on other parts of the Arctic climate system. Sea ice thinning and melt could enhance the heat transfer from the ocean towards the atmosphere especially in autumn due to a later freeze-up at the ocean's surface. This increased heat and moisture in the atmosphere could potentially be advected over land, therefore increasing the energy transfers between atmosphere and

land. Lawrence et al. (2008) noted that the CRUTEM3 temperature data (Jones et al. 2006) in autumn of 2007 was the warmest over the previous 30 years with a significant increase of 2.3 °C over Western Arctic. Using the Community Climate System Model (CCSM3; Meehl et al. 2006), Lawrence et al. (2008) also noted that the simulated warming trend over land, in consequence to RILEs, was 3.5 times larger in transient climate change projections compared to periods outside of rapid ice loss. This warming signal propagated approximately 1,500 km inland, influencing the permafrost on a pan-Arctic scale. Complementary experiments using the Community Land Model (Oleson et al. 2008) showed acceleration of soil heat accumulation during RILEs, directly influencing the warm permafrost areas and hastening the permafrost degradation.

Due to some limitations in RCAO representation of near-surface atmospheric variables, especially over land (see section 1.4.3.3) and its shallow 2.2 m deep land surface scheme (Samuelsson et al. 2006), it was decided to investigate the simulation of near-surface permafrost using the fifth version of the Canadian Regional Climate Model (CRCM5) coupled to the Canadian LAnd Surface Scheme (CLASS). CLASS provided important advantages to study permafrost as its formulation includes a flexible soil column depth capability, crucial to represent high latitude soil processes. Although the CRCM5 isn't coupled with an ocean model, it is planned to include such capability in the near future, therefore motivating this study. Moreover, the first simulation results using the CRCM5 undeniably showed the necessity to improve high latitude soil representation due to an underestimation of simulated near-surface permafrost using CLASS standard configuration.

The objective of the second paper is therefore to assess sensitivity of the near-surface permafrost and surface climate to soil and snow formulation. Mineral soils are generally not representative of the land coverage in the Arctic where organically rich soils are present over large areas. The soil organic carbon (SOC) has very different thermal and hydraulic properties compared to mineral soils and must be taken into account in any land surface model (LSM) to get realistic representation of the annual cycle of soil temperatures. The SOC greatly modifies the thermal and hydraulic properties of the soil column due to its high porosity, low thermal conductivity and relatively high heat content (Beringer et al. 2000; Letts et al. 2000). Recent studies (Nicolsky et al. 2007; Lawrence and Slater 2008; Rinke et

al. 2008; Dankers et al. 2011) demonstrated the need to include SOC in LSMs for improved simulations of soil thermal and moisture regimes, hence near-surface permafrost.

The presence of SOC can have significant impact on the surface energy balance by increasing the energy flux towards the atmosphere, caused by lower thermal conductivity and by impacting the partitioning of this energy into latent and sensible heat fluxes. Very few studies have addressed the impact of SOC on the coupled land-atmosphere system. Lawrence et al. (2008) and Rinke et al. (2008) obtained opposite impacts of SOC in their respective coupled land-atmosphere models. Results of Lawrence et al. (2008) show large increases in the sensible heat flux, leading to increased near-surface air temperatures, a deepening of the atmospheric boundary layer and a decrease in low-level clouds. Rinke et al. (2008) obtained increased latent heat flux, decreased air temperatures and increased low-level clouds. These contradictory results raised important questions on the sensitivity of the surface climate to the implementation of SOC.

Permafrost warming (and degradation) has been observed in multiple regions across the Arctic. The use of numerical modeling to assess the Pan-Arctic permafrost changes is important, given the limited number of observations. Although some studies are available on such scales, most of them were performed using either LSMs driven by observational datasets, reanalysis products or atmospheric fields from general circulation models (GCM), neglecting the potential feedbacks arising from the land-atmosphere interactions. The objectives of the second chapter of this thesis are twofold. The first objective is to assess the sensitivity of the simulated Pan-Arctic soil temperature and moisture regimes to the LSM column depth, to the implementation of SOC parameterization and modified snow conductivity. This first objective is performed using the Canadian Land Surface Scheme (CLASS) driven by reanalysis, therefore in stand-alone mode, neglecting the land-atmosphere interactions and feedbacks.

The second objective is to study the impact of the improvements to CLASS within the coupled framework using the fifth-generation Canadian Regional Climate Model (CRCM5) on the simulated near-surface permafrost, surface climate and land-atmosphere interactions. Analysis of the changes in the surface energy partitioning due to the implementation of the SOC parameterization contributes to reducing the uncertainties noted in previous studies by

Lawrence et al. (2008) and Rinke et al. (2008). Lastly, evaluation of the CRCM5 ability to reproduce the observed warming trend over the Arctic and its relation to the permafrost temperature and active layer thickness is a crucial step prior to considering any climate projections.

Figure I.1: Topography and bathymetry of the Arctic based on the ETOPO5 data set, NOAA 1988 (AMAP 1998).

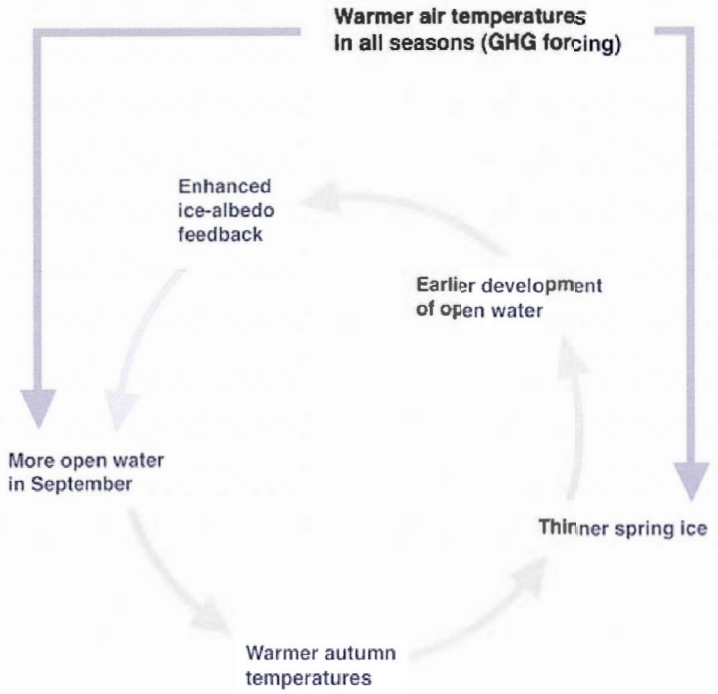

Figure I.2: Illustration of mutually supporting processes favoring acceleration of the September sea ice trend (Stroeve et al. 2012).

CHAPTER I

CAUSES AND CONSEQUENCES OF MID-21st CENTURY RAPID ICE LOSS EVENTS SIMULATED BY THE ROSSBY CENTRE REGIONAL ATMOSPHERE-OCEAN MODEL

This work is published in the peer-reviewed journal Tellus A. The detailed reference is:

Paquin, J.-P., R. Döscher, L. Sushama, T. Koenigk. 2013. "Causes and consequences of mid-21st Century Rapid Ice Loss Events simulated by the Rossby Centre Regional Atmosphere-Ocean Model". *Tellus A*, **65**, http://dx.doi.org/10.3402/tellusa.v65i0.19110

Abstract

Recent observations and modeling studies suggest that the Arctic climate is undergoing important transition. One manifestation of this change is seen in the rapid sea ice cover decrease as experienced in 2007 and 2012. Although most numerical climate models cannot adequately reproduce the recent changes, some models produce similar rapid ice loss events (RILEs) during the mid-21st Century. This study presents an analysis of four specific RILEs clustered around 2040 in three transient climate projections performed with the coupled Rossby Centre regional Atmosphere-Ocean model (RCAO). Analysis shows that long-term thinning causes increased vulnerability of the Arctic Ocean sea ice cover. In the Atlantic sector, preconditioning (thinning of sea ice) combined with anomalous atmospheric and oceanic heat transport cause large ice loss, while in the Pacific sector of the Arctic Ocean sea ice-albedo feedback appears important, particularly along the retreating sea ice margin. Although maximum sea ice loss occurs in fall, response in surface air temperature occurs in early winter, caused by strong increase in ocean-atmosphere surface energy fluxes, mainly the turbulent fluxes. Synchronicity of the events around 2040 in the projections is caused by a strong large-scale atmospheric circulation anomaly at the Atlantic lateral boundary of the regional model. The limited impact on land is caused by vertical propagation of the surface heat anomaly rather than horizontal, caused by the absence of low-level temperature inversion over the ocean.

1.1 Introduction

Climate change, induced by increased anthropogenic emissions of greenhouse gases, is one of the greatest environmental issues today. These changes are being experienced particularly intensely in the Arctic, where the temperatures have risen at almost twice the rate of the rest of the world in the past few decades (ACIA 2005). The climate change projections realized with coupled general circulation models for the 21st Century for the region suggest further warming. It should be noted though that the uncertainties in the projections for the Arctic are larger compared to those for lower latitudes, as shown by the large spread amongst models that participated in the third World Climate Research Program's (WRCP) Coupled Model Intercomparison Project (CMIP3). Understanding the changes in the Arctic climate is crucial not only for regional environmental and social issues, but also for global climate due to interconnections between the Arctic and global climates.

The Arctic sea ice cover and its thickness, due to the relation to atmospheric and oceanic temperatures, is a sensitive indicator of climate change in the region. According to Stroeve et al. (2007), the September Arctic sea ice extent has decreased during the 1979–2006 period at rates of 9.1% per decade. The recent years, however, showed accelerated summer sea ice loss with 2007, 2011 and 2012 showing historical minimum values in the satellite observation era (Comiso et al. 2008; NSIDC). Nghiem et al. (2007) using observations and a drift-age model suggested large acceleration in the rate of decrease of thick perennial (multi-year) ice reaching unprecedented values of 23% between March 2005 and March 2007. The transition from thicker perennial ice towards thinner first-year ice over the 2006–2007 period made the ice more vulnerable, leading to the summer historical minimum values of 2007 (Nghiem et al. 2007).

In addition, a number of other mechanisms also contributed to this rapid observed decrease in sea ice extent. The large-scale atmospheric circulation played an important role; for example, Deser and Teng (2008) and Wang et al. (2009) showed that trends in sea ice cover over the marginal ice zones can be linked to the Northern Annular Mode (NAM) through the surface wind anomalies. This circulation anomaly strengthened the transpolar-drift, with anomalous meridional wind blowing from the western to the eastern Arctic, thus enhancing export of sea ice through Fram Strait. Nghiem et al. (2007) also showed observational evidence of

increased inclusion of perennial (thick multi-year) ice in the transpolar drift, leading to massive ice volume exports through Fram Strait during the 2006–2007 period. However, the analysis by Deser and Teng (2008) concluded that the circulation anomalies couldn't explain the overall summer and winter trends in the sea ice cover.

Kay et al. (2008) studied cloud cover and its potential links to the rapid decrease in sea ice during the 2006–2007 period. They report a 16% decrease in summertime cloudiness over the Western Arctic from satellite and ground-based data in 2006 and 2007, which leads to an increase in downwelling shortwave radiation of $32 W/m^2$, while little changes in downwelling longwave radiation ($-4 W/m^2$) were observed. Analysis of the changes in clouds and radiation over the summer melt season showed the potential to increase surface melting by 0.3 m or a 2.4 K warming of the sea surface temperature, energy potentially used for bottom melting of the ice. Although this anomaly of reduced cloudiness is not unprecedented in records, Kay et al. (2008) suggests that the presence of thinner sea ice over the region made the system more vulnerable. This suggests that, in the future, anomalies in cloud cover and radiative fluxes might play an increasingly important role in regulating summer sea ice extent. Observations of the ice mass balance over the Beaufort Sea confirmed a large increase in the bottom melting of the ice, mainly in 2007, caused by warmer ocean temperatures due to enhanced shortwave absorption, triggering an ice-albedo feedback and accelerated the sea ice melt (Perovich et al., 2008).

Investigation of the Arctic climate using coupled general circulation models showed that none of the models contributing to CMIP3 were able to reproduce the observed acceleration of the Arctic sea ice loss. Stroeve et al. (2007) clearly showed that CMIP3 coupled general circulation models underestimate the sensitivity of the Arctic sea ice to external forcing caused by the increase in greenhouse gas concentration. Analysis performed with the Community Climate System Model version 3 (CCSM3; Collins et al., 2006) showed rapid decreasing trends, suggesting nearly ice-free conditions by approximately 2050 (Holland et al., 2006, hereafter H06), while other models in the CMIP3 ensemble do not reach such state by 2100 (Stroeve et al., 2007). These results highlight the existing uncertainties in the simulation of the Arctic climate and the need for further investigation.

The modeled transition from perennial sea ice cover to nearly ice-free summer often shows abrupt sea ice reduction periods with trends similar in magnitude to those observed during the recent 2006–2012 period. These Rapid Ice Loss Events (RILEs) are characterized by abrupt summer sea ice extent reduction over short time periods (5-10 years). Using the CCSM3, Holland et al. (2006), in an assessment of the relative roles of natural and forced changes in sea ice loss, identified multiple mechanisms responsible for such abrupt reduction in sea ice cover. The long-term thinning over multiple decades occurring before the RILEs increased the vulnerability of the sea ice cover, while 'pulse-like' ocean heat transport anomalies were found to be the triggering mechanism for rapid sea ice loss. Once the ice loss has been triggered, a positive sea ice-albedo feedback occurs in CCSM3, further accelerating the sea ice melt leading to extensive Arctic sea ice loss. Holland et al. (2008, hereafter H08) suggested that the increased vulnerability of the sea ice caused by anthropogenic forcing results in an increase in the intrinsic variability of the sea ice cover.

One of the important concerns related to the RILEs is the consequences on the Arctic climate system. Under conditions of reduced sea ice cover, the atmosphere comes in contact with the warm ocean waters leading to low-level atmospheric warming through increased turbulent fluxes at the surface. Surface winds can later advect this warm air towards surrounding land masses, further accelerating the general warming due to climate change over the adjacent permafrost underlain regions. This accelerated warming during RILEs can accelerate permafrost degradation (Lawrence et al., 2008) already observed in some parts of the Arctic, thus impacting soil thermal and moisture regimes, which can have an influence the pan-Arctic biome. Another potential hazard is the release of soil carbon sequestered in the frozen ground, likely in methane form, to the atmosphere causing a positive feedback leading to further increase in temperature in future climate.

In a previous study, Döscher and Koenigk (2013), hereafter DK, studied 30 sea ice reduction events in an ensemble of 6 regional Arctic climate scenarios from the Rossby Centre Atmosphere-Ocean model (RCAO, Döscher et al. 2002 and 2009). DK studied sea ice reduction events throughout the 1980–2080 period in order to identify physical processes leading to these reductions. In DK, sea ice reduction events are defined as summer sea ice cover reduction of 1,200,000 km^2 over a single or multiple successive years. This criterion is

less constraining compared to that of H08 and the present study, and allowed them to perform statistical analysis over 30 less extreme sea ice reduction events. DK suggested that sudden ice loss mechanisms were strongly related to changes in the large-scale atmospheric circulation and also influenced by sea ice thinning as a preconditioning. Clustering of RILEs during the 2030–2035 period amongst the regional scenarios was indicative of a strong control of large-scale atmospheric forcing from the lateral boundary condition from ECHAM5/MPI-OM common scenario (hereafter ECHAM). Relating RILEs to atmospheric circulation anomalies, DK generally concluded that RILEs in RCAO could result from changes to the large-scale atmospheric circulation with very limited impact of seasonal radiative forcing on average.

The present study aims to provide a more comprehensive understanding of the physical mechanisms responsible for 4 specific extreme RILEs simulated by RCAO clustered around 2040 with additional analysis of aspects not addressed in the previous study by DK. These analysis include: detailed analysis of the surface energy fluxes and surface temperature are presented for the pre-RILE period, during the RILE and post-RILE period. Strong relations between RILEs and the changes in the atmospheric and oceanic circulation are established to demonstrate the important role played by the large-scale flows in the synchronicity of the extreme RILEs. In addition, we investigate the impacts of RILEs on the sea ice variability and the atmospheric structure along with the regional response of temperature over the nearby coastal areas.

The outline of this paper is as follows. Section 1.2 provides a brief description of the RCAO formulation and the model integrations. RCAO present-day climatology for the climate projections and comparison with the driving model ECHAM is presented in Section 1.3 while Rapid Ice Loss Event analysis is presented in Section 1.4, followed by discussion and conclusions in Section 1.5.

1.2. Model description and experimental design

1.2.1 Model description

The Arctic regional climate projections considered in this study are performed by the Rossby Center coupled Atmosphere Ocean model (RCAO, Döscher et al. 2002 and 2009) which consists of RCA for the atmosphere (Jones et al. 2004a; Jones et al. 2004b; Kjellström et al. 2005) and RCO for the ocean (Meier et al. 2003). The model domain is centered over the Arctic and extends from approximately 50°N in the North Atlantic to the Aleutian Islands in the North Pacific (Fig. 1.1). The RCA domain was chosen in a way to avoid large orographic features near the lateral boundaries while covering large enough areas to get realistic wind forcing over the Bering Sea. Both RCA and RCO are integrated at 0.5-degree horizontal resolution, on a rotated latitude-longitude grid for RCA and a spherical grid for RCO.

The RCO ocean model is based on the parallelized 3D primitive equation model in geopotential coordinates with a free surface (Webb et al. 1997). Detailed description of the model formulation and evaluation can be found in Meier et al. (2003) and Döscher et al. (2009). RCO has 59 unevenly distributed vertical levels with the bottom topography interpolated from ETOPO5 dataset (1988). Vertical resolution is 3m at the surface gradually decreasing to 200m at 5000m. The Aleutian Islands form a closed ocean boundary while an open boundary, following formulation by Stevens (1991), is located in the North Atlantic. RCO includes a 2-category dynamic-thermodynamic sea ice model based on elastic-viscous-plastic (EVP) rheology (Hunke and Dukovicz 1997) and Semtner-type thermodynamic formulation (Semtner 1976). Snow and sea ice albedo formulation is dependent on the ice temperature following a modified version of Køltzow (2007). A melt pond parameterization based on SHEBA ice drift station data is included in the model (Döscher et al. 2009).

The atmospheric component RCA, based on the limited-area weather prediction model HIRLAM (Undén et al. 2002), is a semi-implicit, semi-Lagrangian, hydrostatic grid-point model using terrain-following hybrid vertical levels. The present version uses 24 vertical levels with the model top at 15hPa. Adaptation of the physical parameterization to run in climate mode was performed in the early stage of RCA development, especially the radiation

and turbulence schemes (Jones et al. 2004a,b). Recent improvements to the radiation, turbulence and cloud schemes are described in Kjellström et al. (2005). The land surface scheme follows the formulation discussed in Samuelsson et al. (2006) with 5 thermodynamic and 3 moisture levels both reaching a depth of 1.89m.

RCA and RCO are run in parallel and use the coupler OASIS4 (Valcke and Redler 2006) to exchange information every 3 hours. RCA provides heat, radiation, freshwater and momentum fluxes to RCO, while the ocean provides sea surface temperature (SST), sea ice concentration and temperature, snow and ice albedo.

1.2.2 Experiments

Three RCAO Arctic regional projections covering the 1960–2080 period are used; the projections follow SRES-A1B greenhouse emissions scenario. Ocean initial conditions for RCAO are obtained from the Polar Science Center Hydrographic Climatology data (PHC, Steele et al. 2001) which is available at 1° resolution. Sea ice is initialized with a thickness of 2.3m and 95% sea ice concentration for all grid points where the sea surface temperature is equal to or below freezing point. Previous study by Döscher et al. (2009) showed that the RCAO ocean near-surface layers reach advective balance after 20 years of simulation (1960–1979).

Atmospheric initial and lateral boundary conditions for all RCAO runs are taken from a single realization of the General Circulation Model ECHAM5/MPI-OM. Land surface is also initialized from ECHAM5 fields. Differences between the RCAO projections reside in the North Atlantic Ocean boundary conditions and the sea surface salinity correction method, as presented in Table 1.1. The first regional projection is performed using monthly climatological values from PHC at the North Atlantic Ocean boundary (ECHstand2) repeated throughout the projection, while the other two projections (ECHMPIstand and ECHMPIflux) use evolving monthly ocean fields from the driving ECHAM transient experiment.

Two methods are commonly used to apply corrections to RCAO sea surface salinity due to the misrepresentation of freshwater fluxes into the ocean. The first method, used for ECHMPIstand, is a relaxation method using a timescale of 240 days to correct the surface

salinity towards the PHC values. This relaxation is active during the entire climate projection. The second method, used for ECHMPIflux, is a mean monthly flux correction method. The annual cycle of monthly averaged surface salt flux correction was computed from the salt deviation between PHC and an RCAO experiment driven by ECHAM over a 20-year period at the end of the 20th Century. Monthly salt-flux corrections are used without modification throughout the 120-year RCAO climate projection ECHMPIflux. Detailed description of the salinity correction methods can be found in Koenigk et al. (2011).

1.3 RCAO climatology

The coupled model performance has been described in two previous papers (Döscher et al. 2009; Koenigk et al. 2011), including transient evolution of the 2 m-air temperature, sea ice extent and volume. Nevertheless, the understanding of the mechanisms and causes of the Rapid Ice Loss Events requires description of RCAO's climatology to provide context in which the events are occurring and build a basis for comparison with the recent observed 2007 and 2012 events and to other modeling studies.

Figure 1.2 shows the 1980–1999 sea ice thickness fields and the sea ice margin location (SIC>15%) for the ensemble mean of the three RCAO projections and for the driving ECHAM realization. In March, RCAO simulated sea ice margin is in good agreement with sea ice data from ERA-Interim (Dee et al. 2011) except for some underestimation in Barents and Labrador Seas. ECHAM shows better agreement over these two regions but overestimates the sea ice cover in Bering Sea. September sea ice extent is underestimated in RCAO especially in Kara Sea and along Greenland while ECHAM tends to overestimate the sea ice extent over those regions. For sea ice thickness, RCAO produces much thinner ice compared to ECHAM, with maximum sea ice thickness in March located along the Siberian coast (3–3.5 m) and a secondary maximum along the Canadian Arctic Archipelago (2–2.5 m). ECHAM sea ice is thicker than 4m over most of the Central Arctic basin. In September, sea ice thins below 2 m in RCAO except along the Siberian coast while ECHAM retains thick ice over most of the Arctic basin.

Based on numerous studies showing similar biases in the sea ice cover and thickness distribution in coupled models (Chapman and Walsh 2007; Bitz et al. 2002; deWeaver and Bitz 2006; Koldunov et al. 2010), we hypothesize that these differences mainly arise from the simulated atmosphere and associated surface forcings. This hypothesis is supported by results from Mårtensson et al. (2012) who performed RCO standalone simulations driven by ERA-40 reanalysis (Uppala et al. 2005) where the maximal sea ice thickness is located along the Canadian Arctic Archipelago where present-day thickest ice is found (Bourke and Garret 1987; Koldunov et al. 2010). Further improvements of the sea ice thickness distribution in Mårtensson et al. (2012) was achieved by including a multi-category sea ice scheme which was not included in the present RCAO experiments. Moreover, Fig. 1.3 presents the 1980–1999 average sea level pressure (SLP) and 2 m-air temperature (T2M) for ERA-Interim, the RCAO ensemble average and ECHAM. In March, both models overestimate SLP over Iceland, the Nordic Seas and parts of the Atlantic sector. In September, a positive bias is centered over the Central Arctic. This bias is slightly more pronounced in RCAO than in ECHAM. The temperature difference between RCAO and ERA-Interim (Fig. 1.4) shows large warm bias in March over the region of underestimated sea ice extent over Barents and Labrador Seas while a cold bias is present over the Central Arctic, also found in ECHAM. The bias in SLP indicates anomalous surface circulation from the CAA towards the Siberian coast in winter (not shown), which is responsible for the maximal sea ice thickness along the Siberian coast in RCAO. This bias in ice thickness distribution associated with biases in wind forcing is a common problem in many coupled models (Bitz et al. 2002; deWeaver and Bitz 2006; Holland et al. 2006), and the reason for this is still poorly understood (Koldunov et al. 2010). In September, RCAO shows positive biases in SLP indicating the presence of a quasi-permanent high-pressure anomaly over Central Arctic basin with weak interannual variability within RCAO's individual projections (not shown). The biases in the SLP fields directly affect the surface winds, which in turn modify the ice dynamics. Since sea ice drift is nearly parallel to the isobars (Kwok 2008), the systematic high-pressure bias in RCAO compared to ERA-Interim is very likely responsible for an erroneous sea ice motion leading to thicker sea ice along the Siberian coast. The positive 2 m-air temperature present in September is also likely to increase top ice melting, therefore reducing the sea ice thickness compared to observations.

Although ECHAM shows a similar SLP difference pattern, the maximum sea ice is located between the coast of Greenland and Ellesmere Island and the North Pole (Koldunov et al. 2010), while the overestimated thickness is most likely caused by the cold bias over the Arctic basin (Koenigk et al. 2011). Interestingly, when computed over 2025–2044 period, sea ice thickness distribution in ECHAM shows similar patterns to RCAO for the 1980–1999 period (not shown). Differences in sea ice thickness and the resulting sea ice volume between RCAO and ECHAM persists throughout the simulation, with ECHAM showing acceleration in sea ice loss from 2020 onward (Koenigk et al. 2011).

The focus of this paper is to understand the mechanisms responsible for triggering the Rapid Ice Loss events and their effects on surface fields as simulated by RCAO, despite the model limitations. Albeit the impact of the model biases on the simulation of recent past sea ice conditions, this study contributes to improved understanding of not only RCAO behavior, but also of those numerous models sharing similarity in their atmospheric circulation.

1.4 Rapid Ice Loss Events

1.4.1 Rapid Ice Loss Events

In order to focus on extreme events, the RILE criteria used in this study are more conservative compared to the one used in the previous study of DK. The central year of a RILE is defined when the derivative of the five-year running mean of the minimum September sea ice extent exceeds a value of -0.5 million km^2yr^{-1}. In the case that two successive years are below this threshold, the first year is defined as the central date. The duration of each event is defined as the period around the central year showing a loss of 0.15 million km^2yr^{-1} or more included in a ±5 year radius. These criteria are adapted from a sea ice loss study by H06.

Figure 1.5 presents the time series of the September sea ice extent from satellite observations (Fetterer et al. 2002, *updated 2011*), simulated by ECHAM and RCAO with identification of the RILEs detected using the aforementioned criteria. Firstly, RCAO produces realistic September sea ice cover compared to satellite observations, although

underestimated (see also Fig. 1.2), and the recent past decreasing trend is well captured. The driving model, ECHAM, overestimates the sea ice cover, while it underestimate the observed decreasing trend, most likely related to the cold bias presented in section 1.3.

All RCAO integrations show very similar behavior, with a decrease in the September sea ice extent during the 90's, recuperation in the 2000–2010 period, followed by a period of general decrease from 2010 to 2030. Between 2030 and 2040, accelerated September sea ice loss, satisfying RILE criteria is noted. An interesting aspect is the synchronicity of the RILEs for all RCAO projections around 2040, suggesting strong control of the large-scale atmospheric boundary conditions from ECHAM (see section 1.4.2.5). All projections show a partial recovery period of September sea ice extent between 2040 and 2055, some years reaching values comparable to the sea ice extent prior to the 2040 drastic events, followed by a third sea ice loss period extending from 2055 to the end of the projection. The recovery is a dominant factor in the study of the impacts of RILEs by limiting the period over which the atmosphere can react to reduced ice coverage. Although ECHAM shows large negative trends in sea ice extent from 2030 to 2080, no RILEs are detected using the aforementioned criteria in the global projection used to drive RCAO at its lateral boundaries. It should also be noted that in the study by H06 using CCSM3, sea ice recovery was absent. A total of 4 rapid ice loss events in the 3 RCAO regional projections are considered in this study, with average duration of 5.5 years, as summarized in Table 1.2.

1.4.2 Causes and effects of RILEs

This section investigates the characteristics of selected near-surface variables and key physical processes in action during the RILEs. Comparisons are performed between three different periods: RILE period where averages are computed over the duration of the event (consult Table 1.2 for event duration) and pre-RILE period (post-RILE) where averages are computed over the 10 years before (after) the RILE period itself. Due to the similarity of the pre-RILE and RILE periods for all the events occurring around 2040, the R2 event is presented in details; similarities and differences with other events are discussed where appropriate.

1.4.2.1 Sea ice field morphology

Figure 1.6 presents bimonthly averages of sea ice cover and thickness for the R2 event for the pre-RILE and RILE periods. For both pre-RILE and RILE periods, the Arctic ice pack in summer (July-August) and autumn (September-October) is characterized by high fractional cover extending from the East Siberian Sea shores to the Canadian Arctic Archipelago (CAA). In autumn, marginal seas are almost completely ice-free except the East Siberian Sea and the eastern parts of the Chukchi Sea. The thickest ice is located in the East Siberian Sea, as a result of a westward displacement of the winter high-pressure ridge over the Central Arctic Ocean, causing anomalous winds pushing the ice towards the East Siberian Sea coastal regions as presented in section 1.3. This displacement is stronger during pre-RILE periods with winds parallel to the coast from the East Siberian Sea towards the New Siberian Island where ice is the thickest (not shown). This displacement is a well-known large-scale near-surface circulation bias in atmosphere-ocean coupled models (Bitz et al. 2002) accentuated by lack of sufficient number of sea ice classes in RCAO sea ice scheme (Mårtensson et al. 2012). A secondary maximum is located along the CAA shore at the location of present-day thickest ice (Bourke and Garret 1987).

The largest differences in the sea ice cover between pre-RILE and RILE periods is noted for the September-October period. Sea ice cover fraction decreases over the whole Arctic ice pack and open water is formed principally in two distinct regions, over the Canada basin and in the vicinity of the North Pole.

Although the maximal sea ice loss occurs in late autumn, changes can be noted in the sea ice cover in early winter (i.e. November-December) suggesting a delay in the formation of new ice due to accumulation of heat in the ocean. The regions that show decreasing sea ice fraction are along the marginal ice zone in the Atlantic sector (in the vicinity of Franz Joseph Land) and offshore of East Siberian Sea towards Chukchi Sea and extending weakly to Beaufort Sea. During RILE period, signs of early melt in summer (July-August) are visible along the coast of Alaska and in the Atlantic sector along the ice marginal zones, potentially contributing to accelerated ice melt during late summer, as suggested in Steele et al. (2010). The Arctic ice pack is characterized by thin ice (<1 m) over Central Arctic in the pre-RILE and RILE periods, suggesting high potential sensitivity of the sea ice cover to external factors

such as modification in the large-scale atmospheric and oceanic circulations or changes in surface energy budget, presented in details later in this study.

1.4.2.2 Sea Ice vulnerability and long-term pre-conditioning by thinning

Observations and numerical experiments suggest that long-term thinning of the Arctic ice plays a major role in increasing the ice vulnerability to external forcing such as changes in large-scale atmospheric and oceanic circulations, changes in radiative fluxes, or surface temperatures (Holland et al. 2008; Kay et al. 2008; Perovich et al. 2008). This increased vulnerability is believed to have led to the 2007 minimum in sea ice cover. Figure 1.7 presents the evolution of average September sea ice thickness for the Arctic for the 1980–2070 period calculated over each grid point where sea ice cover is larger than 15%. Decreasing trend is clearly visible over 1980–2040 period, in good correlation with the September sea ice extent (Fig. 1.5).

To evaluate the vulnerability of the sea ice extent to the thinning of the ice, Fig. 1.7 presents the relationship between the standard deviation of September sea ice extent and the average sea ice thickness for 20-year sliding windows over the 1980–2070 period. The standard deviation of September sea ice extent is computed using each regional projection after subtracting the ensemble average. This way, we measure the natural variability in September sea ice extent of each simulation excluding the large-scale signal, filtered in the ensemble average. The small number of projections is compensated by the synchronicity of the events allowing reasonable removal of the large-scale signal. As shown in Figs. 1.2 and 1.7, RCAO generally produces thinner ice compared to other climate models (Holland et al. 2006, 2008, 2010; Koenigk et al. 2011), with Arctic Basin maximum average September thickness reaching at most 120cm in the 80's (Fig. 1.7). Nevertheless, Fig. 1.7 confirms increased variability of September sea ice extent for thinner ice for all projections and for the ensemble mean. Compared to a similar plot in the study of Holland et al. (2008) where asymptotic behavior was clearly visible with decreasing variability at thickness below 1m, RCAO shows very large variability even in very thin ice conditions (<50 cm), suggesting that ice formation is highly sensitive to interannual changes of the exterior factors such as large-

scale atmospheric and oceanic flows or changes in radiative fluxes, explored later in this study.

1.4.2.3 Changes to selected near-surface fields during RILEs

Changes in sea ice cover and thickness modify the surface conditions seen by the atmosphere. Figure 1.8a shows bi-monthly differences between the RILE and the pre-RILE periods for sea ice cover and thickness. Maximal ice thickness reduction during the RILE occurs in September-October over the East Siberian Sea causing a sea ice cover reduction from 90–95% to 75%. The Central Arctic also thins from 50cm down to 15cm around 150°E, leading to a sea ice cover decrease from 80% to 50%. November-December shows similar thinning pattern and magnitude as September-October (Fig. 1.8a) but the ice is thick enough to effectively cover most of the Arctic Basin, causing small changes in the sea ice cover. The 2 m-air temperature increases during late autumn (September-October) but the maximal warming, up to 10°C, occurs over the ocean during early winter (November-December). Statistical analysis of the 2 m-air temperature differences between the Pre-RILE and the RILE periods was performed using a t-test at 80%, 90%, 95% and 99% confidence levels (Fig. 1.8a). The 100-year trend in 2 m-air temperature was removed prior to the testing to isolate the effect of the event from the background warming. Despite the limited length of 10 years for the Pre-RILE period and 8 years for the RILE period, Fig. 1.8a show that the warming is mostly significant over the 95% confidence level for the Central Arctic Ocean during late autumn and winter. The warming patterns over the Nordic Seas in September-October is also significant above 90% which will be shown later in the study to be crucial in the understanding of the RILE mechanism for the Atlantic Sector of the domain. In MJ and JA, the large area of statistical significance over the Arctic Ocean and the weak signal in the trended differences is simply caused by a compensation between the long-term warming trends and a short term decrease in temperatures between the two period over these months in the detrended fields. While the detrended differences are small, between -2 and 0 °C, the very small interannual variability of the temperature reaches statistical significance. In the non-detrended differences, there is a net compensation between the long-term warming trends and the short-term cooling leaving an almost zero signal in the differences.

It is found that the 2 m-air temperature response follows the changes in the net surface energy budget, and not the maximal changes in sea ice cover (Fig. 1.8b). The delay between the maximal increase in air temperature relative to the sea ice cover during the RILE period can be explained by increases in the turbulent heat fluxes, both sensible and latent, during the November-December period. Differences are due to the greater exposure of ice-free ocean to colder surface air temperature in early winter compared to milder fall air temperatures. The radiative contribution to the changes in net surface energy budget is limited to -5 Wm^{-2} for terrestrial radiation while solar contribution is zero during the polar night (Fig. 1.8b).

The January-February maximal warming is located at the sea ice margin of the Atlantic sector and over Kara Sea. Both regions show statistically significant warming caused by the increase in the surface turbulent fluxes due to sea ice retreat. Increased anomalies in turbulent fluxes towards the atmosphere are located over retreating sea ice margin, caused by increased exposure of the atmosphere to the relatively warm ocean causing a northward shift in the location of the maximum ocean-atmosphere heat transfer. The region of decreased ocean heat loss over the Barents Sea (Fig. 1.8b) is partly caused by the anomalous southerly circulation over the area, discussed in detail in the next section, decreasing the ocean-atmosphere vertical temperature gradient, thus reducing heat transfer. This dipole structure, consisting of decreased-increased ocean-atmosphere heat fluxes along the retreating sea-ice margin, is coherent with results from CAM3 simulations analyzing the effect of imposed reduction of sea ice cover during a hindcast experiment (Deser et al. 2010).

The net surface solar radiation (Fig. 1.8b) increases due to the retreat of sea ice in May-June over Kara Sea (30-35 W/m^2) and Northern Baffin Bay. This increased absorption of solar radiation, mostly by open water, warms the ocean surface layer and increases the heat content of the ocean, potentially used for bottom ice melt, as suggested by many observations and modeling studies (Perovich et al. 2008; Kay et al. 2008; Steele et al. 2010). The role of increased absorbed solar radiation by the ocean before and during the RILE is found to be a dominant factor over the Pacific sector of the Arctic Ocean in RCAO and will be presented in the next section.

The R1 and R3 events resemble the R2 event in multiple aspects. The R3 event (ECHMPIflux) shows stronger sea ice loss for all seasons, with a broader zone of thinning

covering the entire Arctic ice pack in September-October and also larger loss in the marginal ice zones of the North Atlantic sector for all other seasons. The spatial patterns of increase/decrease of the 2 m-air temperature for R3 are slightly different when compared to the R2 event. Nevertheless, they are caused by the same mechanisms, i.e. changes in the net surface energy flux with the turbulent fluxes playing a dominant role in autumn and winter, while increase in net shortwave is important in spring.

The sea ice cover differences are smaller for R1, especially in the marginal ice zones of the North Atlantic sector, leading to milder changes in 2 m-air temperatures and energy fluxes. This is linked to the oceanic heat transport and is explained in detail in section 1.4.2.5. The R4 event occurs in 2063, nearly 20 years after the first period where the R1, R2 and R3 event occurs (~2040) and after the sea ice "recovery" of the 2050's. Therefore, sea ice is thinner and likely increases the sensitivity of the ice to changes in atmospheric fluxes or changes in circulation. Nevertheless, patterns for both sea ice cover and thickness and their changes during the RILE are similar to the 2040 events and shows similar changes to the surface energy fluxes.

1.4.2.4 Large-scale atmospheric circulation and sea surface temperature anomalies

The general circulation patterns present in the decades preceding the RILEs (2020-2040) are very similar to those of the 1980–1999 climatological period presented in section 1.3. Both RCAO and ECHAM show continuity in the large-scale atmospheric patterns, suggesting a small sensitivity of the atmospheric large-scale circulation to the increased GHG concentrations. Therefore, the analysis of the anomalies in the large-scale circulation causing the RILEs is performed in the context of quasi-permanent anticyclonic circulation over the Arctic basin with relatively weak interannual variability.

In this section, the impact of the short-term modifications of the large-scale atmospheric circulation and SSTs are analyzed. Figure 1.9 presents bi-monthly anomalies of sea-level pressure (SLP) and sea surface temperature (SST) between the RILE and the Pre-RILE periods for the R2 event along with an analysis of the statistical significance of the differences using a t-test.

In July and August (JA), the SST increase over the entire Atlantic sector of the domain, defined as the region between the Nordic Seas extending to the Lomonossov ridge. While the warming is moderate over the Nordic Seas (0.3-0.6 °C) the northernmost the region shows statistical significant the warming to be significant. Larger warming up to 3 °C can be observed over Kara Sea and along the retreating sea ice margin near the North Pole with statistical significance over 90% confidence level. Maximal SST warming for JA is collocated with maximum increases in 2 m-air temperature and sea ice loss (Fig. 1.8a) near the North Pole, the southern regions being already ice-free in the Pre-RILE period.

In September-October, positive SST anomalies, though reduced in magnitude, are still present and statistically significant at 95% over regions where sea ice cover decrease has been noted, namely near the North Pole and offshore of the East Siberian Sea (Fig. 1.8a). The SST over those regions remains above freezing point (not shown) thus delaying sea ice formation. The statistically significant SLP anomalies in autumn (Fig. 9) lead to anomalous southerly winds, advecting warmer air from the Nordic Seas towards the Arctic. Conjointly, changes in 2 m-air temperature over the same region are also significant. One can clearly see a downward net surface energy flux anomaly (Fig. 1.8b) over broad region of the Barents Sea, resulting from a decreased air-ocean temperature contrast caused by the advection of warmer air from the south. This decrease in the energy flux from the ocean to the atmosphere slows the cooling of the near-surface ocean layers, allowing for the warm anomaly to persist, penetrate deeper in the Arctic region and further delay the ice formation. Warm atmospheric inflow in that region during RILEs is coherent with similar finding for summer (JAS) in DK.

During early winter, i.e. November-December, positive SST anomaly is still present and significant in the North Atlantic sector but in a reduced amplitude due to the change in the anomalous large-scale atmospheric circulation. Indeed, the positive SLP anomaly south of Iceland in November-December signals a weaker Icelandic low-pressure system, thus reducing heat transport from the North Atlantic towards the Arctic. Deprived of heat advection from the southern flow, the atmosphere cools rapidly increasing ocean-air temperature gradient at the surface. This leads to increased turbulent surface fluxes in the North Pole region (Fig. 1.8b) and thereby increasing the surface cooling in the ocean producing favorable conditions for the onset of ice formation.

In January-February, changes in the SLP anomaly show a regain of wind blowing from lower latitudes, directed towards the Barents Sea. The advection of warmer air over Barents Sea decreases the air-ocean temperature gradient, causing downward net energy flux over most of the region, except the location of sea ice loss, where strong upward fluxes are observed (Fig. 1.8b). Again, net downward fluxes cause the positive SST anomaly to persist and to remain statistically significant.

While March-April SLP shows a deeper cyclonic Icelandic system during the RILE period, the circulation anomaly is mainly located over the Nordic Seas and does not propagate as far north as it did for January-February and September-October. This results in decreased amplitude of 2 m-air temperature and net radiative balance anomalies over Barents Sea (Fig. 1.8b). In May-June, significant positive SST anomalies develop over the regions of decreased sea ice cover although the SLP anomalies do not suggest southerly inflows. The positive SST anomaly is shown to be caused by the increased net shortwave absorption of 30 Wm^{-2} along the sea ice margin, reaching values of 40 Wm^{-2} over the Kara Sea, which increases the ocean heat content near the surface, explaining large positive SST anomalies in the following months.

For the Pacific sector, Woodgate et al. (2010) showed an increase in the observed oceanic heat transport from the Northern Pacific to the Arctic through Bering Strait. They suggest that this increased heat acts as a trigger for the early onset of sea ice melt. These results are supported by the modeling experiment of Steele et al. (2010), where early melt along the Alaska coast is reported to be caused by the increased Bering Strait inflow, leading to the 2007 minimum. In RCAO, Ekman convergence in the ocean, resulting from the quasi-permanent anticyclonic circulation presented in section 1.3, greatly reduces the Bering Strait inflow by creating a broad region of increased sea surface height covering most of the Arctic basin (not shown). The above, along with the presence of a closed ocean lateral boundary located along the Aleutian Islands, precluding exchange with the North Pacific, leads to underestimation of the Bering Strait inflow in RCAO. In the absence of significant changes to the Bering Strait inflow during RILEs (not shown) and limited vertical heat transport from deeper ocean towards the surface (DK), other mechanisms causing the large sea ice melt over the Pacific sector were investigated. Perovich et al. (2008) showed that the increase of

absorbed solar radiation by the ocean played a major role in the negative sea ice mass balance observed for the 2007 minimum, by triggering a sea-ice albedo feedback that contributed to the accelerated the sea ice retreat.

Figure 1.10 shows the averaged anomalies of surface sea ice conditions, radiative fluxes, SST and 2 m-air temperature computed over the period from May to October (MJJASO) between the year of minimum sea ice cover for event R2 (2041) and the 2010−2030 average. Sea ice cover shows strong decrease over the Beaufort Sea with signs of retreating sea ice margin (SIC > 15%) initialized from the Amundsen Gulf in May (contours in Fig. 1.10), evolving towards an ice-free region along the Alaska coast in August (green curve). The early sea ice retreat is triggered by anomalous sea ice velocity from the coast towards central Beaufort Sea (not shown). This retreat reaches a maximum in September (grey curve), where open water is present over most of the Beaufort Sea, leading to large negative SIC anomaly. Downwelling shortwave radiation at the surface shows average negative anomalies over the retreating sea ice margin in southwestern Beaufort Sea, caused by the increase in the low cloud cover (not shown) resulting from the presence of more open water associated with release of moisture from the ocean to the atmosphere. Nevertheless, the absorbed shortwave radiation by the open water shows strong increase over the same region reaching averaged monthly values of 30 Wm^{-2} (45 Wm^{-2} in May-June). This increased energy absorbed by the ocean leads to a warming of SSTs by up to 3 °C. The combination of early sea ice retreat, increased solar energy absorbed by the ocean and an ocean circulation directed from the coastal region towards the retreating ice edge strengthens the sea ice-albedo feedback and accelerates the bottom melt of the remaining thin ice present over the region. The contribution from downwelling longwave radiation (Fig. 1.10) is smaller over the entire Beaufort Sea with maximum values smaller than 5 Wm^{-2} over the southwestern Beaufort Sea. The increased in downwelling longwave radiation corresponds to the near-surface temperature, resulting from the presence of open water and increased heat transfer from the ocean to the atmosphere. The increased 2 m-air temperature over the Northern Beaufort Sea is the result of summertime advection from the Atlantic sector, enhancing top melting of the sea ice over the area, where little changes are observed in both downwelling shortwave and longwave radiation at the surface. Compared to observations of the 2007 event (Kay et al.

2008; Perovich et al. 2008), the simulated sea ice present over the Pacific sector in RCAO is much thinner increasing its sensitivity to smaller perturbations in the radiation and clouds.

1.4.2.5 Synchronicity of RILE events and Ocean heat transport contribution

The synchronicity of the RILEs during the regional climate projections, with three of the four events occurring around 2040 (Fig. 1.5), suggests a strong control of the large-scale atmospheric and oceanic circulation on the timing of the events. Figure 1.11 presents a comparison of the 850 hPa geopotential heights anomaly between 2036–2042 encompassing the first three RILEs and the 10-year period prior (2026–2035). Figure 1.11 shows the differences between those time periods for the ECHAM climate projection used to provide the atmospheric lateral boundary conditions to all three RCAO projections along with an estimation of the statistical significance using a t-test. The 850 hPa geopotential height field allows evaluation of lower tropospheric circulation while limiting the effect of surface processes.

The comparison of the anomaly for ECHAM and the three RCAO regional projections shows large consistency between the four patterns for both the March-April and September-October periods, especially along RCAO lateral boundaries. As expected, differences between ECHAM and the regional projections and amongst individual regional projections grow towards the central part of the domain showing the decreased influence of the lateral boundary conditions towards the central part of the domain. Nevertheless, all regional projections show statistically significant geopotential anomalies leading to increased advection from the Nordic Seas towards the Central Arctic Ocean in September-October and a deepening and northward extension of the Icelandic low in March-April. These results supports the hypothesis of increased heat transport from the Nordic Seas towards the Arctic during the RILE periods. Over the North Atlantic sector, one can notice that the amplitude of the geopotential height is, over most of the region, one order of magnitude larger compared to the standard deviation of the difference amongst the regional projections. The large values of the geopotential height anomalies compared to the variability amongst individual projections, their similarity compared to ECHAM and the high level of statistical significance of the signal rules out the possibility that these anomalies occurs randomly within RCAO

projections. Moreover, the results presented in Fig. 1.11 can be generalized over the annual cycle and for multiple vertical levels in the atmosphere (not shown), again reinforcing the conclusion that the anomaly propagates from the common lateral boundary conditions provided by ECHAM.

Patterns of large-scale atmospheric circulation in events R1 and R3 show anomalous winds from Nordic Seas towards the polar region. These winds generate positive anomalies in the annual oceanic heat transport (OHT) reaching the Barents Sea shelf (Fig. 1.12). Barents Sea OHT is computed over the first 290 m of the ocean (top 25 vertical levels) along a transect from Svalbard to the Kola Peninsula using a reference temperature of -0.1°C. OHT in Barents Sea shows an increase for all RCAO projections from 2010 reaching maximum values around 2040, the central dates of R1, R2 and R3 events. The large increase from 2030 to 2040 is caused by a combination of warmer water and increased volume transport through the section, contributing to the SST warming observed over Barents Sea during the RILE events (Fig. 1.9). The differences in OHT between ECHstand2 (R1) and the other two projections increase after the 2040 maximum. The OHT simulated by the ECHStand2, which uses repeated climatological ocean lateral boundary conditions, decreases abruptly after 2040 reaching a minimum in 2045, followed by moderate increase until the end of the projection. However, the other two projections using ocean lateral boundary conditions from the global model scenario, responsible for the R2 and R3 events, show smaller decrease in OHT after 2040. It suggests that the OHT decrease in ECHMPIstand2 is responsible for a milder R1 event with reduced magnitude and duration compared to R2 and R3 events. The differences in the ocean lateral boundary condition causes the ECHstand2 to generate a more diffuse and warmer North Atlantic sub-polar gyre while the ECHMPIstand and ECHMPIflux favor warmer and stronger inflow along Ireland causing a warmer and more intense Norwegian Current which penetrates further North (not shown) causing increased temperatures in the Nordic Seas and in the Barents Sea for those two runs.

Results presented in this section leads the authors to comfortably conclude that the synchronicity of the RILE events are caused by anomalous large-scale atmospheric circulation propagating from the driving model ECHAM, efficiently propagating from the lateral boundary conditions in the North Atlantic into the regional projections. This anomaly

causes increased atmospheric and oceanic heat transport towards the Arctic Ocean, contributing to important sea ice reduction.

1.4.3 Impacts of RILEs

This section investigates the effects of the RILEs on the post-RILE period from different aspects: variability, changes over coastal regions around the Arctic Ocean and the atmospheric vertical structure.

1.4.3.1 Post-RILE variability

Following the events R2 and R3, a partial recovery period is seen in September sea ice extent (Fig. 1.5), also characterized by increased interrannual variability. The high variability at low sea ice thickness (Fig. 1.7) suggests the ability of the model to easily form thin ice, sufficient to cover relatively large areas of the Arctic Ocean. To illustrate the changes in the spatial distribution of ice and its variability, seasonal standard deviation is computed over the pre-RILE and post-RILE periods for all events. The respective linear trends for each period were subtracted prior to calculating the standard deviation. Figure 1.13 presents results for the R2 event; similar conclusions are valid for R3 and R4 events, while R1 shows weaker changes due to the smaller amplitude of the event. In summer and autumn, a transition towards more variable ice pack is observed from pre-RILE to post-RILE period. While a stable Arctic ice pack was present in summer during the pre-RILE period, represented by the area of low interrannual variability extending from the East Siberian Sea coast towards Central Arctic, very little of it remains after the RILE except over narrow regions of the East Siberian Sea and the CAA. In autumn, the annually present ice pack completely disappears. This is caused by a transition in the sea ice extent towards a more chaotic behavior with high sensitivity to anomalies in surface forcings and atmospheric circulation. Increased variability in the sea ice extent is not present in CCSM3 where September sea ice standard deviation is shown to peak during the RILE to rapidly decrease in the years following the event (see Fig. 3c and Plate 5 in H08).

1.4.3.2 Atmospheric and Land Response

To determine the longer-term changes caused by the rapid decrease of sea ice cover, Fig. 1.14 shows the average temperature anomaly for the R2 event, relative to the pre-RILE conditions, for both the RILE and the post-RILE periods over the Arctic Ocean and the surrounding continental areas. Coherently with the bi-monthly temperature changes (Fig. 1.8), the warming is maximal over the ocean in December (5.2 °C), mainly caused by the increased turbulent fluxes over remaining open water, and minimum (0.4 °C) in May. Important consistency is found between the annual cycle of the temperature anomalies for the two periods over ocean and land. Warming over land shows the same annual cycle as that over the ocean but with smaller amplitude, with increases of 3.3 °C and 1.3 °C for December and May, respectively. The similarity between the annual cycle of the temperature anomalies for the RILE and post-RILE periods, generally 0.5 °C apart, shows a transition towards warmer climate despite the relative recuperation of the sea ice cover in the post-RILE period. This is probably caused by the low thickness of the ice incapable of effectively insulating the atmosphere from the ocean combined with the general warming trend likely caused by increased GHG concentration, since most of the warming over land isn't statistically significant when the 100-year trend is removed (Fig. 1.8a).

The 2 m-air temperature response during the event (Fig. 1.8) showed maximum increases in temperatures over the East Siberian Sea in November-December caused by a delay in the ice formation over that region. The regional maximum warming is clearly visible over the Siberian Sea sector, defined between 110-190°E and 65-90°N (Fig. 1.14) with warming from 7.2 to 8.1 °C in December, 3 °C larger compared to the average Arctic Ocean warming. Despite the increased ocean warming over the East Siberian Sea, the nearby coastal area between 110-190 °N and from 65 °N to the coast shows smaller response with increases of 3.7 °C, corresponding to increased warming between 0.4 and 1 °C compared to Arctic Land.

Nevertheless, one would expect the warmer air present over the ocean to be advected over land by the anticyclonic circulation over the region (not shown). The rapid attenuation of the warming over land raises the question of the atmospheric heat transport mechanism, which is addressed in the next section.

1.4.3.3 Impact of RILEs on atmospheric structure

One would expect near-surface horizontal propagation of the warming signal due to the strong atmospheric stability caused by the Arctic low-level inversion. Studies by Deser et al. (2010) and Lawrence et al. (2008) showed propagation of a more uniform latitudinal warming over the continent, penetrating up to 1,500km inland, a signal very different in RCAO projections (Figs. 1.8 & 1.14).

To understand the propagation of the warming signal, a comparison of spatially averaged November-December vertical temperature profiles for pre-RILE and RILE periods as simulated by RCAO is presented in Fig. 15. Very weak low-level temperature inversion is noted from the profiles over the Arctic Ocean for both pre-RILE and RILE periods (~1 °C). Inversions of 2.8 °C and 4.2 °C are visible in the pre-RILE profiles for the East Siberian Sea and nearby land respectively, limited between the surface and 925 hPa. The Siberian Sea inversion disappears during RILE while the Siberian land inversion is reduced to 2.8 °C. While the warming signal is, as expected, strongest near the surface, temperature increases in the vertical, reaching heights of 500 hPa and above. This indicates an equivalent-barotropic structure to the warm anomaly; such structure is as expected associated with rather weak horizontal transport of heat from the oceanic region towards the continent. In present-day observations, strong linear relation has been demonstrated between the low-level inversion strength and the density of the underlying sea ice cover (Pavelsky et al. 2011). It is very likely that in the transient RCAO climate projections, the progressive decrease in the sea ice cover and thickness leads to gradual erosion of the atmospheric inversion. This reduced atmospheric stability might explain the vertical propagation of the surface warming during the events, therefore reducing their effects on surrounding continental areas.

1.5 Discussion & conclusions

The regional climate projections performed using the Rossby Center Atmosphere-Ocean modeling system produced four rapid ice loss events within three transient climate projections. The clustering of the major sea ice loss events around 2040 is caused by the combined effects of long-term sea ice thinning and large-scale atmospheric and oceanic

circulation anomalies originating from the common ECHAM lateral boundary conditions used to drive all three RCAO projections. The anomalous atmospheric and ocean northward flow causes increased heat transport from the Nordic Seas towards the Arctic region. The increased heat transport reaching the Barents Sea Shelf causes sea ice reduction over Barents Sea and in the vicinity of the North Pole. Similar mechanisms were suggested by Francis and Hunter (2007) based on observations and by H08 using results from CCSM3.

Although the maximal changes in the sea ice cover occurs in September, changes in surface variables are maximal during early winter (November-December) and are driven by the changes in the net energy flux. The net energy flux is mainly influenced by the increase in the turbulent latent and sensible heat fluxes. Compared to the more idealized study of Deser et al. (2010), results obtained in RCAO transient climate projections show more moderate changes in most of the atmospheric variables, especially the erosion of the Arctic wintertime inversion, the precipitation, and the snow cover (not shown). Nevertheless, the temporal changes in the surface energy fluxes are in good agreement with that of Deser et al. (2010), showing similar seasonality and comparable mechanisms albeit the differences in the spatial patterns.

Over Beaufort Sea, a sea ice-albedo feedback occurs over the retreating sea ice marginal zones. This sea ice-albedo feedback is triggered by anomalous circulation pushing the ice from the coastal areas towards the center of the Beaufort Sea, causing an increase in the absorption of solar radiation by the ocean. The increase in the energy absorbed by the ocean causes an increase in the SSTs and bottom melting along the retreating sea ice margin. Although anomalies in surface fluxes are weaker compared to the observation during the sea ice minimum of 2007 (Kay et al., 2008), the presence of thin ice in RCAO allowed large sea ice cover reduction despite the smaller anomalies simulated in the surface radiative fluxes.

RCAO shows increased variability in the sea ice cover after the RILEs. This result strongly suggests an increased sensitivity of the sea ice cover to changes in the large-scale atmospheric circulation and the surface radiative fluxes, leading to the partial recovery period observed during the post-RILE period. Despite the increased post-RILE sea ice cover variability, both in space and time, the 2 m-air temperature shows signs of a transition from colder pre-RILE to generally warmer post-RILE. This transition present over the Arctic

Ocean and peripheral land areas suggests decreased control of the sea ice cover on atmospheric variables potentially due to reduced insulation efficiency of thin sea ice.

The differences in the geographic location of the temperature changes between RILEs show a strong relationship between the regional response and the location of sea ice in RCAO. Lawrence et al. (2008) showed maximum warming over land in the CAA region while R2 event shows maximum differences over Oriental Siberia, caused by the maximum decrease in sea ice cover and thickness occurring upwind of that specific location in this particular event. Moreover, event R3, with maximal sea ice loss in the vicinity of the North Pole showed very little impact on land simply because the warm anomaly was advected southward toward the Greenland Sea, influencing no land masses along its path. The limited impact on land is caused by the vertical propagation of the surface heat anomaly rather than horizontal, caused by the absence of low-level temperature inversion over the ocean. Previous studies during recent-past, showed strong relation between the inversion strength and the sea ice cover but in the context of a transient climate change experiment, it is likely that the progressive thinning of the ice causes decreased surface cooling that gradually erodes the inversion.

It has been shown that RCAO sea ice cover and thickness suffers from relatively large biases in the atmospheric large-scale circulation over the Central Arctic basin caused by a quasi-permanent anticyclonic gyre combined with underestimation of its interannual variability. This bias in the sea level pressure, present in many coupled climate models, causes erroneous surface forcing acting on the sea ice and is responsible for the displacement of the maximum sea ice thickness towards the Siberian coast. The causes for this artificial anticyclonic circulation over the Arctic basin in numerical models are still poorly understood at this point. Furthermore, the stability of the anticyclonic circulation throughout the RCAO climate projection tends to generate large region of positive sea surface height (SSH) anomaly over the Arctic, decreasing the gradient between Bering and Beaufort Sea, therefore reducing the Bering Strait inflow (not shown). Studies of the 2007 event showed that increased heat transport through Bering Strait (Woodgate et al. 2010) was a factor in triggering the early sea ice retreat along the Alaska coast, most likely allowing the onset of sea ice-albedo feedback (Steele et al. 2010). The underestimation of Bering Strait inflow in

RCAO limits the ability of the ocean to produce RILEs originating from the Pacific Sector of the Arctic Ocean, explaining the "Atlantic origin" of the events presented in this study. However, the 2012 September sea ice minimum was related to large sea ice reduction both in the Pacific and Atlantic sectors, indicating RILEs with "Atlantic origin" are possible and their analysis relevant.

Compared to observations, to ECHAM, and other modeling studies, RCAO produces thinner ice for the recent past period (1980–1999), likely due to its warm near-surface temperature bias and the absence of a multi-category sea ice scheme. The thinner ice most likely increases the vulnerability of the modeled ice pack to changes in large-scale forcings and changes in the radiative fluxes, especially after decades of warming due to the increase in GHG concentration.

The ECHAM realization used to provide the atmospheric (and oceanic) lateral boundary conditions shares similar large-scale atmospheric circulation biases. This circulation anomaly, combined with the cold biases in ECHAM climatology explains the overestimated sea ice volume compared to observations and the large difference in sea ice volume compared to RCAO throughout the climate projections (Koenigk et al. 2011). Despite very similar large-scale atmospheric anomalies in ECHAM propagating into RCAO, the presence of thicker ice in ECHAM most likely decreases the sea ice vulnerability. This explains the absence of the 2040–2055 RILEs in ECHAM.

This study confirms that large-scale atmospheric anomaly is a key-element for triggering RILEs in RCAO projections combined with the preconditioning by long-term thinning of the sea ice. These results strengthen the conclusions found in DK, based on a much broader range of events of smaller amplitude. Moreover, it demonstrates the strong control of the driving GCM on the timing and synchronicity of RILEs. Future work is required to address this issue more thoroughly by performing ensemble of simulations driven by several GCMs at RCAO atmospheric and oceanic lateral boundaries. This will help assess the relative role of the driving model on RCAO solutions over the Arctic region. In-depth analysis of this relevant aspect will be possible within the framework of the COordinated Regional Downscaling Experiment, CORDEX, that is presently underway with RCAO as one of the participating models (http://www.meteo.unican.es/en/projects/CORDEX).

Table 1.1: Details of RCAO projections

Experiment	**North Atlantic Boundary**	**Sea surface salinity correction method**
ECHstand2	PHC climatology	Salinity relaxation
ECHMPIstand	ECHAM5/MPI-OM	Salinity relaxation
ECHMPIflux	ECHAM5/MPI-OM	Flux correction

Table 1.2: RILE summary

Rile identification	**Projection**	**Central Date**	**Period**	**Length**
R1	ECHstand2	2041	2039-2041	3
R2	ECHMPIstand	2039	2036-2043	8
R3	ECHMPIflux	2040	2036-2041	6
R4	ECHstand2	2063	2059-2063	5

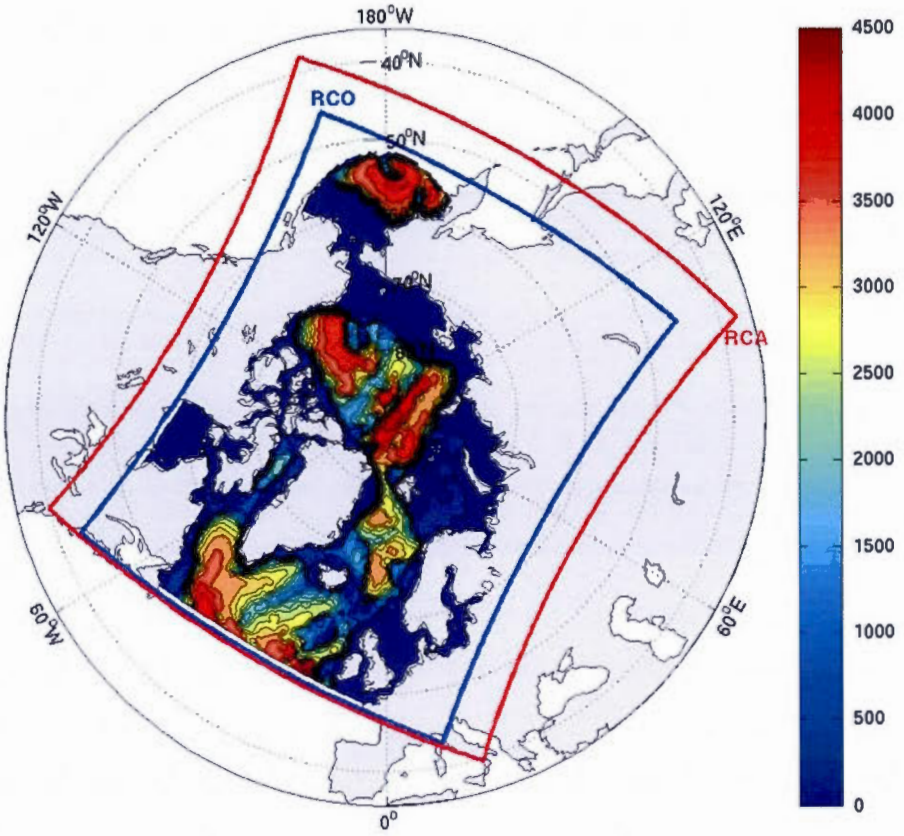

Figure 1.1: RCAO arctic domain and bathymetry (m).

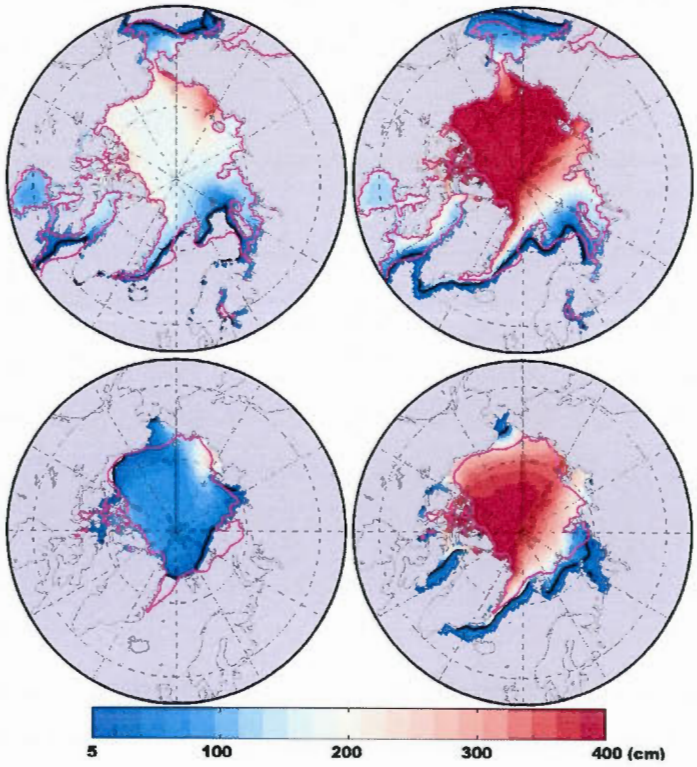

Figure 1.2: 1980-1999 average sea ice thickness (cm) and sea ice margin (SIC>15%; black contours) for the ensemble mean of the three RCAO climate projections (left) and ECHAM5/MPI-OM (right) for March (top) and September (bottom). ERA-Interim sea ice margin location is shown in magenta contour.

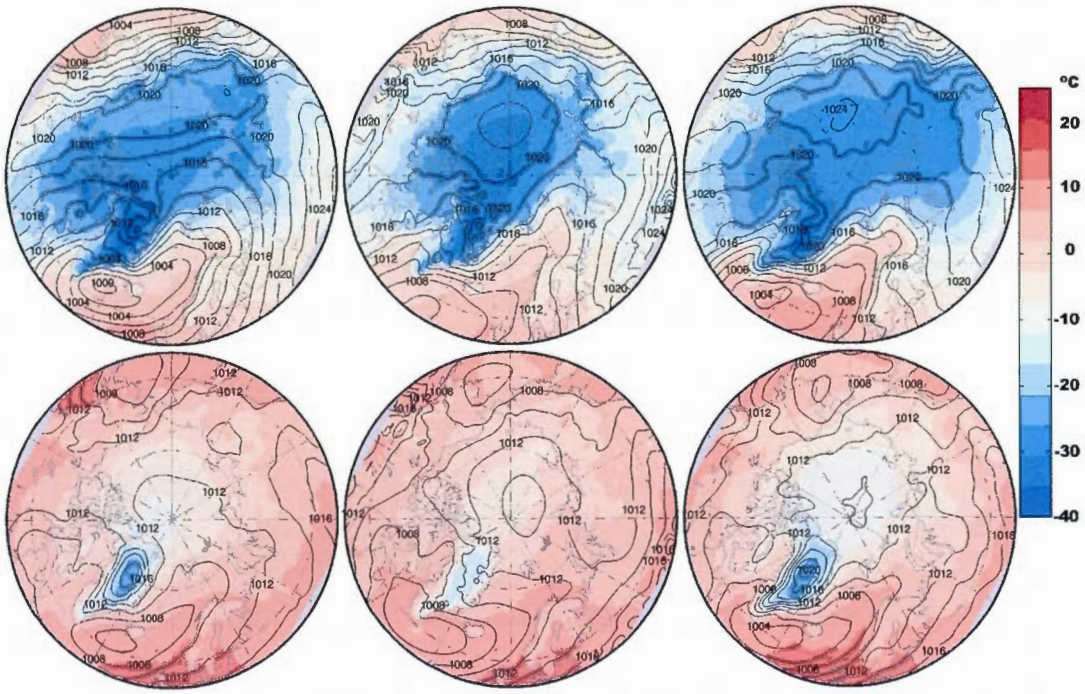

Figure 1.3: 1980-1999 average of 2 m-air temperature (°C; colors) and sea level pressure (hPa; contours) for ERA-Interim (left), ensemble mean of the three RCAO projections (middle) and ECHAM (right) for March (top) and September (bottom).

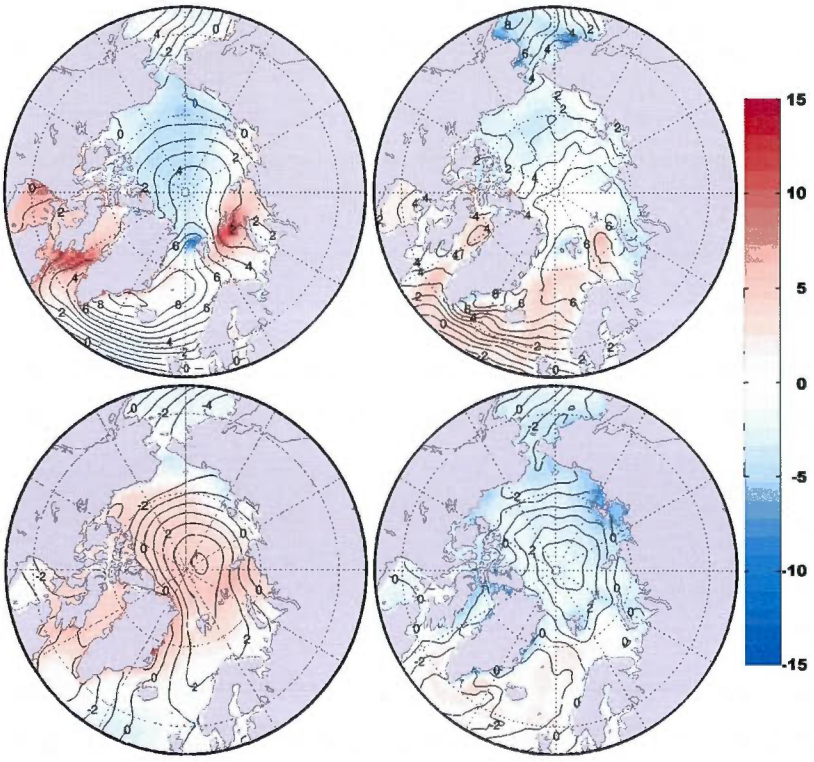

Figure 1.4: 1980-1999 differences for 2 m-air temperature (°C; colors) and sea level pressure (hPa; contours) between RCAO minus ERA-Interim (left) and ECHAM minus Era-Interim (right) for March (top) and September (bottom).

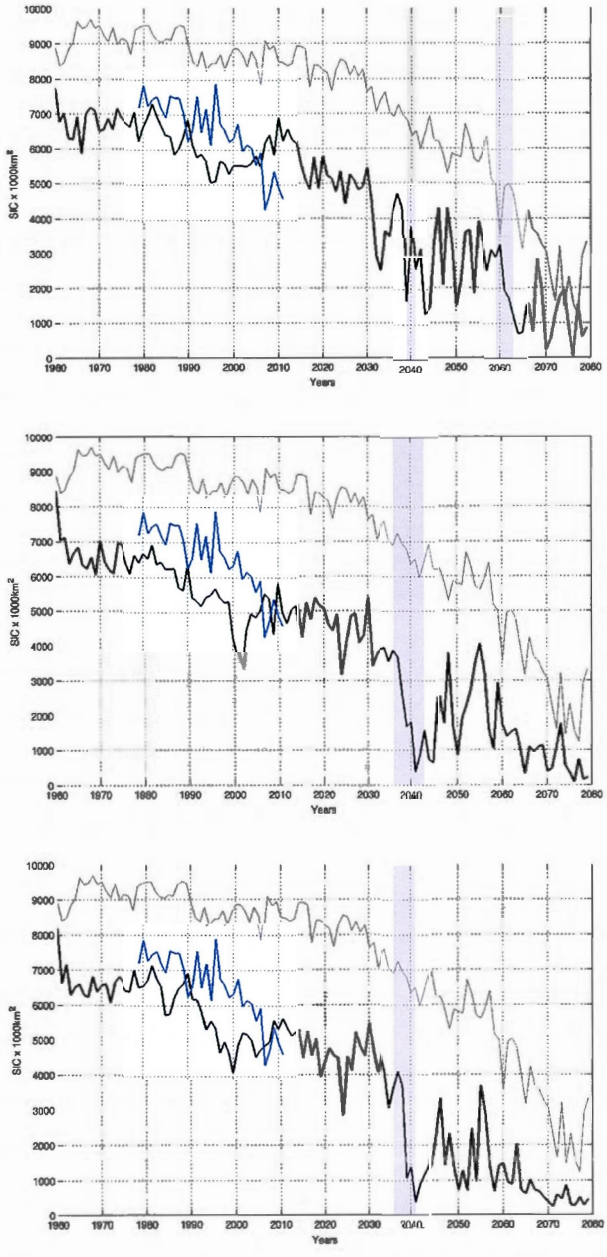

Figure 1.5: RCAO simulated September sea ice extent is shown in black for the 1980–2080 period: ECHstand2 (top), ECHMPIstand (middle) and ECHMPIflux (bottom). Grey shadings indicate Rapid Ice Loss Events considered in this study (Table 1.2). ECHAM and satellite observations (Fetterer et al., 2002; *updated 2011*) of September sea ice extent are presented in light grey and blue, respectively, on all panels.

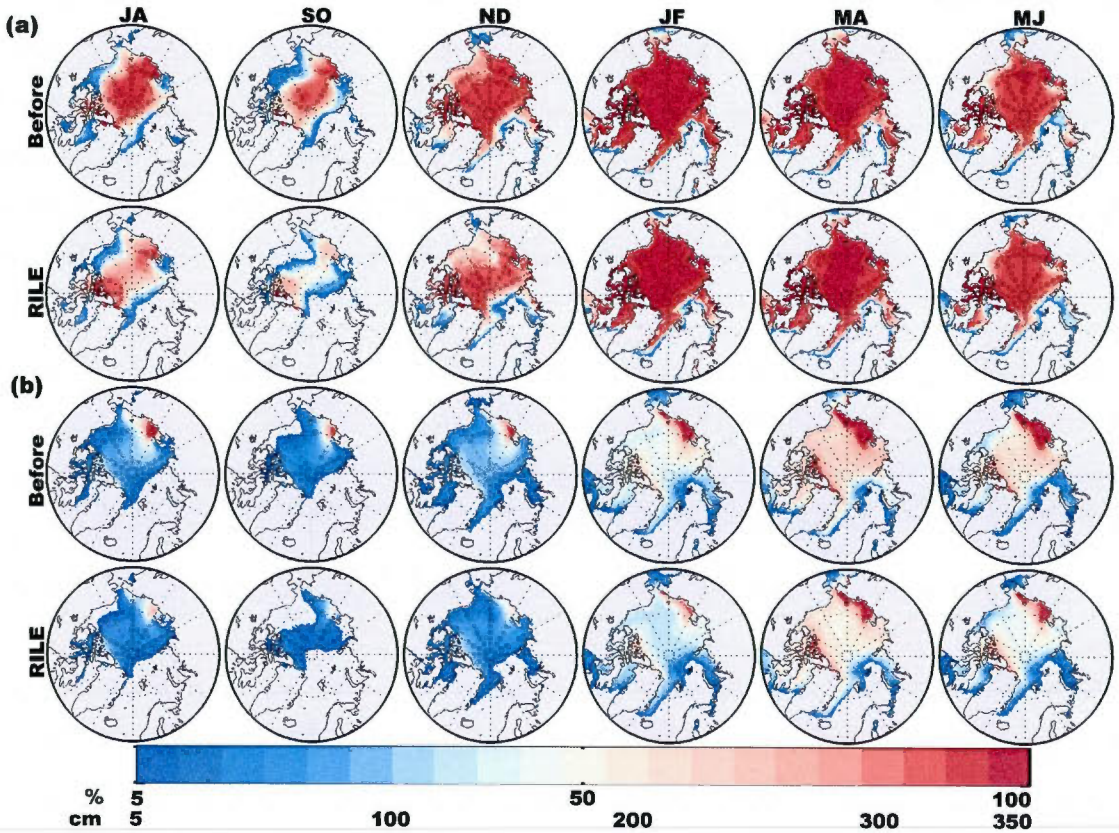

Figure 1.6: Bimonthly averages of (a) sea ice cover (fraction) and (b) thickness (cm) for pre-RILE (top) and RILE (bottom) period for R2 (2039 event, projection ECHMPIstand).

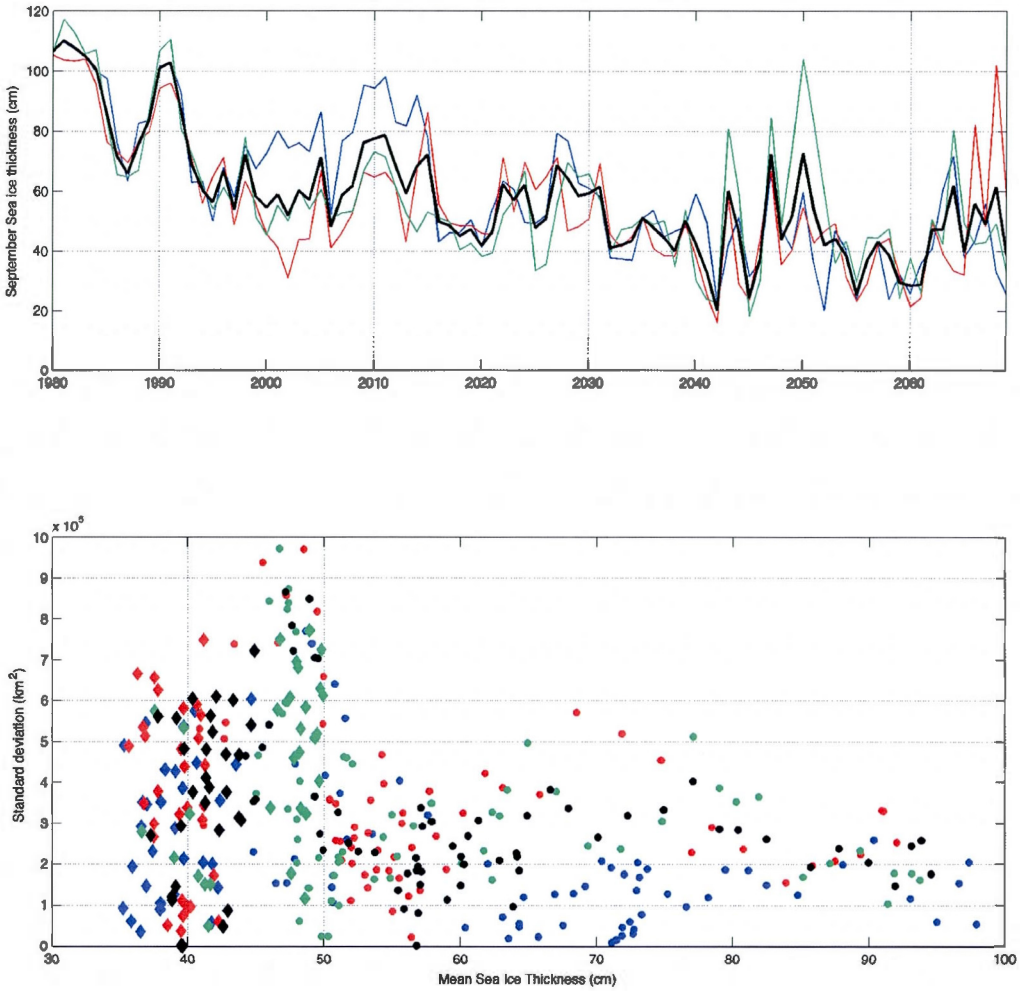

Figure 1.7: (top) Average September sea ice thickness for ECHStand2 (blue), ECHMPIStand (red), ECHMPIFlux (green) and ensemble average (black). (bottom) Relation between 20-year standard deviation of September Sea Ice Extent to 20-year average sea ice thickness. Dots are used for 1980–2040 period, while diamonds corresponds to the 2041–2070 period. Same color code as in the top panel with black symbols representing the ensemble average of the three simulations.

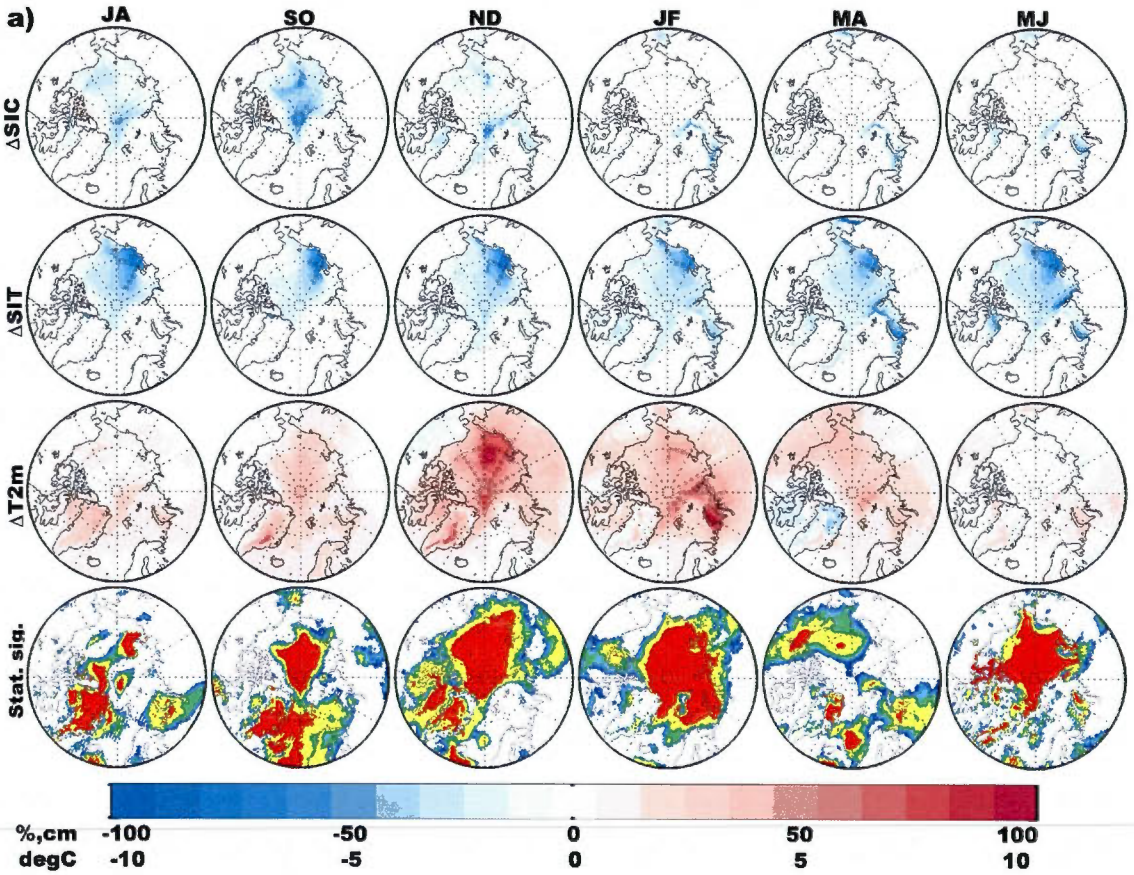

Figure 1.8a: Bimonthly differences of RILE-(Pre-RILE) averages for R2 event: sea ice cover (SIC, %), sea ice thickness (SIT, cm), 2 m-air temperature (T2M, °C) and statistical significance of the 2 m-air temperature following a t-test at significance levels: 80%-blue, 90%-green, 95%-yellow and 99%-red. The 100-year trend in 2 m-air temperature was removed prior to statistical significance testing.

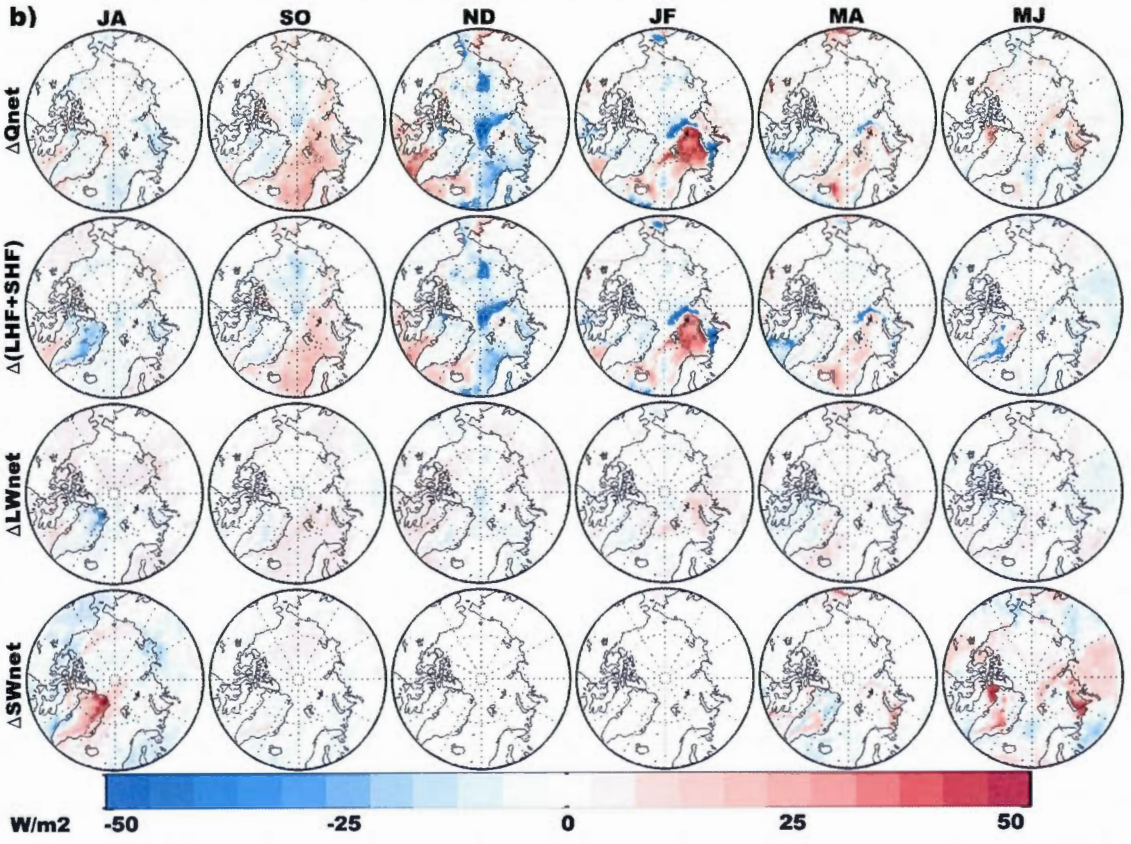

Figure 1.8b: same as Fig. 1.8a but for: surface net radiative balance (Q_{net}, Wm^{-2}), combined latent and sensible heat fluxes (LHF+SHF, Wm^{-2}), net surface longwave (LW_{net}, Wm^{-2}), and net surface shortwave (Q_{net}, Wm^{-2}). Fluxes are defined negative upward with respect to the surface.

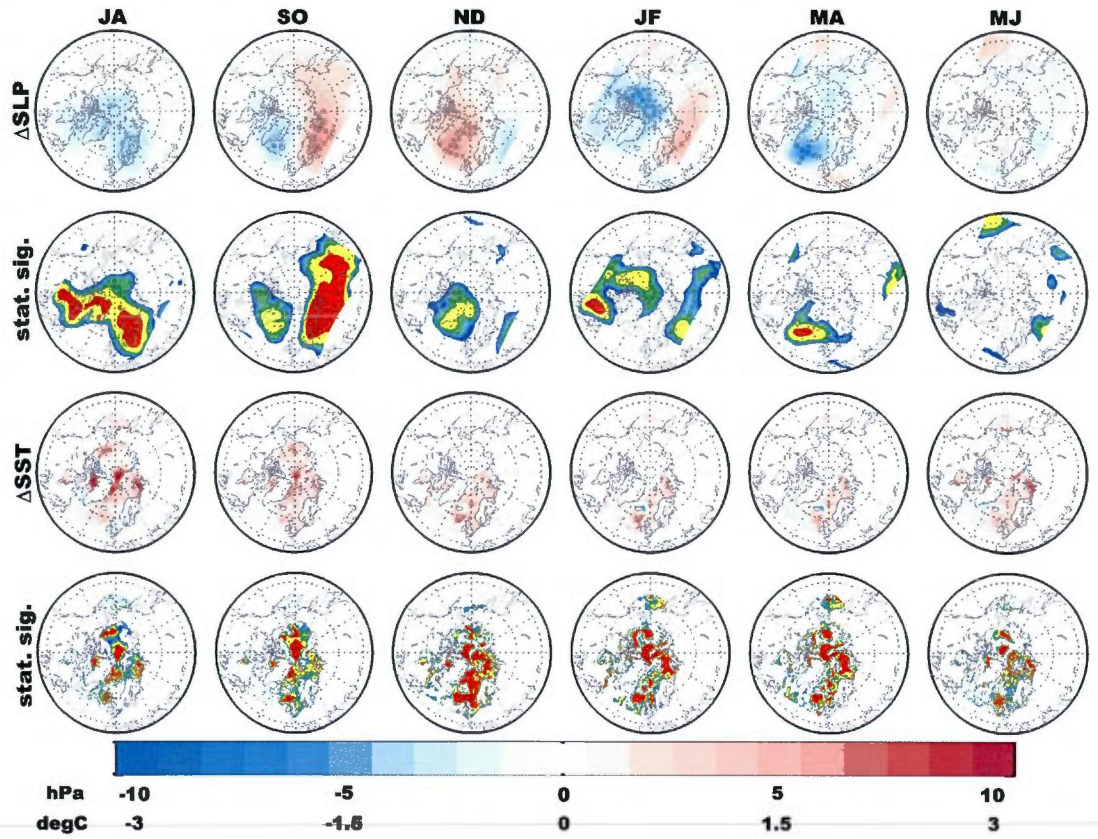

Figure 1.9: Bimonthly differences of RILE-(Pre-RILE) averages for R2 event sea level pressure (1st row), sea surface temperature (3rd row) and their statistical significance (2nd and 4th row). The blue, green, yellow and red shadings correspond to 80%, 90%, 95% and 99% confidence levels of the statistical significance.

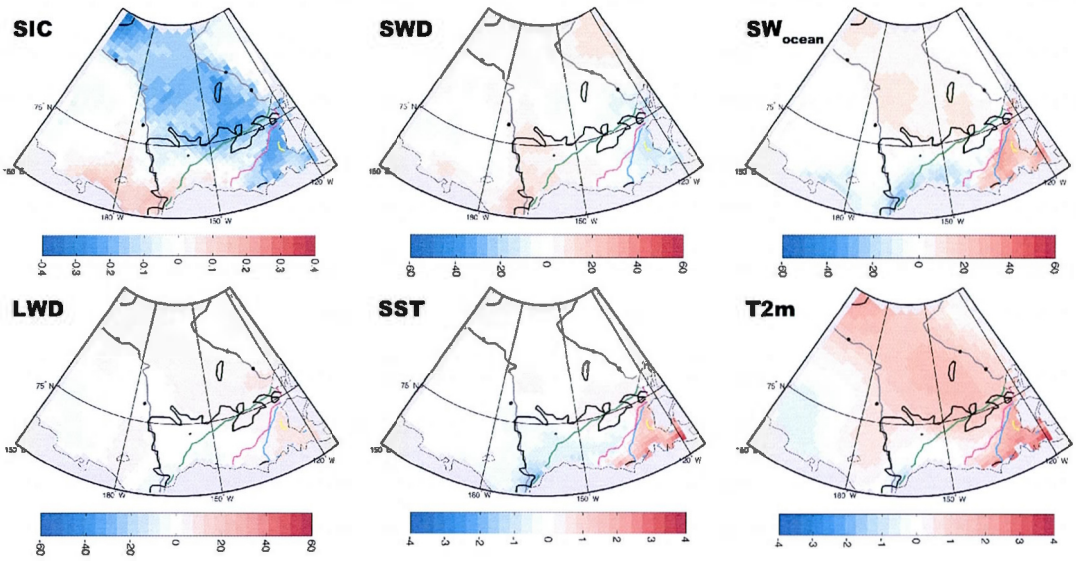

Figure 1.10: Average MJJASO anomalies between 2041 against the 2010−2030 period for: sea ice cover (top left), shortwave radiation down at the surface (top middle), shortwave radiation absorbed by the ocean (top right), longwave radiation down at the surface (bottom left), sea surface temperature (bottom middle) and 2 m-air temperature (bottom right). Radiative flux anomalies are presented in Wm^{-2} and temperatures anomalies in °C. Contours show the location of the 2041 sea ice margin (sea ice cover > 15%) for June (yellow), July (cyan), August (green), September (grey) and October (black).

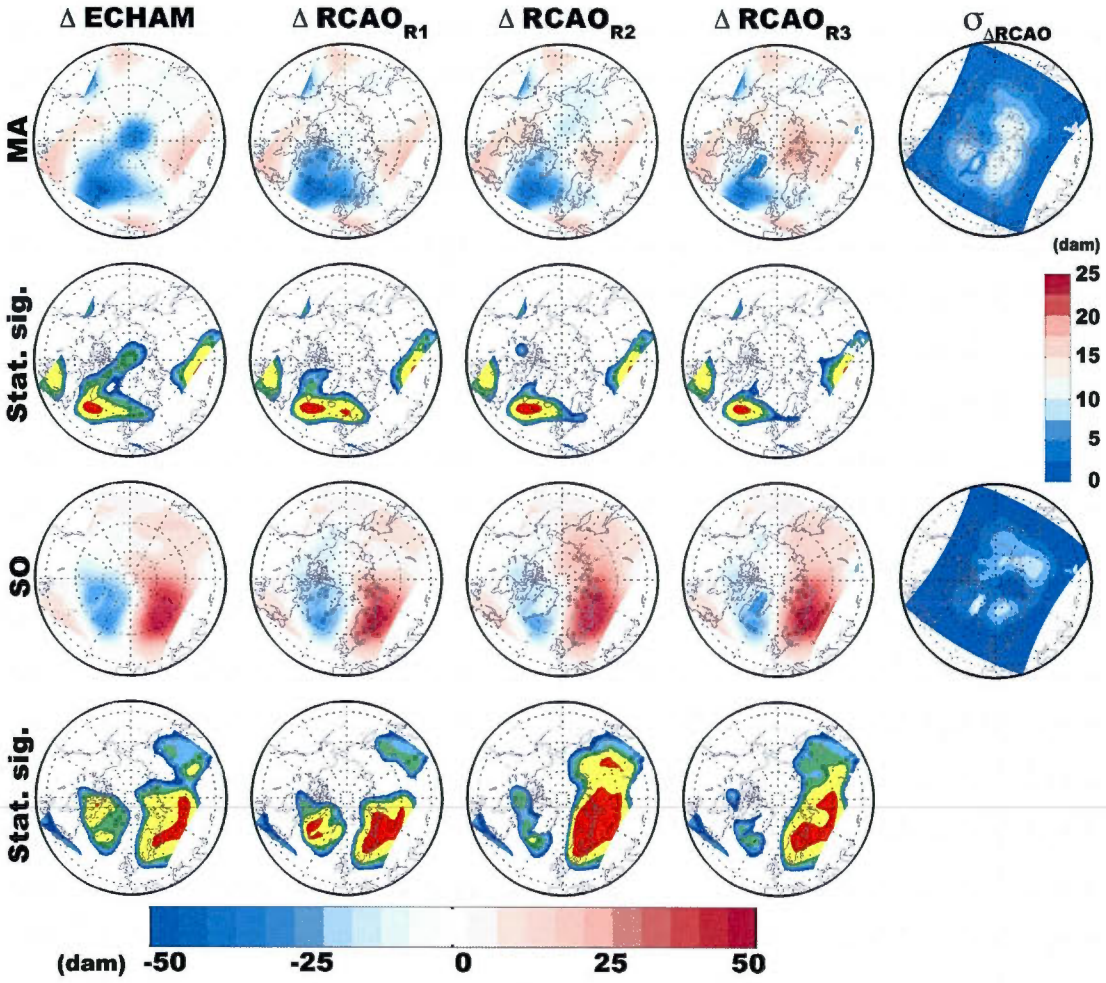

Figure 1.11: Changes in 850 hPa geopotential height for March-April (first row), statistical significance (second row), September-October (third row) and its statistical significance (fourth row) between period around RILEs (2036–2042) and the preceding 10-year period (2026–2035) for the driving model ECHAM, RCAO events R1, R2 and R3, from left to right respectively. The blue, green, yellow and red shadings correspond to 80%, 90%, 95% and 99% confidence levels of the statistical significance of a t-test. The last column represents the standard deviation amongst RCAO for the three projections.

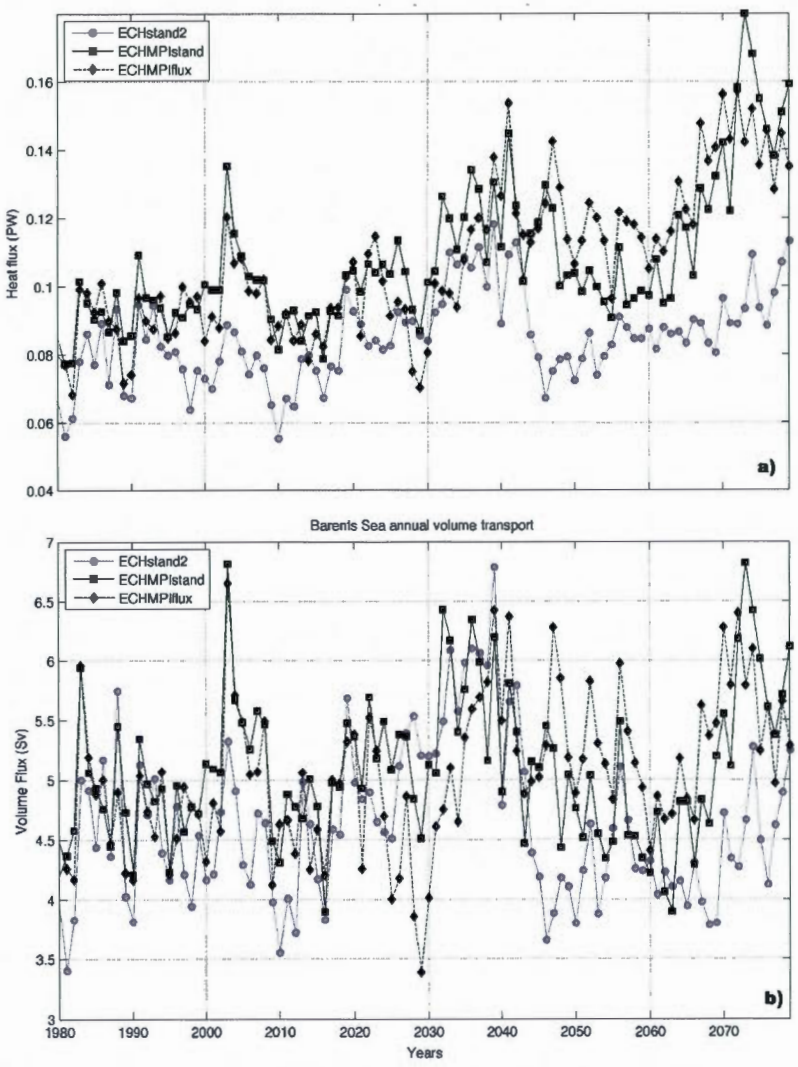

Figure 1.12: Time series of the Barents Sea opening annual (a) oceanic heat transport (PW) and (b) volume transport (Sv) computed using a reference temperature of -0.1 °C over the first 290 m (model first 25 vertical levels) for three RCAO climate projections: ECHstand2 (grey line), ECHMPIstand (black solid line) and ECHMPIflux (black dashed line).

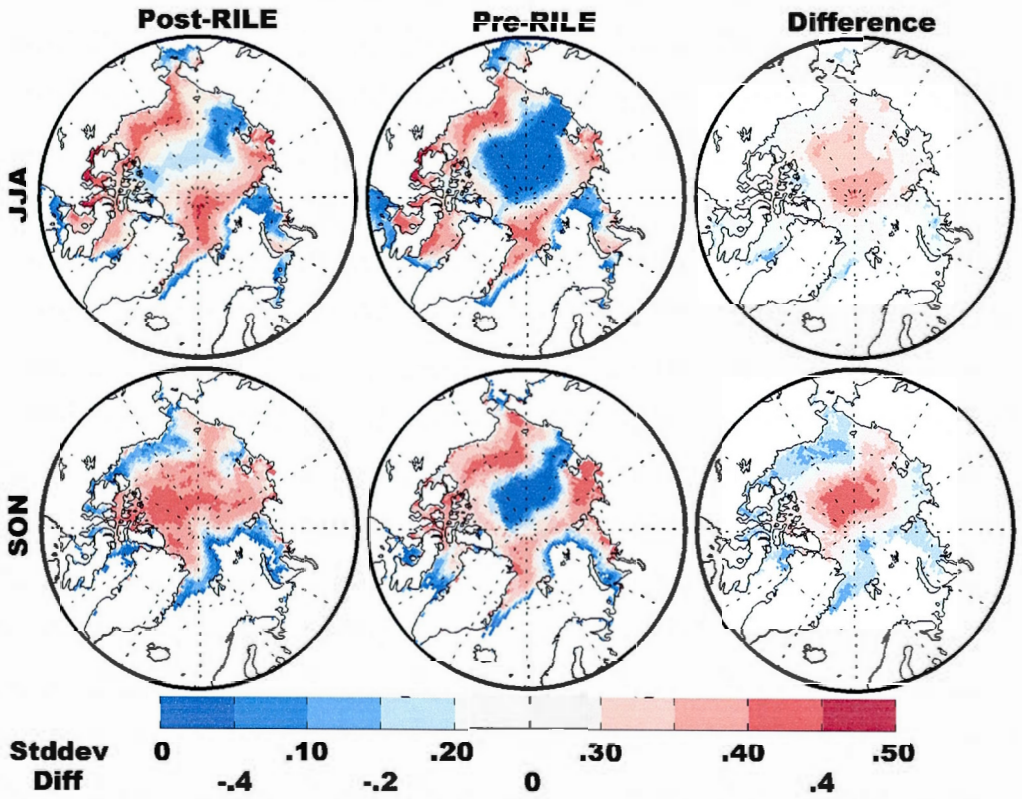

Figure 1.13: Summer and autumn seasonal standard deviation of sea ice cover for post-RILE (left), pre-RILE (middle) and their differences (right) for R2 event.

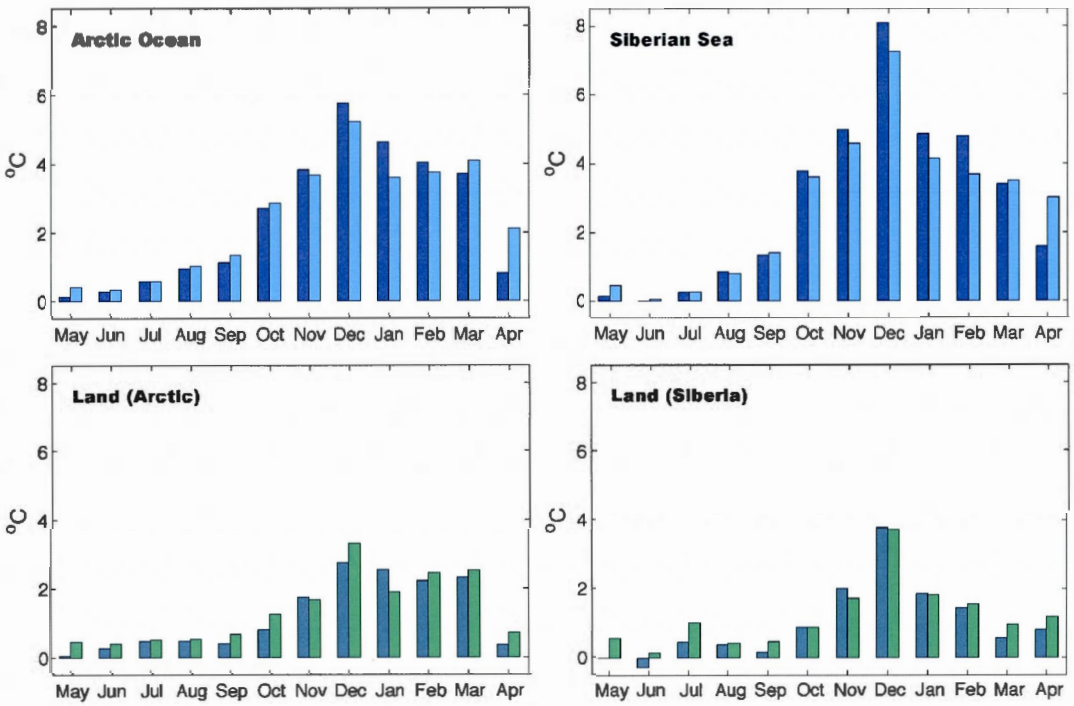

Fig 1.14: 2 m air temperatures differences for RILE minus Pre-RILE periods (dark colors) and Post-RILE minus Pre-RILE (light colors) over the Arctic Ocean (top left), Arctic Land (bottom left), Siberian Sea (top right) and Siberian Land (bottom right). Arctic land is defined between 45-290°E and between 65°N and the coast while the Siberian sector is defined between 110-190°E and 65-90°N.

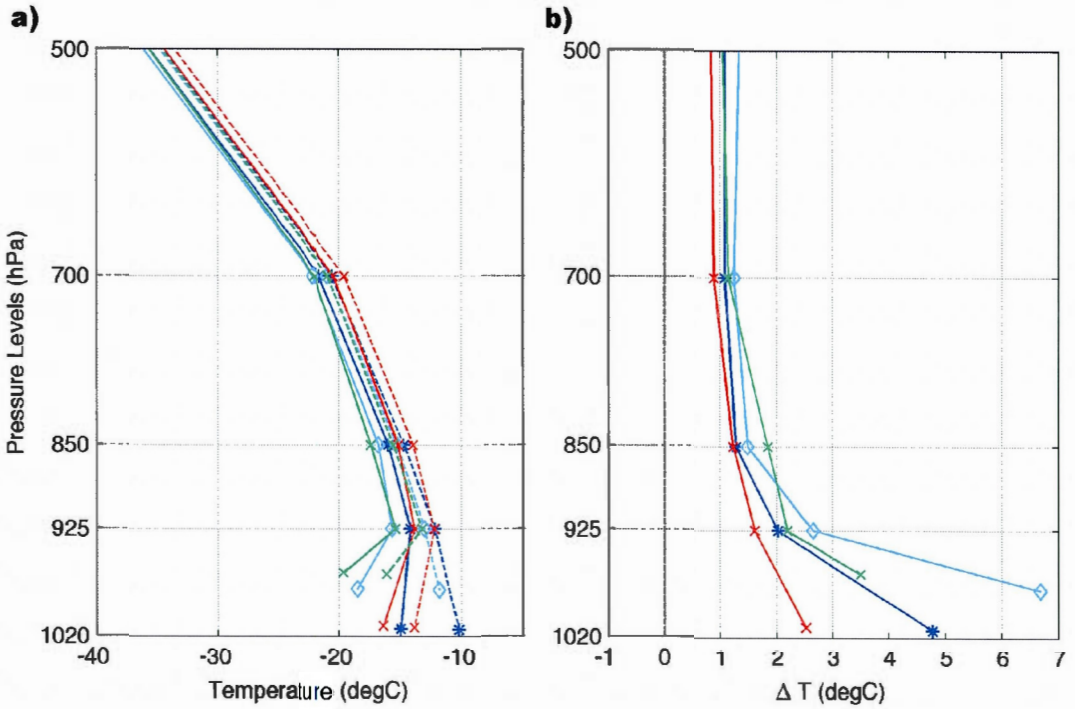

Figure 1.15: November-December (a) spatially averaged vertical temperature profile over Arctic Ocean (blue), Siberian Sea (cyan), pan-Arctic land (red) and Siberian Sea land sector (green) for Pre-RILE (full) and RILE periods (dotted). (b) differences RILE-(Pre-RILE) for same regions. The Arctic Ocean here is the region between latitudes 80-90°N between 90°W to 60°E and from 68-90°N from 60°E to 90°W. The Siberian Sea covers longitudes between 110°E to 190°E from the coastline to 90°N, while the Siberian Land covers land from 60°N to the coastline.

CHAPTER II

ON THE SIMULATED ARCTIC NEAR-SURFACE PERMAFROST AND CLIMATE SENSITIVITIES TO SOIL AND SNOW FORMULATIONS

This work has been submitted for publication in the peer-reviewed journal Climate Dynamics. The detailed reference is:

Paquin, J.-P. and L. Sushama. 2013. "On the simulated Arctic Near-Surface Permafrost and Climate Sensitivity to Soil and Snow Formulations". *In review in Climate Dynamics.*

Abstract

Near-surface permafrost has shown sign of warming on the Pan-Arctic scale in the recent decades. The fifth-generation of the Canadian Regional Climate Model (CRCM5) using the Canadian Land Surface Scheme (CLASS) in its standard configuration was underestimating the representation of the near-surface permafrost. This study tested successive improvements to the land surface scheme by (1) increasing the total soil column depth, (2) including the effects of organically rich soils and (3) modification to the snow density – snow thermal conductivity relation.

Stand-alone CLASS experiments showed successive improvements to the representation of the near-surface permafrost and simulated active layer thickness (ALT). Deepening the total soil column increased the near-surface permafrost area although the ALTs are generally overestimated. Adding organically rich soils decreased the summer ground heat flux, therefore cooling the soil column and thus improving the ALTs. The modification of the snow density – snow thermal conductivity relation reduced winter soil cooling, reducing the cold biases noted compared to observations. Similar effects were noted for coupled experiments. In coupled experiments, the decreased ground heat fluxes in summer caused by the representation of soil carbon, cause increased surface latent or sensible heat fluxes with spatial heterogeneity controlled by local soil moisture content. The inter-annual variability of the ALTs shows sensitivities to different atmospheric parameters depending on the soil and snow configuration. Over the 1960-2008 period, the positive ALT trends are caused by the warming of the simulated surface climate while the overestimated magnitude of the ALT is most likely related to the presence of a warm bias in the CRCM5 climatology.

Keywords: Regional climate model; land surface model; soil carbon; permafrost; active layer thickness

2.1. Introduction

Permafrost covers a significant area, i.e. approximately one quarter of all the exposed land of the continental northern hemisphere (Zhang et al. 1999). Many recent studies (Lemke et al. 2007) suggest increases in soil temperatures in these permafrost regions, particularly during the last few decades. These increases in soil temperatures are reflected in the increasing tendency of the active layer thickness (ALT) – defined as the maximum annual thaw depth – and permafrost degradation. The environmental impacts of permafrost degradation are manifold: it can alter significantly the soil structure and hydrology of the region, can lead to the formation of thermokarst lakes and/or drainage of existing lakes and change wetlands and vegetation cover (Hinzman et al. 2005). Permafrost degradation is also of concern from the viewpoint of the large amounts of carbon (~1672 Pg of carbon; Tarnocai et al. 2009) that are currently sequestered in the region. Since majority of the microbial decomposition occurs in the seasonally thawed active layer (Nelson 2004), increases in the ALT and permafrost thaw will increase decomposition of the sequestered organic matter, resulting in the release of carbon dioxide and/or methane. The decomposition process will release carbon dioxide or methane, depending on the type of decomposition, i.e. aerobic or anaerobic, to the atmosphere. This release of greenhouse gases associated with permafrost thaw will act as a positive feedback to climate warming. This has been evaluated to be between 2.8 °C and 7.8 °C by the end of the Century (Solomon et al. 2007) without the inclusion of this potential positive feedback. Climate models still do not consider all these above factors adequately, which contribute to large uncertainties in the projected climate changes.

The observed changes in soil temperatures, ALT and near-surface permafrost are not only related to higher temperatures, but also to changes in snow cover extent and duration (Zhang et al. 2005; Lemke et al. 2007; Frauenfeld and Zhang 2011). Most of the permafrost studies available to date are based on Land Surface Model (LSM) simulations driven by observed meteorological data (Oelke et al. 2004; Dankers et al. 2011; Burke et al. 2013) or

outputs from Global and Regional Climate Models (Sushama et al. 2007; Lawrence et al. 2008; Schaefer et al. 2011; Koven et al. 2011). These offline LSM simulations have provided important insights related to the evolution of permafrost, but do not represent the two-way feedbacks between the land and the atmosphere. Efforts to simulate permafrost interactively in climate models, both global and regional, is currently an active area of research. Studies by Smerdon and Stieglitz (2006) and Alexeev et al. (2007) documented limitations of climate models in simulating near-surface permafrost. They report that realistic simulation of soil temperatures in cold permafrost regions using Land Surface Models (LSM) with a zero-flux bottom boundary condition requires a total soil column depth of at least 30 m. Furthermore, Nicolsky et al. (2007), Lawrence et al. (2008) and Dankers et al. (2011) demonstrated the need to include soil organic carbon (organically rich soils) in LSMs for realistic simulations of soil thermal and moisture regimes and therefore ALT and permafrost extent. This, in turn, is important for realistic surface energy and water partitioning at the surface (Lawrence and Slater 2008; Rinke et al. 2008). Indeed, organic material acts as an insulator because of its low thermal conductivity and relatively high heat content. Implementation of soil organic carbon in LSM leads to important cooling of the soil temperatures, especially during summer, allowing permafrost to be present at warmer annual temperatures than if only mineral soils were represented in the LSM (Lawrence and Slater 2008; Rinke et al. 2008; Dankers et al. 2011).

Organic material also influences the soil moisture. In nature, organic soils are characterized by nearly saturated sub-surface conditions with a drier surface layer (Hinzman et al. 1991). Strong variability is observed in the soil moisture of the surface layer due to the efficient transport of water deeper in the soil column. This enhanced downward transport is due to increased porosity, high hydraulic conductivity and weak suction of organic material (Quinton and Gray 2003).

The simulated near-surface atmospheric fields in climate models will be sensitive to the parameterization method adopted for organic soils. Lawrence and Slater (2008) and Rinke et al. (2008) obtained different sensitivities of near-surface atmosphere to the implementation of soil organic material in their respective models. Lawrence and Slater (2008) showed large increase in the sensible heat flux over most of the high-latitude regions of the northern

hemisphere. These changes led to increased 2 m-air temperature, deeper and drier atmospheric boundary layer and reduced occurrence of low-level clouds. On the contrary, Rinke et al. (2008) obtained large increases in the latent heat flux, thereby cooling the surface temperature and enhancing low-level clouds. Given the large uncertainties in the atmospheric response, there is a need for more focused studies to identify the main reasons behind these uncertainties related to the representation of organic material in climate models.

The overall goal of this study is to improve the representation of the soil moisture and temperature regimes to better simulate the near-surface permafrost on a pan-Arctic scale. Two main objectives are presented in this study. The first objective is to assess the sensitivity of the Pan-Arctic soil temperature and moisture regimes to the depth of the soil model and to the implementation of a soil organic carbon parameterization and modified snow thermal conductivity through a series of offline simulations with the Canadian Land surface Scheme (CLASS). This allows an evaluation of the Pan-Arctic representation of permafrost conditions in CLASS excluding the complex land-atmosphere interactions and feedbacks. The second objective is to study the impact of the land surface model improvements, particularly the organic soil parameterization, in the fifth-generation of the Canadian Regional Climate Model (CRCM5), on the simulated permafrost, surface climate and land-atmosphere interactions through a series of CRCM5 simulations. It must be noted that the land surface model used in CRCM5 is CLASS. Evaluation of CRCM5's ability in capturing the observed near-surface permafrost conditions and trends is essential prior to performing future climate projections.

The outline of this paper is as follows. Section 2.2 provides a brief description of CLASS and CRCM5. Model configurations and the soil organic carbon parameterization are presented in Section 2.3. Section 2.4 details the observational datasets and reanalysis used in model evaluation. Analysis of the offline simulations performed with CLASS followed by that of CRCM5 simulations are presented in Section 2.5. Summary and conclusions are presented in Section 2.6.

2.2. Model description

The offline LSM simulations presented in this study are performed with CLASS (Verseghy 1991; Verseghy et al. 1993; Verseghy 2008), and the regional climate model used is a developmental version of the CRCM5 (Zadra et al. 2008; Martynov et al. 2013). As mentioned earlier, the LSM in CRCM5 is CLASS. A brief description of CLASS and CRCM5 follows.

2.2.1 The Canadian Land Surface Scheme

The basic prognostic variables in CLASS consist of the temperatures and the liquid and frozen moisture contents of the soil layers; the mass, temperature, density and albedo of the snow pack; the temperature and intercepted rain and snow on the vegetation canopy; the temperature and depth of ponded water on the soil surface; and an empirical vegetation growth index (Verseghy 2008). At each time step, CLASS calculates the characteristics of the vegetation canopy on the basis of the vegetation types present over the modeled area. In a pre-processing step, 23 surface and vegetation types with assigned background values of parameters such as albedo, roughness length, annual maximum and minimum leaf area index, rooting depth, etc. are aggregated over four main vegetation categories identified by CLASS: needleleaf trees, broadleaf trees, crops, and grass (Verseghy 2008). To account for subgrid-scale variability, CLASS models separately the changes to the energy and moisture budget over four subareas: bare soil, vegetation over bare soil, vegetation over snow and snow over bare soil.

CLASS is particularly suited for permafrost studies due to its flexible soil layer formulation. Each grid cell corresponds to a single soil profile of sand, clay and bedrock at the grid resolution computed independently, neglecting lateral heat and soil moisture transfers. Snow is modelled as a single variable depth layer. The effective thermal conductivity of snow, λ_s, is determined from the snow density, ρ_s, assumed constant with depth, described in Mellor et al. (1977):

$$\lambda_s = 2.576 \cdot 10^{-6} \rho_s^2 + 0.074$$

where λ_s, is in W m^{-1} K^{-1} and ρ_s is in kg m^{-3}. The magnitude of ρ_s increases exponentially with time from a fresh snow value of 100 kg m^{-3} to 300 kg m^{-3}, according to an expression derived from the field measurements of Longley (1960) and Gold (1958). CLASS treats refreezing of percolating melt-water or rain, which can lead to increases in snow density. After snowfall, ρ_s is recalculated as the weighted average of the previous density and that of the new snow.

2.2.2 The Canadian Regional Climate Model

The CRCM5 (Martynov et al. 2013) is based on a limited-area version of the Global Environment Multiscale (GEM) model used for Numerical Weather Prediction at Environment Canada (Côté et al., 1998). GEM employs semi-Lagrangian transport and (quasi) fully implicit marching scheme. The following parameterizations are used in CRCM5: deep convection following Kain and Fritsch (1990), shallow convection based on a transient version of Kuo (1965) scheme (Bélair et al. 2005), large-scale condensation (Sundqvist et al. 1989), correlated-K solar and terrestrial radiations (Li and Barker 2005), subgrid-scale orographic gravity-wave drag (McFarlane 1987), low-level orographic blocking (Zadra et al. 2003), and turbulent kinetic energy closure in the planetary boundary layer and vertical diffusion (Benoît et al. 1989; Delage and Girard 1992; Delage 1997).

2.3. Model setup

2.3.1 CLASS and CRCM5 configurations

A number of offline experiments are set up with CLASS to evaluate the performance of the model in representing the large-scale features of the permafrost distribution. To evaluate the sensitivity of the soil thermal and moisture regimes to the depth of the soil column, two configurations – shallow and deep – are considered. The shallow configuration uses 6 soil layers that are 0.1, 0.2, 0.3, 0.5, 0.9 and 1.5 m thick for a total depth of 3.5 m. In the deep configuration, 41 additional layers of 1.5 m thickness each were added to the

shallow configuration for a total of 47 levels reaching a total depth of 65 m.

All offline simulations are performed over a Pan-Arctic domain, at 0.5° horizontal resolution on a rotated latitude-longitude 172x160 points grid (Fig. 2.1a). CLASS uses sand and clay concentrations derived from Wilson and Henderson-Sellers (1985). Webb et al. (2000) is used for the depth to bedrock and therefore the depth of permeable soil layers in CLASS. If the depth to bedrock occurs within a soil layer rather than at the interface between two layers, CLASS assigns the specified soil characteristics to the part of the layer above bedrock, and values corresponding to rock to the portion below. Thermal conductivity of rock is the same as for sand, i.e. 2.5 W m^{-1} K^{-1}, with zero porosity. Figure 2.1b presents the number of permeable soil layers over the study domain.

The CRCM5 experiments use the exact same domain and grid as the CLASS offline simulations, with blending and sponge zones added to main analysis domain; CRCM5 simulations are performed with 56 atmospheric levels, with the model top at 0.1 hPa.

2.3.2 Soil carbon data and parameterization

In CLASS 3.5, high concentration of soil organic carbon can be represented with the peatland parameterization of Letts et al. (2000). This parameterization assumes that the entire soil column consists of organic material or peat. Three organic soil / peat classes, fibric, hemic and sapric, are considered for layers one, two and three and below to account for the effect of compaction of the organic material, with variations in the hydraulic properties of the uppermost 0.5 m of organic soil (Letts et al. 2000). It is to be noted that in this parameterization, bedrock can be located at any depth.

To account for organic material present outside of deep peatlands, a simple parameterization of soil organic carbon (SOC) has been introduced. This parameterization was implemeted to improve the representation of moderate concentration of organic material and thereby its influence on the surface fluxes, the surface and sub-surface thermal and hydraulic properties of the soil. This parameterization redistributes the observed SOC from

Global Soil Data Task Group of the International Geosphere-Biosphere Programme Data and Information System (IGBP-DIS) (Fig. 2.1c) assuming that high concentration of organic material is located at the surface, and the concentration decreases rapidly with depth. This assumption is reasonable since observational data is available only for the first 100 cm of the soil column. SOC from IGBP-DIS is interpolated from its original 1°x1° grid to the model grid. Vertical layers of CLASS are "filled" with organic carbon from the surface down until the observed soil carbon content is depleted. At the moment, no fractional percentage of soil organic carbon is allowed within a soil layer, resulting in either 100% organic carbon content or 100% mineral composition. For the vertical levels filled with organic material, the thermal and hydraulic properties follow Letts et al. (2000). The net effect is a 10 cm organic layer for most of the high latitudes (Fig. 2.1d) and 30 cm for certain grid points located in Scandinavia and in the Ob river valley.

The above implementation method is similar to that used by Rinke et al. (2008) where they assume that soil layers are entirely composed of SOC. Rinke et al. (2008) used three different organic classification: lichen, peat and moss, with parameters from Beringer et al. (2001) spatially distributed based on vegetation cover while in this study we distribute a single SOC with vertically varying parameters based on observed values from IGBP-DIS data. In this study, the net introduction of soil organic carbon concentrated near the surface with pure organic carbon in the first 10 cm of the soil column, which is similar to other studies although the implementation method used here is simpler. Implementation of SOC in the Community Land Surface Scheme (CLM; Lawrence and Slater 2008) and in the Joint UK Land Environment Simulator (JULES; Dankers et al. 2011) uses a redistribution of the observed SOC assuming vertically varying profiles and allows fractional SOC to be present at any soil layer. All methods have important limitations caused by the spatial heterogeneity of the soil carbon distribution. In reality, SOC is mostly accumulating in valleys and wetlands while ridges usually show limited SOC concentration.

2.3.3 Model experiments

To evaluate the impact of various formulations on the simulated near-surface permafrost and surface climate, four pairs of experiments are performed; each pair consists of a CLASS offline simulation and a matching CRCM5 simulation using identical CLASS formulations (Table 2.1). The first pair of simulations, Off_Mine6 and C_Mine6, uses the shallow 6-layer configuration without SOC. The second pair of simulations, Off_Mine47 and C_Mine47, uses the deep soil column with 47 layers for a total depth of 65m without SOC. These simulations are used to evaluate the sensitivity of the model solely to the vertical extension of the soil column and its impact on vertical propagation of heat. The third pair of simulation uses the deep vertical configuration and includes both the Letts et al. (2000) peatland parameterization and the SOC parameterization described in Section 2.3.2. While the third pair of simulation, i.e. Off_OM47 and C_OM47, uses CLASS standard snow conductivity of Mellor et al. (1977), the fourth pair, Off_OMSC47 and C_OMSC47, uses the quadratic relation between snow density and snow conductivity under varying snow conditions from Sturm et al. (1997):

$$\lambda_s = 0.023 + 0.234\rho_s \qquad \text{for } \{\rho_s < 0.156\}$$

$$\lambda_s = 0.138 - 1.01\rho_s + 3.233\rho_s^2 \qquad \text{for } \{0.156 \le \rho_s \le 0.6\}$$

This relation leads to reduced snow conductivity compared to the standard Mellor et al. (1977) formulation used in CLASS. Previous experiments using CLASS offline over selected sites in the Québec boreal forest showed improvements in simulated wintertime soil temperatures by using Sturm's formulation (Harvey et al. 2010). The fourth pair of simulations will thus enable assessment of the impact of new snow conductivity.

The offline CLASS simulations over the Pan-Arctic domain are driven by atmospheric forcings, i.e. precipitation, downward solar and longwave radiation, near-surface air-temperature and specific humidity, surface wind speed and air pressure, from ERA-40 reanalysis (Uppala et al. 2005) for the 1957−1994 period and by ERA-Interim (Dee et al. 2011) for the 1995−2008 period. ERA-40 and ERA-Interim reanalysis were spatially

interpolated from their original 2.5° and 1.5° grids, respectively, to the model grid at 0.5°. Both reanalysis were available at 6-hourly time interval, which were linearly interpolated to the model 30-minute time step. No temperature or precipitation corrections were applied to the reanalysis data. Soil temperature and moisture content were initialized using the respective fields from 200-year spinup runs using atmospheric boundary conditions from the 1970–1999 ERA-40 climatology. Two hundred year spinup runs were performed for each of the four CLASS offline experimental setups.

The CRCM5 simulations are driven at its lateral boundaries by ERA-40 and ERA-Interim reanalysis. All coupled experiments were spun-up for an additional 20 years using initial soil temperatures and moisture from the 200-year offline spinup runs discussed above. The lateral boundary conditions used to drive CRCM5 during the 20-year spinup corresponds to the year 1957 from ERA-40. This additional spinup was executed to make sure that the soil layer temperatures and moisture above 20 m depth were in equilibrium with the CRCM5 climate before executing hindcast experiments (not shown).

2.4. Large-scale data for model evaluation

2.4.1 Permafrost extent

The observed permafrost extent is derived from the International Permafrost Association (IPA) map (Brown et al. 2001). IPA classifies permafrost into four different categories based on the areal extent of permafrost: 90–100% coverage is considered continuous permafrost, 50–90% discontinuous, 10–50% sporadic and less than 10% isolated. The data from IPA represents an estimate of the permafrost extent valid mostly for the second half of the 20th Century (Burke et al. 2013). Given the resolution of the simulations, both offline and coupled, sporadic and isolated permafrost regions cannot be expected to be captured by the simulations. For this reason, simulated permafrost extent only for continuous and discontinuous regions will be compared to that observed.

2.4.2 Active layer thickness

The observed ALT dataset available from the Circumpolar Active Layer Monitoring program (CALM) (Brown et al. 2003; Brown 1998) is used to evaluate simulated ALTs. This dataset covers the 1990 to present period. The Arctic part of the CALM network consists of 79 stations mainly located in the arctic and sub-arctic lowlands. Three methods are mainly used to determine the ALT: by mechanical probing on a rectangular grid of 100 m x 100 m at 10 m spacing or 1000 m x 1000 m at 100 m spacing; by employing thaw tubes; or by inferring the thaw depth from ground temperature measurements recorded by thermistors. More details about the data and methodology are available on the CALM website (http://www.udel.edu/Geography/calm/index.html).

2.4.3 Russian historical soil temperature dataset

The at-site soil temperature observations over Russia (Zhang et al. 2001) used for evaluating simulated soil temperatures cover the 1882–1990 period. This dataset is a collection of monthly soil temperatures measured at meteorological stations for 13 different depths from 0.02 m to 3.2 m using bent stem thermometers, extraction thermometers, and electrical resistance thermistors. The stations are located in different climatic regions of Russia, between 35°E and 180°E, providing useful large-scale soil information for the evaluation of modeled soil temperatures. Although the original dataset covers period from 1882 to 1990, data coverage in space and time suffers from numerous gaps. Data concentration is relatively high in the 1980−1990 period and will constitute the reference period for comparison with model results. Measurements were generally performed over bare soil without a surface organic layer, which could lead to an overestimation of the seasonal cycle of temperature at depth (Gilichinsky et al. 1998).

2.4.4 Surface air temperature

The CRCM5 simulated 2 m-air temperature are compared against the European Reanalysis ERA-Interim (Dee et al. 2011) at 1.5° horizontal resolution and that of two station-based gridded observational datasets: the global gridded data from the University of Delaware (Udel; Willmott and Matsuura 1995) and from the Climatic Research Unit version 3.1 (CRU3.1; Mitchell and Jones 2005). These last two datasets combine weather station records and uses spatial interpolation methods to produce monthly means at 0.5° horizontal resolution over land.

2.4.5 Precipitation

As for 2 m-air temperatures, data from ERA-Interim and UDel are used for the evaluation of CRCM5 simulated precipitation. Precipitation data from the Global Precipitation Climatology Center (GPCC; Schneider et al. 2011) is also used in this study (Schneider et al. 2011). The version 6 of GPCC includes data from global stations to provide gridded monthly means of precipitation at 0.5° horizontal resolution for the 1951 to present period. No corrections were applied to any of the station-based observational datasests for the undercatch of solid precipitation in the Arctic.

2.4.6 Snow water equivalent

Two datasets of snow water equivalent (SWE) are used for model evaluation: the Global Snow Monitoring for Climate Research (GlobSnow; Luojus et al. 2010) version 1.2 and the Canadian Meteorological Center (CMC SWE; Brown and Brasnett 2010) snow analysis. The GlobSnow product is derived from a combination of ground based data and satellite microwave radiometer-based measurements. Due to the nature of the radiometer observations, the SWE product is reliable only over areas with seasonal dry snow cover. Areas with sporadic wet snow or a thin snow layer are not reliably detected and typically not present in the SWE product. The CMC SWE dataset consists of Northern Hemisphere snow depth analysis. Snow depth data is obtained from surface synoptic observations,

meteorological aviation reports, and special aviation reports. Monthly averages and climatologies of snow depth and estimated SWE are provided, where SWE was estimated using a density look-up table.

2.5. Results

2.5.1 Offline results

In this section, performance of CLASS in simulating the near-surface permafrost extent and soil temperature is evaluated by comparing with observations presented in Section 2.4. The sensitivity of simulated soil thermal and moisture regimes to soil column depth, inclusion of SOC and modification of the snow conductivity is also explored. The soil thaw depth is diagnosed from the simulated soil temperatures by fitting a linear temperature profile through the midpoints of each soil layer and calculating the depth at which the profile crosses the 0 °C isotherm. The thaw depth is computed for each month and the annual maximum thawing depth is defined as the Active Layer Thickness (ALT).

2.5.1.1 Permafrost extent

Figure 2.2 shows the observed (Brown et al. 2001) and CLASS simulated permafrost extent North of 45°N. To be defined as near-surface permafrost, the temperature of at least one soil layer in the top 5.0 m must remain below 0°C for 24 consecutive months.

The shallow 6-layer configuration, Off_Mine6, greatly underestimates the permafrost extent with 1.28 x 10^6 km^2 (Table 2.2), with ALT below 2.0 m limited to the Canadian Arctic Archipelago and the northernmost regions of Siberia. The model fails to capture the observed extent of permafrost, primarily due to the zero-flux boundary condition at 3.5 m, which leads to the overestimation of the simulated annual cycle of soil temperatures, as shown by Smerdon and Stieglitz (2006), letting all six soil layers to thaw regularly in summer.

Results from the Off_Mine47 experiment show that increasing the soil depth to 65 m substantially increases the near-surface permafrost extent. Comparison between the observed (13.25 $x10^6$ km^2) and simulated (12.27 $x10^6$ km^2) permafrost extent for continuous and discontinuous permafrost regions shows relatively good agreement, with an average simulated ALT of 2.2 m.

The incorporation of organic soils (Off_OM47) slightly increases the areal extent of continuous and discontinuous permafrost by 0.33 x 10^6 km^2 to a total of 12.60 x 10^6 km^2. As can be seen from Fig. 2.2, introduction of SOC in the model leads to limited extension of the near-surface permafrost at its southern limit. The major impact is a large decrease in the simulated ALT (1.69 m) over most of the permafrost regions. Since the ALT mainly represents the summer temperatures, the introduction of soil carbon in CLASS lowers summertime temperatures by insulating more effectively the deeper soil layers from the atmosphere as will be shown in detail in the following sections.

Combining SOC with snow conductivity from Strum et al. (1997) (Off_OMSC47) decreases near-surface permafrost extent compared to the SOC only experiment (Off_OM47) (Fig. 2.2). Permafrost is lost from the southern edge of the near-surface permafrost distribution but also in the continuous and discontinuous region, reaching 11.48 million km^2 compared to 12.6 x 10^6 km^2 for Off_OM47 (Table 2.2). Average ALT over the continuous and discontinuous region also increases up to 2.16 m, similar to the 2.21 m obtained for Off_Mine47. As will be demonstrated in the following sections, the decreased snow conductivity in Off_OMSC47 tends to increase the wintertime soil temperatures through increased insulation relative to Off_OM47.

2.5.1.2 Active Layer thickness

In this section, the simulated and observed ALTs are compared. It must be noted that comparison is only performed for those CALM sites, north of 60°N, with an altitude difference of less than 150 m with the average altitude of the representative grid cell. This way, stations where altitude differences could lead to significant mismatch in the surface

climate between the CALM site and the representative model grid are eliminated. As observed values are not available for all sites for the entire period, average observed and modeled values for the 1990–2008 period are compared.

Generally, the ALTs are overestimated compared to the observed values with averaged biases ranging from 39 cm to 122 cm (Fig. 2.3). The small biases for Off_Mine6 is due to the fact that only few site comparisons are possible due to the large underestimation of permafrost in this simulation (Fig. 2.2), with near-surface permafrost captured only over the coldest regions of the Canadian Arctic Archipelago and Siberia. The deep mineral, Off_Mine47, and deep organic with modified snow conductivity Off_OMSC47 show large average biases in simulated ALTs, 113 cm and 122 cm respectively, while the deep organic run Off_OM47 shows relatively smaller average bias of 71 cm.

Careful evaluation of the ALT shows larger overestimation of the ALT for CALM sites located inland, mostly along the Mackenzie River and Alaska where overestimation increases from coastal sites to those inland (not shown).

It should be noted that CLASS is run at relatively coarse horizontal resolution (0.5° x 0.5°), while observations are mainly point-scale or representative of a much smaller area (1 km^2), and therefore not very representative of large area means, in particular for complex terrain (Dankers et al. 2012; Oelke et al. 2003; Nelson et al. 1997). Moreover, grid-averaged soil properties and coarse-resolution atmospheric forcings might also introduce biases in the comparison between observed and simulated ALTs. Therefore, comparison between observed and simulated ALTs should be viewed as an indication of the model performance rather than a true in-situ validation. Nevertheless, results clearly show a general tendency to overestimate maximum thaw depth for all stations.

2.5.1.3 Soil temperatures

To evaluate CLASS simulated soil temperatures, we used the Russian Historical Temperature dataset (Zhang et al. 2001) presented in Section 2.4. For all observed soil levels,

stations located North of 55°N with at least one available value per month were selected. Monthly averages were computed over the 10-year period. All observed vertical levels falling within a model layer are averaged to maximize the number of stations for the comparison. Then, similar to ALT comparison, soil temperature comparisons are performed only for those observation stations with minimal differences in altitude with the representative grid cell.

Figure 2.4 shows a comparison of the mean annual soil temperatures at 0.2 m, 0.85 m and 2.75 m corresponding to the midpoints of the 2nd, 4th and 6th model soil layers. All simulations show relatively good agreement for regions with milder climate, while underestimates the mean annual soil temperatures at all levels for points located in colder regions. Nevertheless, the simulation using the deep configuration with SOC and modified snow conductivity (Off_OMSC47) shows smaller biases (less than -4.5°C) at all soil levels for stations between 35 and 100°E, while larger biases are noted for grid cells located between 100 and 190°E (Table 2.3). Interestingly, for stations in eastern Siberia, the experiment combining SOC and modified snow conductivity (Off_OMSC47) shows a net improvement of the biases compared to other simulations.

Figure 2.4 also presents the annual cycle of soil temperatures, which clearly show a strong wintertime cold bias. For all the stations (35–190°E), CLASS underestimates winter temperatures down to –8 °C in February at 0.2 m depth for all runs except Off_OMSC47 which tends to have smaller biases. The cold bias propagates down with attenuation of the signal reaching biases of –7 °C in April at 2.75 m for Off_Mine47 and Off_OM47. Surface air temperature used to drive the model shows no significant difference with the gridded dataset from UDel suggesting that differences are most likely due to the model formulation and/or due to the deficiencies in the representation of snow coverage and snow properties (Fig. 2.4). This later assumption is strongly supported by the lower biases associated with the simulated soil temperatures for Off_OMSC47, at all vertical levels in winter. Summer soil temperature is underestimated compared with observations and the introduction of the SOC further increases the cold biases near the surface compared to the mineral formulation. It must be noted that the top organic material is removed from the observational sites, most likely causing increased summer soil temperature and amplified annual cycle (Gilichinsky et al. 1998).

The shallow configuration Off_Mine6 tends to overestimate the annual cycle amplitude at 2.75 m as a result of the zero-flux bottom boundary conditions imposed at 3.5 m. This confirms the necessity to use deeper soil column configuration especially for high latitudes.

CLASS captures the annual cycle of the soil temperature reasonably well despite the systematic cold bias in winter. The introduction of SOC does impact the summertime temperatures, while modified snow thermal conductivity plays a major role in the improvement of wintertime soil temperatures.

2.5.1.4 Impact of organic matter implementation over Northwest Siberia

In this section, we evaluate the changes in the modeled soil temperatures over Northwest Siberia, specifically the region bounded by 55–90°E and 55–75°N, as this region is characterized by more permeable soil layers (Fig. 2.1b) and high concentration of SOC represented by deep peatlands and by the introduction of one or two layers of SOC over the area (Fig. 2.1d). Furthermore, soil temperatures are relatively well simulated for this region compared to observations (Table 2.3). Comparisons are performed relative to the Off_Mine47 experiments to isolate the effects of SOC and snow conductivity.

Figure 2.5 presents the monthly averaged soil temperatures over the West Siberian Plains from the surface down to 3.5 m. The shallow mineral experiment Off_Mine6 doesn't show large differences for the first 3 layers across the annual cycle compared to Off_Mine47, but the amplitude of the soil temperature annual cycle is overestimated at deeper levels compared to Off_Mine47 due to the zero-flux bottom boundary condition imposed at 3.5 m, as shown previously in Fig. 2.3.

Deep SOC configuration, Off_OM47, shows decreased summer soil temperature with reduced penetration of the 0 °C isotherm into the soil column, thus decreasing the average ALT over the region (Fig. 2.2). Compared to Off_Mine47, this experiment shows lower summer maximum temperatures in July with values of –5.4 °C and –5.56 °C at 0.2 m and

0.45 m respectively. This is due to the reduced summertime heat exchanges between the atmosphere and the soil due to the lower thermal conductivity of the SOC and increased soil water content (addressed in the next section). The ground heat flux is indeed reduced compared to both simulations using mineral soils (Fig. 2.6).

For the Off_OMSC47, summer temperatures are found lower than that of Off_Mine47 resulting from the insulating effect of the SOC. The temperature differences are smaller with minimum values of –4.23 °C and –4.25 °C in July at 0.2 m and 0.45 m respectively. Wintertime temperatures are significantly high in this experiment compared to the other deep configuration experiments due to the decreased snow thermal conductivity. In February, the soil temperatures are warmer by +5.03 °C and +4.25 °C at 0.2 m and 0.85 m respectively. This shows a large sensitivity of the simulated soil temperatures to the formulation of the snow thermal conductivity-snow density relation in CLASS. The increased winter temperature is caused by reduced heat flux from the soil to the atmosphere through the snow pack (Fig. 2.6), a direct consequence of the reduced snow thermal conductivity, which further reduces soil-atmosphere interactions in winter.

2.5.1.5 Changes in hydrology and surface soil variables over Northwest Siberia

The implementation of SOC has a direct effect on the hydrology associated with the increased porosity and soil hydraulic conductivity. This section evaluates the changes in the simulated hydrology over the Northwest Siberian Plains. Deep peatlands are present mostly over the southern part of the region while over the northern region, mainly one SOC layer is added (Fig. 2.1d). The number of permeable soil layers decrease from 6 (with total permeable depth of 3.5 m) in the southern part to 3 layers (with total permeable depth of 0.6 m) in the coastal area (Fig. 2.1b).

Figure 2.7 presents the average annual cycle of the main surface hydrological variables, for the 1990–2008 period. Soil liquid and frozen water contents of the first soil layer increases in the SOC experiments as a direct consequence of the increased soil porosity of the organic soil (0.93) compared to mineral soils (<0.49). The total summer water content,

i.e. liquid and solid combined, is reduced compared to winter due to increased evaporation in summer. The deep peatlands show larger increases of both water contents with values approaching saturation in winter, while non-peatland points show a more moderate increase (not shown).

The peaks in the surface runoff occur in May and June for all experiments and is related to the springtime snowmelt. The simulated differences in the surface runoff and the drainage are subject to many factors: the soil temperatures, the presence of permafrost, the presence of peatlands and changes in evapotranspiration. Drainage occurs at the bottom of the permeable soil depth, varying over the area between 0.6 m in the northern part to 3.5 m in the southern part (Fig. 2.1b). Therefore, for grid cells with permafrost and ALT shallower than the total depth of the permeable soil, drainage is inhibited, thus increasing the potential for surface runoffs. This situation is mostly present for the Off_OM47 simulation where most of the region doesn't allow drainage due to ALT shallower than the depth to bedrock (Fig. 2.2). The presence of shallow frozen ground therefore explains why Off_OM47 has minimum drainage and maximum surface runoff compared to other experiments. Coherently, the Off_OMSC47, with milder soil temperatures, earlier soil thaw and deeper ALT allows a higher fraction of the melt water to percolate into the soil.

The introduction of peatlands also alters runoff. Averages computed solely over peatlands show that drainage is almost zero resulting from the combined effects of frozen ground and due to Letts et al. (2000) formulation allowing a higher water retention capacity in the organic soils. Therefore, the decrease in drainage and the increase in the surface runoff during the late summer (July to September) are mostly due to the presence of peatlands over the area.

2.5.2 Results from CRCM5 experiments

While the offline simulations discussed in the section above helped assess the sensitivity of soil thermal and moisture regimes to modifications in the LSM in isolation, it is essential to use coupled land-atmosphere simulations to study the interactions and sensitivity

of surface climate to changes in soil and snow formulations. The CRCM5 simulations C_Mine6, C_Mine47, C_OM47 and C_OMSC47 will be analysed in this section and compared to the matching offline ones as required.

2.5.2.1 General model evaluation

The simulation of permafrost and soil conditions in a coupled land-atmosphere model is dependent on the quality of the simulated surface climate. Hence, a general evaluation of the CRCM5 performance against reanalysis and observational databases is presented here for key variables directly influencing the soil conditions: the 2 m-air temperature, precipitation and snow water equivalent. The model evaluation is presented for the deep mineral configuration (C_Mine47).

Figure 2.8 presents the simulated 2 m-air temperature for winter (DJF) and summer (JJA) and comparison with ERA-Interim, UDel and CRU3.1 datasets. Summer temperatures are relatively well simulated and biases are less than 4°C when compared to ERA-Interim over most of the domain. Compared to UDel, the model has a general cold bias over most of North America and East of the West Siberian Plains. Comparison with CRU3.1 dataset shows different bias patterns in the temperature, with several grid cells with warm biases (e.g. Kolyma Mountain Range). The differences in the two station-based climatological datasets UDel and CRU3.1 can be explained by the low density of the observational network in high latitudes and the differences in the interpolation methods used. One could see these differences between observed datasets as an approximate measure of the observational uncertainties.

Winter temperature shows systematic cold bias over Western Russia, interior Alaska and over the Rocky Mountains. Warm biases are widespread, with biases of 4 to 6 °C around Hudson Bay and over the Central Siberian Upland. Maximum warm biases are located in the Lena River Valley and in the surrounding mountainous regions (6 to 12 °C). Although biases are smaller in comparison with ERA-Interim, the existence of similar patterns in the comparison with all datasets, despite their observational uncertainties, lead to the conclusion that the CRCM5 has an important warm bias over these regions.

Figure 2.9 shows the simulated winter and summer precipitation fields and its comparison with ERA-Interim, UDel and GPCC datasets. Winter precipitation shows minimum precipitation located over the Arctic Ocean extending to the Canadian Arctic Archipelago and to Siberia, in good agreement with observations. Comparisons with ERA-Interim, UDel and GPCC show a general overestimation of winter precipitation over mountainous regions and generally over North American continental areas. A dry bias over West Siberian Plains is also present and is consistent in comparison with all datasets. One must note that uncertainties in wintertime precipitation are large mainly because of the undercatch of solid precipitation by ground-based observation stations, a systematic bias for which neither UDel nor GPCC have been corrected. One hypothesis for the underestimation of the precipitation over West Siberia is the underestimation of the Icelandic Low system in CRCM5 (not shown) that would limit the moisture transport from the Nordic Sea region towards Western Siberia while good agreement is noted over Central Siberia.

Simulated summer precipitation shows the important signature of complex topography over the whole domain with maximum values located over the Pacific Coast of North America and over Siberian Mountains of the Altai, Central Siberian Upland, the Kolyma and Stanovoy Range. This signature of complex topography is hardly visible in station-based observational datasets, most likely due to the scarcity of the stations network, leading to the systematic wet biases in those regions, especially over Russia, as seen in the difference fields. While the comparison with both station-based datasets show coherent biases (mostly wet) over the high latitudes of the continental North America, comparison with ERA-Interim shows a very different pattern with large dry bias over Alaska decreasing in magnitude towards Hudson Bay. These differences again reflect the large uncertainties in the measurement of precipitation and the representativeness of gridded datasets derived from stations compared to reanalysis products. In that sense, one might consider solely the regions where both station-based datasets and reanalysis biases are coherent as signs of significant biases in the CRCM5. Two regions, the West Siberian Plains and in the vicinity of Hudson Bay distinctly appear as areas where the simulated CRCM5 precipitation might suffer from a systematic dry precipitation bias. Although an important dry bias also exists south of the

Stanovoy Range, this region is not significant for the present study focusing on high-latitude temperature and permafrost.

Figure 2.10 presents a comparison of the average NDJFM SWE for 1990–2008 period against the gridded dataset from GlobSnow and the CMC SWE. SWE data on complex topography is not presented in GlobSnow due to low reliability and are masked out in Fig. 2.10. Compared to GlobSnow data, simulated SWE is underestimated over Eastern Russia, in good agreement with the DJF precipitation underestimation presented in Figure 2.9. SWE over Alaska, Yukon and the Northwest Territories in Canada also show some underestimation although the comparison with precipitation datasets showed a wet bias in the CRCM5. A second comparison was performed with the CMC SWE, showing an overestimation of SWE over most of the domain except for an underestimation over the Central Siberian Upland. The discrepancies in the snow data are another illustration of the observational uncertainties in the Arctic region leading to difficult model evaluation over the region. Nevertheless, one can see the impact of topography in the simulated SWE with maximum values located mainly over complex topography, a feature well represented in the CMC SWE compared to GlobSnow.

In general, the CRCM5 shows reasonable skill in reproducing the climatic means over the 1990–2008 period. Albeit some strong biases in winter temperatures over Eastern Siberia, temperature and precipitation can generally be considered in good agreement with the observations and within the range of observational errors. The SWE shows large differences between the observational datasets with the main differences located over regions of complex topography. The CRCM5 and the CMC SWE show detailed pattern in mountainous areas, a feature missing from the GlobSnow data.

2.5.2.2 Permafrost extent

Figure 2.11 shows CRCM5 simulated permafrost extent North of 45°N for the 1990–2008 period. Similar to the offline simulations, the shallow configuration C_Mine6 underestimates the permafrost extent with ALT below 2.0 m limited to the northernmost

latitudes of Siberia and over the Canadian Arctic Archipelago. The total near-surface permafrost cover reaches only 350,000 km^2.

The deep mineral configuration (C_Mine47) shows substantially more near-surface permafrost compared to the shallow configuration with a total coverage of 10.5 x 10^6 km^2 of continuous and discontinuous permafrost. The matching offline experiment Off_Mine47 shows larger permafrost extent (12.3 x 10^6 km^2) compared to C_Mine47 with the southern permafrost limit extending further south, mostly on the Siberian side. This reduced extent is combined with generally deeper averaged ALT over the continuous and discontinuous permafrost regions in C_Mine47 compared to Off_Mine47, 3.08 m versus 2.21 m respectively (Table 2.2). This increased ALT in CRCM5 is likely related to the winter warm biases compared to ERA-Interim (Fig. 2.8).

Compared to C_Mine47, the C_OM47 and C_OMSC47 experiments show increased permafrost extent and reduced ALTs over the continuous and discontinuous regions. Summertime changes in soil temperature resulting from the implementation of SOC (figure not shown) shows very similar response to offline simulations (Fig. 2.5) with maximum cooling near the surface. Comparison of soil temperatures and ALTs for coupled experiments with observed data are similar to those for the offline simulations and are therefore not presented here.

2.5.2.3 Surface energy balance

Offline experiments showed that the implementation of SOC changes the summer surface energy partitioning by decreasing the ground heat flux (Fig. 2.5 and 2.6). In the CRCM5, the decreased ground heat flux is compensated by increases in the surface turbulent fluxes. The surface energy partitioning between the latent and sensible heat fluxes can potentially have a large impact on the surface climate in coupled models. Two previous studies that addressed the impact of SOC on near-surface climate show conflicting results. Lawrence and Slater (2008) showed a large increase in the sensible heat flux over the latent heat flux, causing increased 2 m-air temperatures, and a deeper and dryer atmospheric

boundary layer, which decreased the low-level clouds, with SOC inclusion in the model. Rinke et al. (2008) on the other hand showed a large increase in the latent heat flux, a decrease in the 2 m-air temperature and an increase in the low-level cloud cover. The atmospheric response in coupled models is therefore very sensitive to the implementation technique and parameterization.

Figure 2.12 presents the differences in the summer (June-July-August) latent heat flux, sensible heat flux and 2-m air temperature, for the 1990–2008 period, between the C_OM47 and C_Mine47 experiments. The surface turbulent heat fluxes generally show an increase over the domain in the C_OM47 experiment. This increased energy redistribution towards the atmosphere is a direct consequence of the decreased ground heat flux (figure not shown), similar to the results presented in Fig. 2.6. The maximum increases in the latent heat flux are located in the coastal regions while the increase in the sensible heat flux are mainly located inland, mostly over Central and Eastern Siberia. Most of the regions where differences exist in both fluxes are statistically significant at a 95% confidence level. Surface air temperature changes show a general decrease over regions where the latent heat flux increases and an increase over regions where the increases in sensible heat flux dominates, in good agreement with the results from both Rinke et al. (2008) and Lawrence et al. (2008). Despite the somewhat large increases in the surface turbulent fluxes, the statistically significant temperature changes are mostly present outside of the continuous permafrost region (Fig. 2.11). As discussed in the next paragraph, the two experiments using mineral soil simulate similar surface fluxes and surface temperatures while the two experiments including SOC present strong similarities.

Figure 2.13 presents the mean 1990–2008 annual cycle of the latent heat flux (LHF) and sensible heat flux (SHF) along with the 2 m-air temperatures over two main vegetation categories present over the Arctic region; namely needleleaf trees and tundra. Besides the different vegetation parameters, another important difference is the geographic distribution of these vegetation categories (Fig. 2.13d), with the needleleaf trees present mostly in the southern part of the domain while tundra covers extensively the higher latitudes and coastal regions of the Arctic Ocean. Therefore, the two vegetation classes show different surface climates with colder temperatures over the tundra compared to the forested areas (Fig. 2.13c).

For both vegetation classes, the surface energy fluxes (Fig. 2.13) are separated in two distinct groups, with generally larger fluxes noted for the two experiments using the SOC parameterization compared to the two experiments using mineral soil. This separation is simply the result of the decreased ground heat flux in the summer for the experiments using SOC (not shown) as in the offline experiments (Fig. 2.6), therefore increasing the surface energy redistribution towards the atmosphere.

For the needleleaf tree regions, the SHF and LHF show differences in their annual cycle. The LHF (Fig. 2.13a) shows larger increases during early summer for the two SOC experiments. Differences in LHF are maximum in June, rapidly decreasing to reach similar values to the mineral experiments in August. The SHF, on the other hand, is similar between all four experiments until May. In July, the soil organic experiments show large increase in the SHF (Fig. 2.13b). Over tundra, the LHF increase is generally larger compared to the changes in the SHF in good agreement with spatial distribution of LHF differences over tundra (Fig. 2.12). The differences between the SOC and the mineral experiments are maximum in June by up to 9.4 W m^{-2} while the LHF reaches maximum values in July. The SHF increases are generally smaller, as can be noted on Fig. 2.12 limited to a maximal 6.8 W m^{-2} in June.

To understand the surface energy partitioning, one must study the availability of soil water for evaporation and transpiration. CLASS allows transpiration to occur for air temperatures above 0 °C, provided soil liquid water is available in the soil layers with roots. This explains the delay in the increase of the LHF component over grasslands compared to the forested areas, directly related to the colder surface climate. Secondly, results for offline experiments (and similarly for CRCM5) showed increased soil water content in the first soil layer in experiments using the SOC parameterization (Fig. 2.7), largely caused by the increased soil porosity. Figure 2.13d presents the soil saturation for the upper two layers for the needleleaf vegetation category. For the organic soil experiments, the soil saturation reaches maximum value in May for the first layer, rapidly decreasing to reach values near the retention capacity of the organic soils (0.27) in July and August. Therefore, water available for evapotranspiration is higher in May and June compared to July explaining the larger

increase in the LHF over that period while SHF shows the largest differences in July, when the surface soil layer is drier.

The net effect of the introduction of soil organic carbon is a drying of the first soil layer combined with an increase in the soil saturation in deeper layers, where the depth to bedrock allows more than one permeable layer (Fig. 2.1b). The downward displacement of soil water is caused by the larger hydraulic conductivity and low suction of the organic soils, a result also obtained by Lawrence and Slater (2008). Furthermore, in the organic soils parameterization, if the liquid water content of the first soil layer is above the retention capacity, CLASS redistributes the water within the layer by creating a vertical gradient, imposing the retention capacity at the soil surface and linearly increasing the liquid water content to reach saturation at the bottom of the layer (Verseghy 2008). This formulation therefore presents a relatively dry surface to the atmosphere, limiting direct evaporation from the top soil layer, explaining the combination of increased LHF and SHF.

The CRCM5 shows moderate atmospheric response to the increase in the summer surface turbulent heat fluxes (Fig. 2.13c). The summer 2 m-air temperature changes are limited to maximal values within ±2 °C over both vegetation categories. Spatially, changes in 2 m-air temperatures shows summertime cooling over North America and Eastern Russia reaching changes of –0.5 to –1.5 °C, while Western Russia warms between 0.5 and 1 °C. These results are not statistically significant and therefore cannot be associated with the implementation of SOC with certainty. No clear signal is visible for the changes in the atmospheric boundary layer height or for the low-level cloud cover (not shown). The limited changes to the near-surface temperatures to the increase in the surface turbulent fluxes is likely explainable by the similar magnitude of the changes to both turbulent fluxes. Both fluxes increase in similar proportion, leading to very little changes in the Bowen ratio (SHF/LHF) therefore having a limited impact on the atmospheric boundary layer stability.

In summary, CRCM5 results show a more moderate response of the surface climate to the implementation of SOC compared to the studies of Lawrence and Slater (2008) and Rinke et al. (2008). Increases in LHF and SHF are related to the availability of water in the near-surface layers explaining the seasonality of the increases in the surface turbulent fluxes,

especially over the forested areas. The limited influence of the SOC implementation on the surface climate is likely caused by the similar increases in both fluxes, having little impact on the boundary layer stability, illustrating the atmospheric model sensitivity to the implementation of SOC.

2.5.2.4 Sensitivity of simulated ALT to atmospheric parameters

In this section, we evaluate the simulated ALT trends for the 1960–2008 period and its sensitivity to atmospheric variables. Figure 2.14 presents the ALT trends for the three simulations using the deep soil configuration, for those points that retain near-surface permafrost until the end of 2008. The experiment using mineral soils, C_Mine47, has the largest trend values over most of the domain, compared to C_OM47 and C_OMSC47. One might note large areas near the southern limit of the permafrost region showing signs of degradation over the simulation period, as shown in grey in Fig. 2.14. The extent of this area is larger in C_Mine47 compared to the experiments using SOC. For grid points where the ALT trend is statistically significant at 90% confidence level, the average ALT trend in C_Mine47 is 12.3 cm/decade, a larger value compared to the ~8 cm/decade obtained by Oelke et al. (2004). Maximum values are mainly located over Northwest and Eastern Siberia, regions where the average ALT is overestimated compared to Oelke et al. (2004) and Burke et al. (2013). The experiment C_OM47 shows smaller trends in ALT amongst all experiments, 6.7 cm/decade, likely a consequence of the colder winter soil temperatures and the effective insulation of the SOC in summer. Nevertheless, the trend is statistically significant over most of the continuous and discontinuous permafrost regions except for Central Siberia, where all experiments show non-significant trends that are in good agreement with other modeling studies (Oelke et al. 2004; Burke et al. 2013). The C_OMSC47 experiment shows significant trends over most of the domain, with maximum trends located in Southern and Eastern Siberia and over North America from Alaska to the Hudson Bay with an average trend of 9.9 cm/decade over grid points where the ALT trend is significant at 90% confidence level.

To understand the sensitivity of the ALT to atmospheric variables, an analysis of the relation between ALT and atmospheric variables directly influencing the soil thermal regime

was performed over grid points showing significant ATL trends. To identify the most important atmospheric variables having an impact on the ALT, trend analysis and correlation between atmospheric parameters and ALT were investigated. Statistically significant correlations at 95% confidence level are found between the ALT and the following atmospheric parameters: 2 m-air temperatures (T2M), the degree-day thawing (DDT) and freezing (DDF) indexes and the length of both thawing and freezing season. The degree-day thawing (freezing) index is defined as the sum of the above-zero (sub-zero) daily average 2 m-air temperatures from October to September. Other parameters, such as SWE, net shortwave radiation at the surface, annual and seasonal precipitations show no significant correlation with the ALT.

Figure 2.15 shows the relation between the ALT anomaly and selected atmospheric parameters T2M, DDT and DDF. For the 1960–2008 period, the average annual 2 m-air temperature warms by 0.34, 0.29 and 0.27 °C/decade for experiments C_Mine47, C_OM47 and C_OMSC47 respectively. The differences in the magnitude of the trends between the experiments are due to the different spatial distribution of the grid points where the ALT trends are significant (Fig. 2.13b). This increase in temperature is significantly correlated with increases in the ALTs (Fig. 2.15) with values of 0.68, 0.85 and 0.80 for C_Mine47, C_OM47 and C_OMSC47 respectively.

Since the ALT – defined as the annual maximal thaw depth – occurs mostly at the end of the summer, the thawing index should be a better indicator than the annual average 2 m-air temperatures. The DDT shows an increase over the simulated period with values of 28.8, 30.1 and 24.2 °C day/decade for C_Mine47, C_OM47 and C_OMSC47 respectively, coherent with a warming of the surface climate over the Arctic. The ALT and the DDT in C_Mine47 experiment shows the highest correlation amongst the three experiments (0.91). The other simulations using SOC are also highly correlated with the DDT but with smaller values: 0.81 and 0.79 for C_OM47 and C_OMSC47, respectively.

The DDF shows the largest trends of all parameters considered with values of -97.2, -76.1 and -68.1 °C day/decade. The DDF and the ALT are negatively correlated, significant at

95% confidence level, with values of -0.44, -0.74 and -0.64 for C_Mine47, C_OM47 and C_OMSC47 respectively.

Although all experiments agree on the relations between a deepening of the ALT with the warming of the surface climate during the 1960–2008 period, some differences are visible, related to the soil configuration. Firstly, the mineral soil experiment, C_Mine47 shows maximal correlation of ALT with the DDT index amongst the experiments, while minimal correlations are found with T2M and DDF for that particular experiment. This shows that the mineral configuration is most sensitive to the summer temperatures. According to the larger ground heat flux in the mineral experiment compared to the SOC experiments (Fig. 2.6), results presented in this section suggest a short-term sensitivity (or "memory") of the soil to the air temperature anomalies of the same year summer with limited sensitivity to the previous winter or summer temperatures. On the other hand, the SOC experiment C_OM47 shows higher correlation with the annual temperatures, showing larger sensitivity of this particular experiment to both the summer and winter temperatures. This is partly due to the isolative effect of the SOC reducing the impact of summer temperatures while the larger snow conductivity, compared to C_OMSC47, shows relatively important impact of the winter air temperature on the soil column temperature. One might note that the high correlations between the temperature-based atmospheric parameters and the ALT on a yearly basis shows similarities to the observational study of Frauenfeld and Zhang (2011) over Russian stations, where antecedent conditions from the previous year do not appear to play a major role in affecting the subsequent near-surface soil conditions.

Results from the CRCM5 experiments showed overestimated ALT and trends over most of the Pan-Arctic domain compared to observations (CALM) and other numerical experiments using LSM (Oelke et al. 2004; Burke et al. 2013). Two hypotheses are formulated to explain the overestimated ALT and its trends: (1) the warm bias in the CRCM5 and (2) an accelerated warming in the CRCM5 surface climate compared to observations. Figure 2.16 compares the time series the DDF (Fig 2.16a) and DDT (Fig. 2.16b) indexes from UDel, CRU3.1 to simulated results for the grid points where the three deep soil configuration experiments shows significant trends in the ALT, i.e., mostly over Eastern Siberia and Alaska (Fig. 2.14). Due to the limited observations of daily temperatures in the

Arctic, estimates of the DDF and DDT indexes were computed from the monthly temperatures from UDel and CRU3.1. This method is known to introduce some uncertainties in the estimates of the indexes between 10–15% over the continuous and discontinuous permafrost regions (Frauenfeld et al. 2007). Compared to CRU3.1 data, the simulated DDF is underestimated while in relatively good agreement with the UDel data. Simulated DDT is overestimated compared to CRU3.1 while underestimated compared to UDel. In general, the CRCM5 results are between CRU3.1 and UDel estimates, showing that CRCM5 is within the observational uncertainties but tends to be warm biased, in good agreement with the simulated warm biases noted over Eastern Siberia and North America (Fig. 2.8). Statistically significant differences at 95% confidence level exist between the simulated and observational estimates, which highlight the CRCM5 warm bias over the region, especially when compared to CRU3.1, noted to be colder than UDel especially over Eastern Siberia (Fig. 2.8).

Standardizing the time series of DDF (Fig. 2.16c) and DDT (Fig. 2.16d) with respect to their long-term mean and standard deviation, removing any biases, allows estimating and comparing the trends. Standardized trends and interannual variability for DDF and DDT are almost identical for CRU3.1 and UDel. The CRCM5 experiments tend to overestimate both trends and the inter-annual variability of the indices. A t-test was performed over the standardized data that showed that the observed and simulated distributions are not significantly different at 95% confidence level. Therefore we can conclude that the warming trends are well reproduced by the CRCM5 although the warming is slightly accelerated in the model.

In summary, the simulated ALTs in CRCM5 experiments are overestimated compared to observations and other studies using offline LSMs and significantly correlated to surface air temperatures and indexes. The snow and precipitation show little correlation with ALTs and likely play a secondary role in the evolution of the soil temperatures. Despite the warm bias noted in the CRCM5 surface air temperatures, the warming trends over the 1960-2008 period is not significantly different from the observations suggesting that the overestimated ALTs are likely related to that warm bias.

2.6. Summary and conclusions

The warming observed in the Arctic in the recent decades and the warming suggested by coupled general circulation models for the 21st Century could have an important impact on the thermal state of the Arctic soils. Although direct observations are invaluable sources for monitoring the Arctic Climate, the limitations in the available data both spatially and in time strongly supports the modeling approach in order to get continuous data for large-scale studies of the Arctic. Despite an increasing number of studies addressing the changes in the thermal state of the Arctic permafrost, the land surface models used generally require improvements to their numerical formulation to adequately represent the soil organic carbon and its thermal and hydrological properties. Moreover, a limited number of studies actually focus on the land-atmosphere interactions resulting from the implementation of SOC and its potential feedbacks on the surface climate.

The first objective of this study was to assess the sensitivity of simulated Arctic soil temperature and moisture regimes, particularly near-surface permafrost and ALT, to soil layer configuration and soil organic carbon, using offline simulations with CLASS. In agreement with the work of Smerdon and Stieglitz (2006), the shallow soil configuration showed overestimated annual cycle of soil temperatures, directly affecting the permafrost extent in the Arctic. Analysis showed that such shallow configuration is not capable of reproducing high-latitude near-surface permafrost. Other modeling groups showed better permafrost extent using shallow (~3.5 m) configuration, e.g. Lawrence et al. (2008) and Dankers et al. (2011), using the Community Land Model (CLM) and the Joint UK Land Environment Simulator (JULES), respectively. Though the above studies had similar soil layers to that of the shallow configuration considered here, there were important differences with respect to the depth to bedrock. In this study, depth to bedrock is based on the dataset from Webb et al. (2000), while Dankers et al. (2011) and Lawrence et al. (2008) assumed permeable soil composed of sand, silt, clay and organic material for the entire soil column. Since a large part of the study domain has less than 1 m of permeable soil according to Webb et al. (2000), the thermal conductivity is larger in our experiments due to the presence of shallow bedrock and reduced thermal inertia due to the limited soil water content and phase

changes in the soil column. The combination of these effects leads to bigger thaw depths compared to a fully permeable soil column.

Deepening the soil column depth to 65 m improved the permafrost extent although the Active Layer Thickness (ALT) was overestimated compared to observations and other modeling studies (Oelke et al. 2003; Oelke et al. 2004; Lawrence et al. 2008; Dankers et al. 2011; Burke et al. 2013). The implementation of SOC greatly reduced the ALT and summer soil temperatures over the Pan-Arctic domain compared to the experiment using mineral soils. Combination of the SOC and the decreased snow thermal conductivity of Sturm et al. (1997) resulted in colder temperatures during the summer due to the SOC and warmer temperatures in winter because of the reduced heat flux from the soil towards the atmosphere through the snow pack. The land surface model CLASS therefore showed a large sensitivity of the soil temperatures to the snow density-snow thermal conductivity relation that should be investigated further.

The hydrological response to the SOC implementation revealed complex interactions between the surface runoff and drainage to the permeable soil depth, presence of deep peatlands and the soil temperatures. In general, simulation with cooler temperatures, near-surface permafrost and shallower ALTs showed increased (decreased) surface runoff (drainage), particularly over deep peatlands.

CRCM5 experiments showed similar sensitivities to soil column depth and SOC implementation as the offline CLASS experiments. Simulated near-surface permafrost extent showed similar response although the CRCM5 deep mineral configuration showed reduced extent and larger ALT values compared to its offline counterpart due to warm biases in CRCM5 climatology. As for offline experiments, important decreases in simulated ALTs result from the implementation of SOC.

The summer surface turbulent fluxes in CRCM5 shows important increases caused by the SOC implementation, as a direct response to the decreased ground heat flux. While Lawrence and Slater (2008) and Rinke et al. (2008) obtained opposite and significant signals in the surface turbulent heat fluxes, results from this study show moderate response with very limited impact on the surface climate and atmospheric boundary layer. This is mainly caused

by the similar increases in both sensible and latent heat fluxes in the SOC experiments mainly controlled by the availability of near-surface soil moisture and saturation level. Only limited regions of the Pan-Arctic domain show significant changes to the 2 m-air temperature, boundary layer height and low-level cloud cover. These results emphasized the large sensitivity of atmospheric models to SOC formulation.

The warming of the near-surface climate over the 1960–2008 period is responsible for the positive and significant trends in the simulated ALT, present over most of the Pan-Arctic domain for all CRCM5 experiments. The mineral soil experiment showed the largest trends and permafrost degradation amongst the experiments. The large sensitivity of that particular experiment to the increasing degree-day thawing (DDT) index suggests that changes in the summer temperatures dominate the ALT sensitivity. Although the experiments using SOC were also significantly correlated with the DDT index, the correlations between ALT and DDT departures from their mean values showed smaller values while increased correlation were found for the annually averaged 2 m-air temperature and the degree-day thawing index. The higher correlation with annual and winter parameters shows that the SOC experiments are relatively less sensitive to summer temperatures while increasing winter temperatures play a more important role in the ALT trends for these experiments.

Analysis of the trends in DDT and DDF showed that the CRCM5 surface climate trends are not significantly different from that of CRU3.1 and UDel. The overestimated ALTs and trends in the model are likely linked to the near-surface warm biases in the model and would require further investigation to improve their representation.

Based on the present study, it appears important to further improve the representation of snow in CLASS, given the winter cold biases associated with soil temperatures for both offline and coupled experiments. For example, Burke et al. (2013) showed that a more realistic multi-layer snow scheme significantly reduced the winter cold bias in soil temperatures previously observed in JULES land surface model (Dankers et al. 2011).

Other processes not presently included in CLASS such as ice-lenses and thermokarst lakes may also have important impact in the ALT simulation and trends in the model. In the event that detailed Pan-Arctic observations of the soil organic content and its spatial coverage

becomes available, a sensible next step in future work would be to use sub-grid scale variability of the soil type using the "mosaic option" that is available in CLASS. The main challenge would be the colossal amount of work required to gather and centralize the terrain data.

Table 2.1: List of experiments performed in this study

	Experiment mode	Atmospheric Forcing	Period	Soil column depth	SOC	Snow conductivity
Off_Mine6	Offline	ERA-40 & ERA-Interim	1957-2008	3.5 m	No	Mellor (1977)
Off_Mine47	Offline	ERA-40 & ERA-Interim	1957-2008	65 m	No	Mellor (1977)
Off_OM47	Offline	ERA-40 & ERA-Interim	1957-2008	65 m	**Yes**	Mellor (1977)
Off_OMSC47	Offline	ERA-40 & ERA-Interim	1957-2008	65 m	**Yes**	**Sturm et al. (1997)**
C_Mine6	Coupled	—	1957-2008	3.5 m	No	Mellor (1977)
C_Mine47	Coupled	—	1957-2008	65 m	No	Mellor (1977)
C_OM47	Coupled	—	1957-2008	65 m	**Yes**	Mellor (1977)
C_OMSC47	Coupled	—	1957-2008	65 m	**Yes**	**Sturm et al. (1997)**

Table 2.2: Permafrost extent (x10^6 km^2) located North of 45°N and averaged Active Layer thickness (m) over 1990–2008 period

	Discontinuous		Continuous		Continuous+Discontinuous	
	Area (x10^6 km^2)	ALT (m)	Area (x10^6 km^2)	ALT (m)	Area (x10^6 km^2)	ALT (m)
IPA	**3.14**	-----	**10.12**	-----	**13.25**	-----
Off_Mine6	**0.09**	0.0001	**1.18**	0.5869	**1.27**	0.55
Off_Mine47	**2.47**	2.82	**9.79**	2.06	**12.27**	2.21
Off_OM47	**2.71**	2.18	**9.89**	1.56	**12.60**	1.69
Off_OMSC47	**2.10**	2.74	**9.37**	2.03	**11.47**	2.16
C_Mine6	**0.03**	1.21	**0.33**	0.27	**0.35**	0.33
C_Mine47	**1.69**	3.34	**8.81**	3.024	**10.50**	3.08
C_OM47	**2.622**	2.23	**9.53**	1.45	**12.15**	1.62
C_OMSC47	**2.02**	2.78	**9.30**	1.91	**11.32**	2.10

Table 2.3: Annual mean soil temperature biases (°C) relative to longitudinal position of the stations.

		35-190°E		35-100°E		100-190°E		60-90°E	
Depth	**Experiment**	**Bias**	**RMSE**	**Bias**	**RMSE**	**Bias**	**RMSE**	**Bias**	**RMSE**
0.2 m	Off_Mine6	-5.80	7.18	-3.38	3.91	-10.02	10.72	-3.45	3.89
	Off_Mine47	-5.95	7.37	-3.49	4.02	-10.25	11.00	-3.60	4.04
	Off_OM47	-6.54	7.73	-4.36	4.79	-10.33	11.14	-4.66	4.94
	Off_OMSC47	-4.40	5.59	-2.80	3.16	-7.20	8.26	-2.79	3.06
0.85 m	Off_Mine6	-5.65	6.99	-3.30	3.87	-9.93	10.52	-3.37	3.84
	Off_Mine47	-5.87	7.23	-3.48	4.03	-10.21	10.85	-3.60	4.07
	Off_OM47	-6.43	7.56	-4.30	4.75	-10.30	10.96	-4.64	4.96
	Off_OMSC47	-4.36	5.45	-2.76	3.16	-7.27	8.11	-2.80	3.13
2.75 m	Off_Mine6	-5.60	6.92	-3.24	3.80	-9.81	10.37	-3.16	3.58
	Off_Mine47	-5.91	7.18	-3.57	4.08	-10.10	10.68	-3.55	3.94
	Off_OM47	-6.34	7.41	-4.26	4.67	-10.04	10.68	-4.43	4.67
	Off_OMSC47	-4.46	5.46	-2.90	3.26	-7.23	8.00	-2.82	3.07

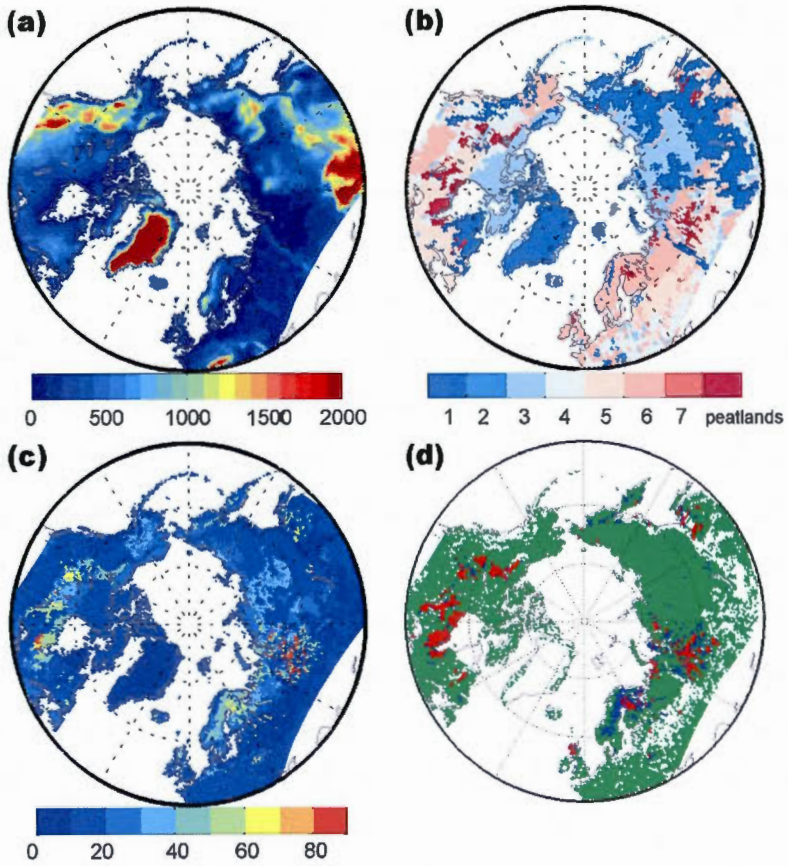

Figure 2.1: (a) CRCM topography (m); (b) Number of permeable layers. Dark red regions represent deep peatlands where Letts et al. (2000) parameterization is used. (c) Soil organic concentration (kg m^{-2}) from IGBP-DIS for the first 100 cm of soil. (d) Number of soil organic layers considered in Off_OM47, Off_OMSC47, C_OM47 and C_OMSC47. Red regions are similar to those in (b), while green (blue) regions represent grid points where 10 cm (30 cm) of organic soil are used.

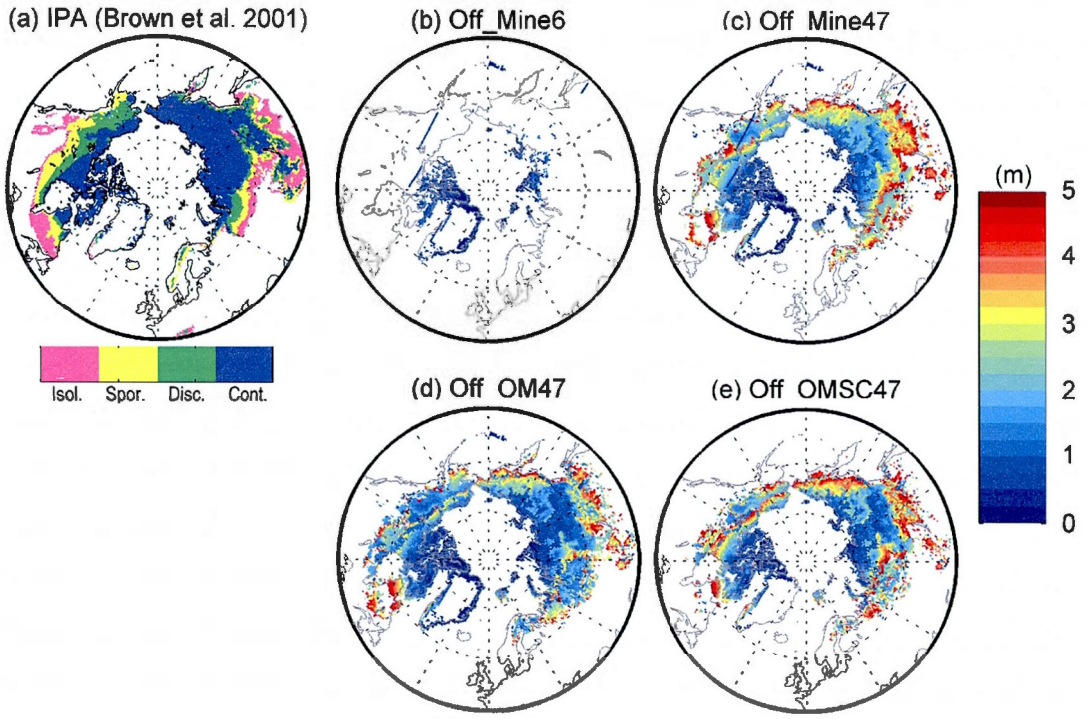

Figure 2.2: (a) Observed permafrost extent (continuous, discontinuous, sporadic and isolated) from the International Permafrost Association (IPA) (Brown et al. 1998); (b)-(e) Modeled average permafrost extent and ALTs for the offline simulations for the 1990–2008 period.

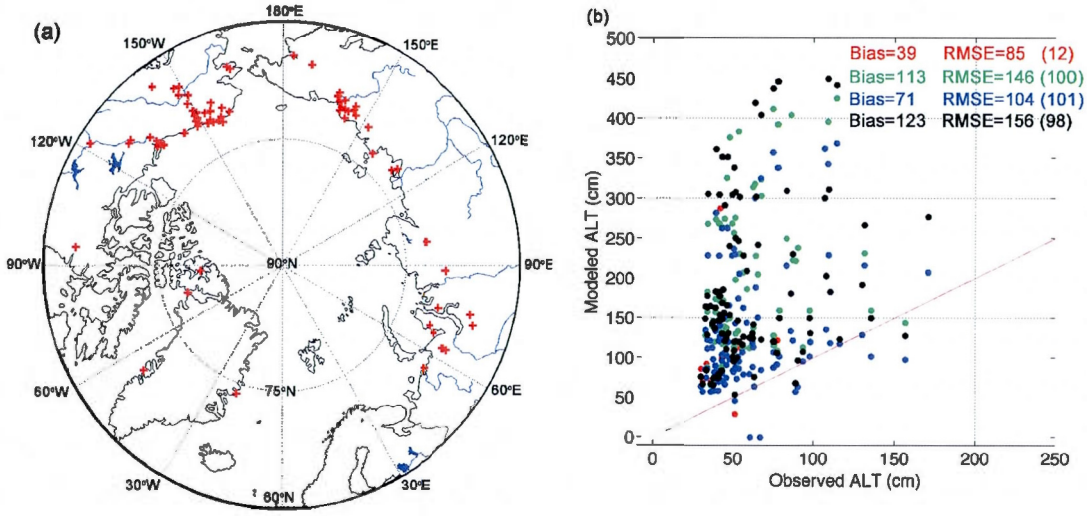

Figure 2.3: (a) Location of selected CALM sites used in the evaluation of ALTs (red). (b) Averaged 1990–2008 observed vs. modeled annual maximum ALTs for CLASS offline simulations: Off_Mine6 (red); Off_Mine47 (green); Off_OM47 (blue); Off_OMSC47 (black). For all experiments, the number in brackets indicates the number of stations used for comparison.

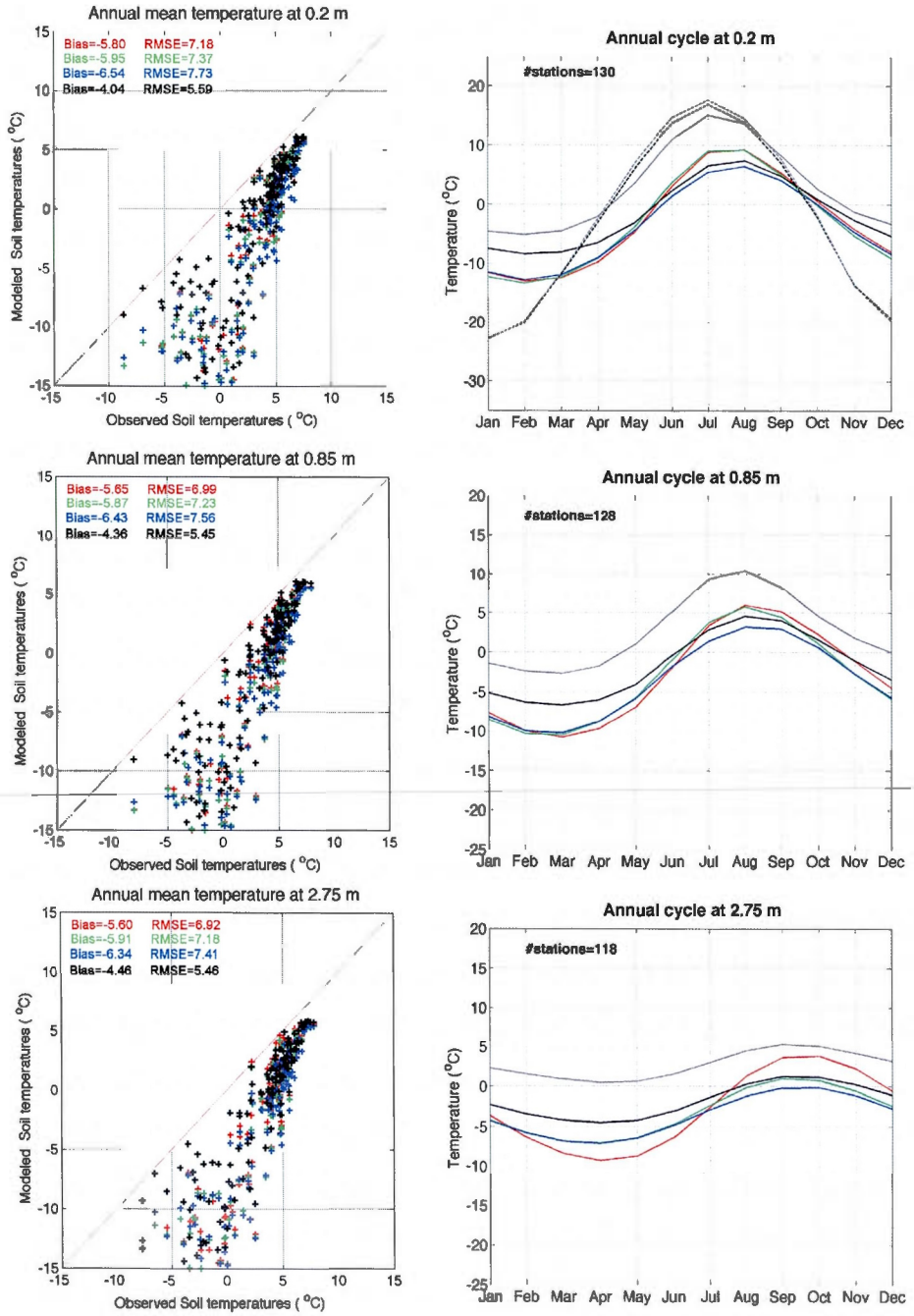

Figure 2.4: (left) Simulated and observed mean annual soil temperatures (°C) for stations within the region bounded by 20-190°E and 55-90°N. (right) Mean annual cycle of observed (grey) and simulated soil temperature: Off_Mine6 (red); Off_Mine47 (green); Off_OM47 (blue) and Off_OMSC47 (black). Dashed line on top right plot represents 2 m-air temperature for UDel (grey) and that from ERA-Interim (black) used to drive CLASS offline.

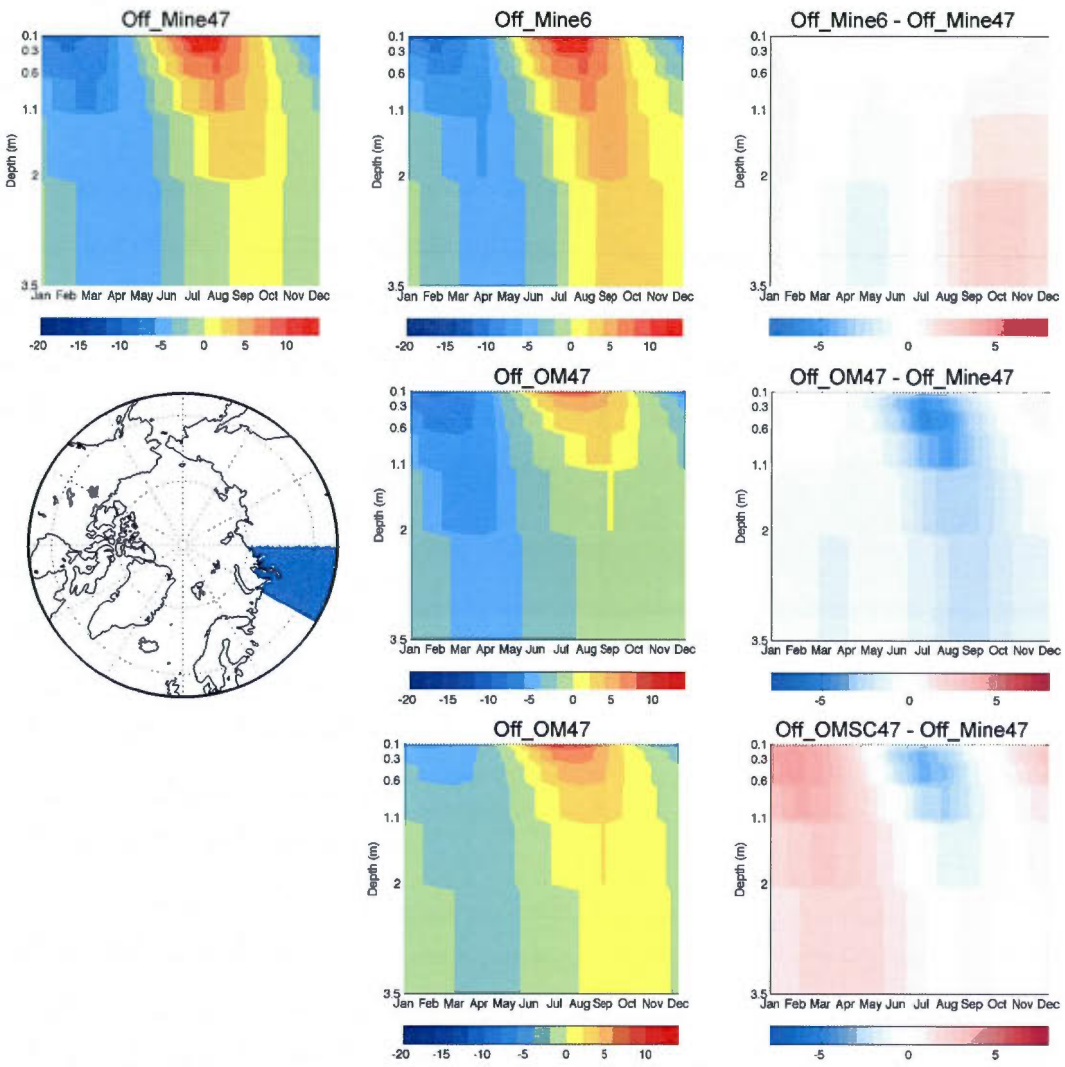

Figure 2.5: Averaged mean monthly soil temperature (°C) for the 1990–2008 period for Northwest Siberia (55-90°N, 60-90°E; blue shaded region in the left central panel), for various CLASS offline simulations and differences relative to the deep mineral configuration (Off_Mine47). No vertical interpolation of the temperature is done therefore results are presented on model levels.

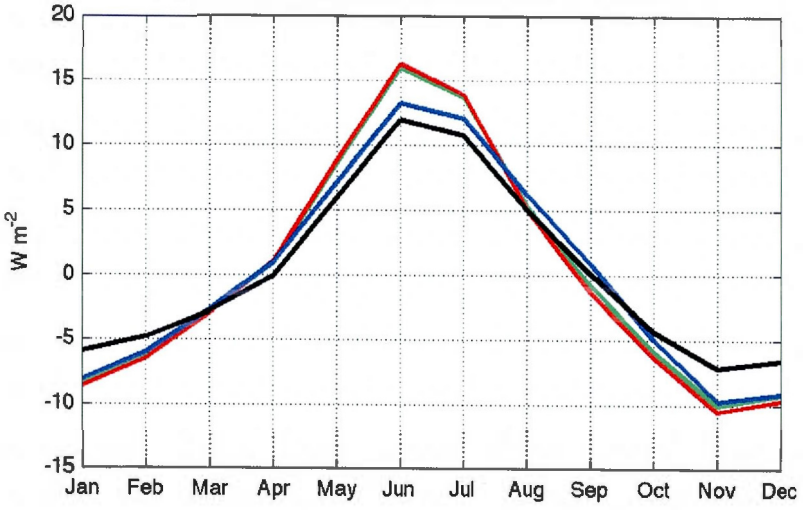

Figure 2.6: Monthly averages of ground heat flux at the soil/snow (atmosphere) interface for Northwestern Siberia (60-90°E, 55-75°N) for the 1990−2008 period for: Off_Mine6 (red), Off_Mine47 (green), Off_OM47 (blue) and Off_OMSC47 (black).

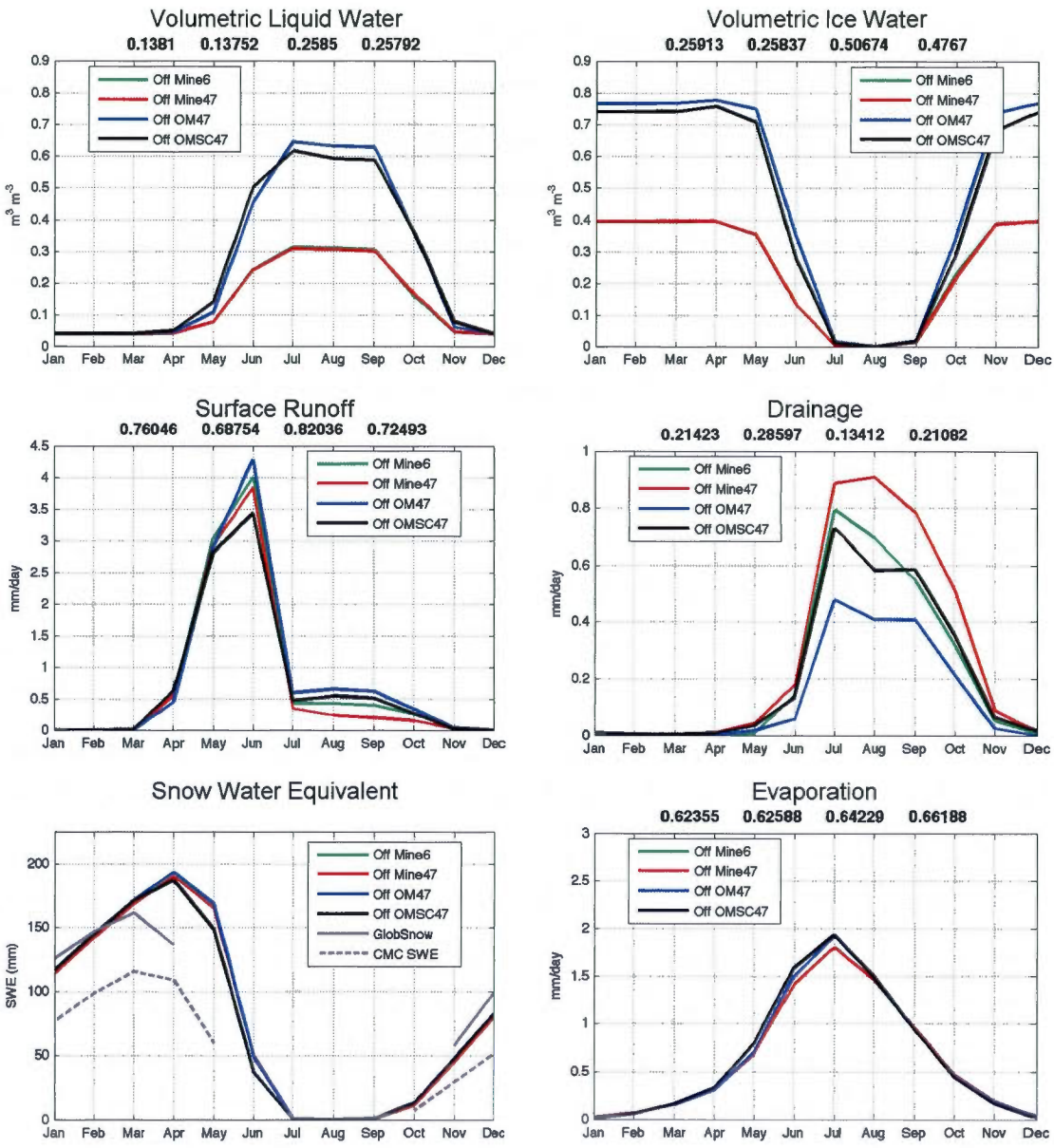

Figure 2.7: Annual cycle of (a) liquid water content and (b) frozen water content for the first soil layer, (c) surface runoff, (d) sub-surface runoff, (e) SWE and (f) evaporation, over Northwestern Siberia (60−90°E, 55−75°N) computed over the 1990−2008 period for CLASS offline simulations: Off_Mine6 (red), Off_Mine47 (green), Off_OM47 (blue) and Off_OMSC47 (black). Numbers on top of the subpanels represent the annual average values for Off_Mine6, Off_Mine47, Off_OM47 and Off_OMSC47 in order. Grey lines snow observational data of SWE for GlobSnow (full line) and CMC SWE (dashed).

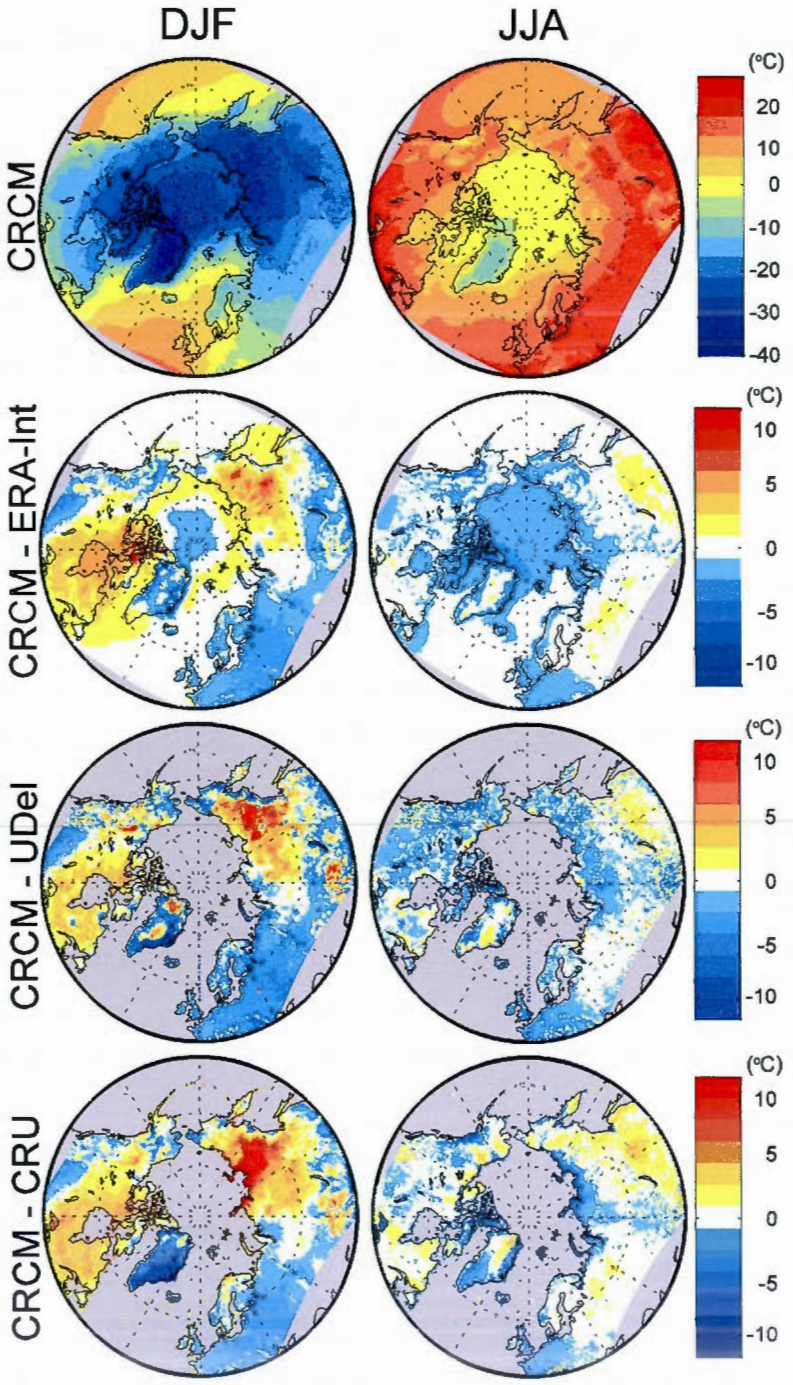

Figure 2.8: Comparison of averaged 2 m-air temperature (°C) for DJF (left) and JJA (right) for C_Mine47 (1st row) and differences with ERA-Interim (2nd row), UDel dataset (3rd row) and CRU TS3.1 dataset (4th row), for the 1990−2008 period.

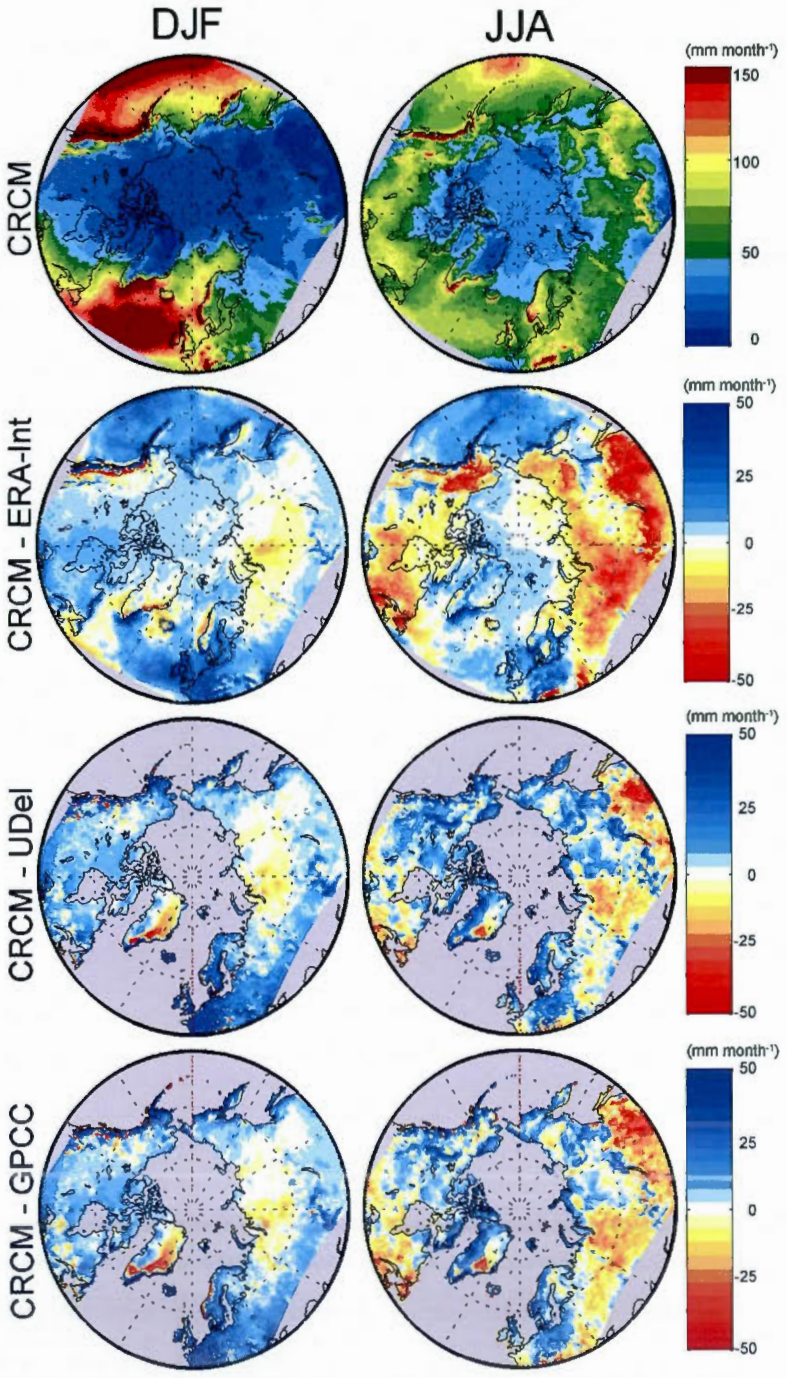

Figure 2.9: Comparison of averaged precipitation (mm month^{-1}) for DJF (left) and JJA (right) for C_Mine47 (1st row) and differences with ERA-Interim (2nd row), UDel dataset (3rd row) and GPCC dataset (4th row), for the 1990−2008 period.

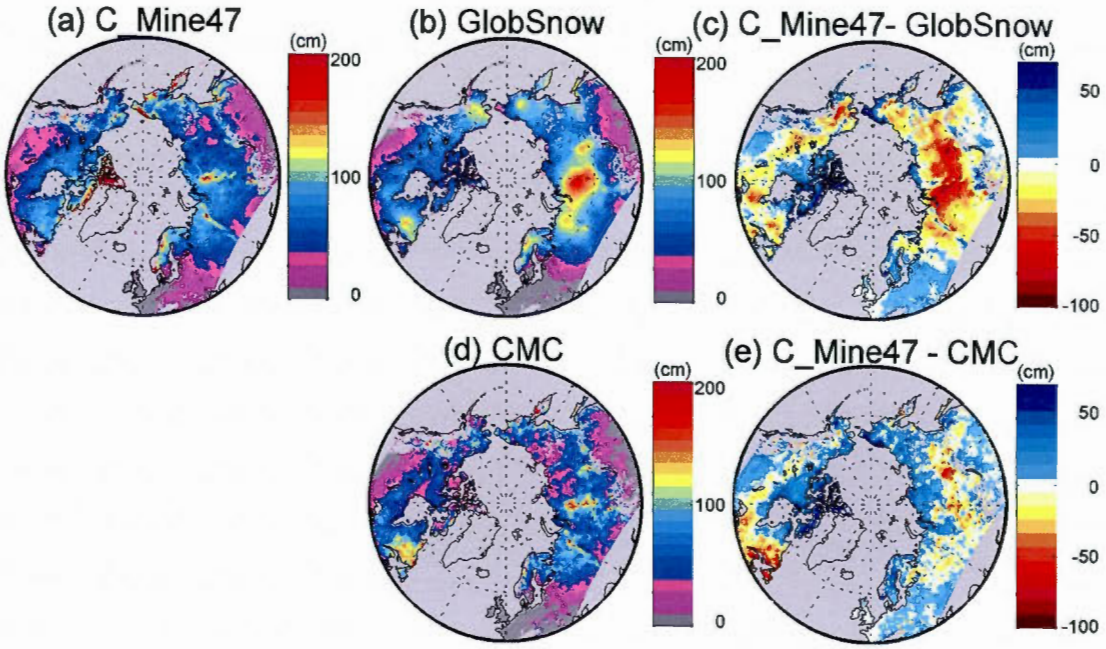

Figure 2.10: Comparison of average SWE (cm) for NDJFM for: (a) C_Mine47, (b) GlobSnow, (c) the difference C_Mine47-GlobSnow, (d) CMC SWE analysis, (e) the difference C_Mine47-CMC. Mountainous areas are masked in GlobSnow dataset due to insufficient data and high uncertainties; therefore no comparison is made with modeled snow mass over these areas.

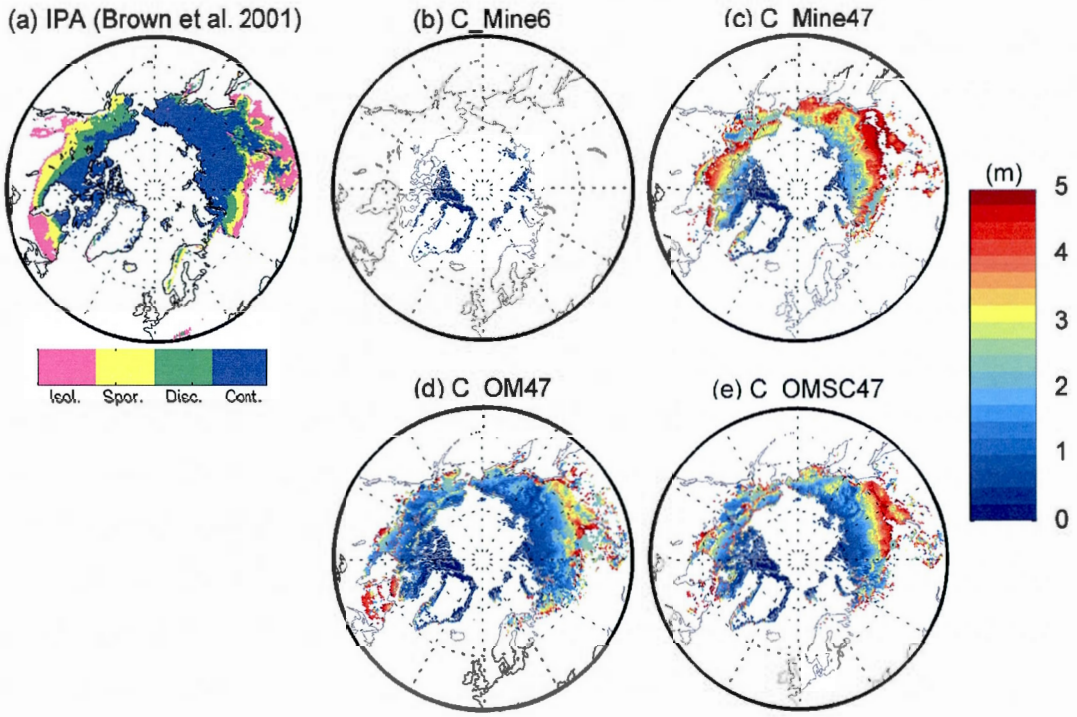

Figure 2.11: (a) Observed permafrost extent (continuous, discontinuous, sporadic and isolated) from the International Permafrost Association (IPA) (Brown et al. 1998); (b)-(e) Modelled permafrost extent and ALTs for the CRCM5 simulations for the 1990-2008 period.

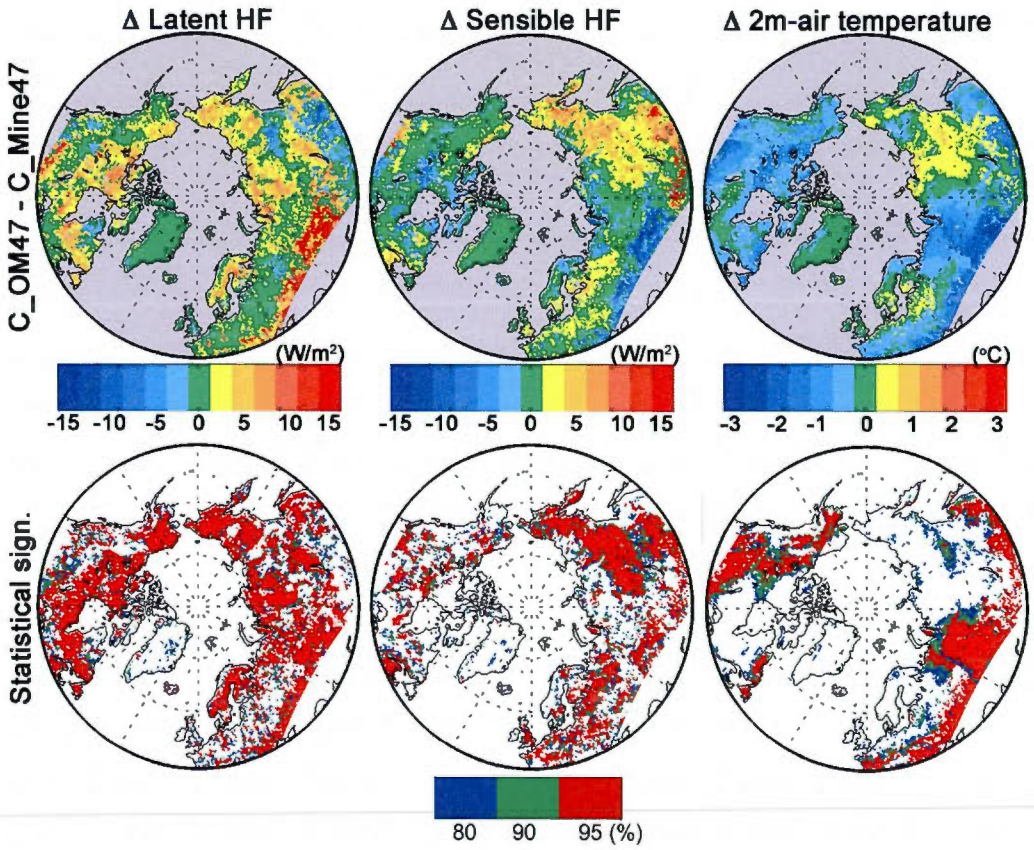

Figure 2.12: (top) Comparison of summer (June-July-August) climatology of (left) latent heat flux, (middle) sensible heat flux and (right) 2 m-air temperature between C_OM47 and C_Mine47 over the 1990–2008 period. (bottom) Statistical significance of the differences using a t-test.

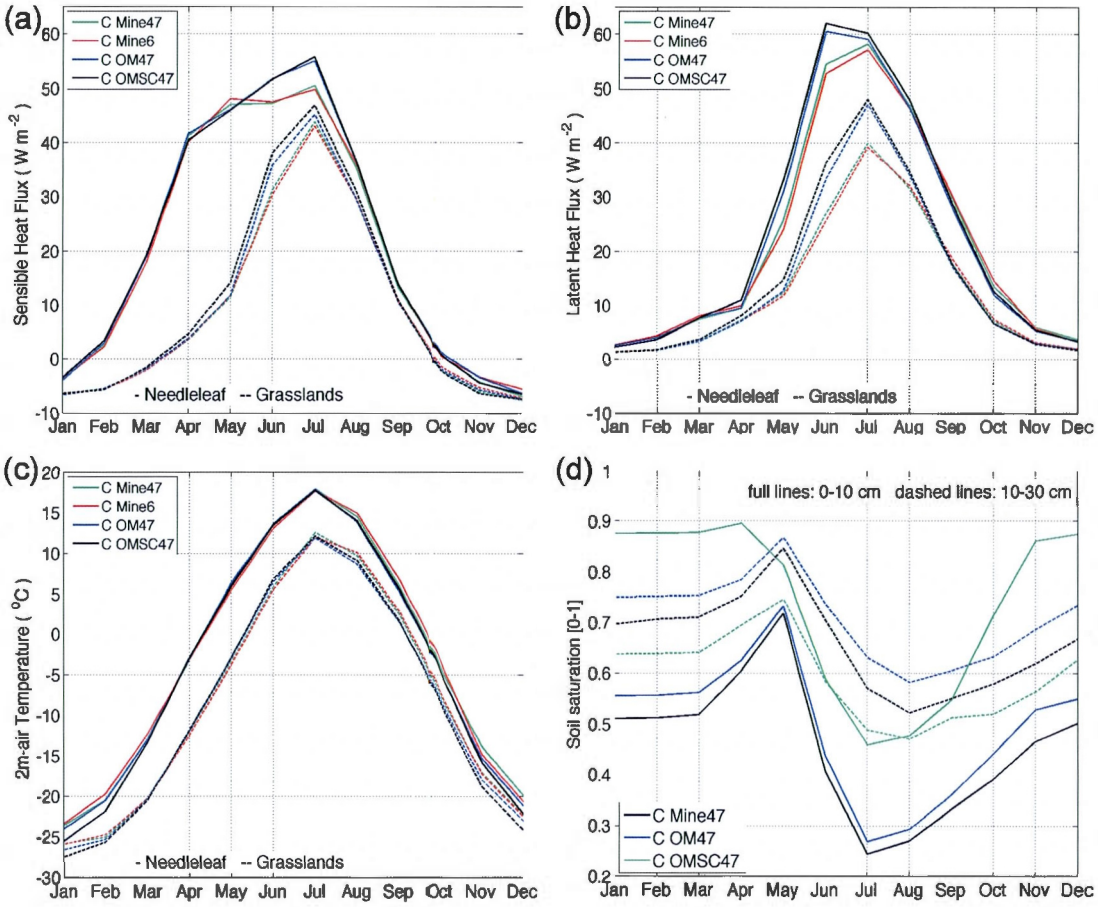

Figure 2.13: Average annual cycle of (a) latent heat flux, (b) sensible heat flux (Wm^{-2}) and (c) 2 m-air temperature (°C) for needle leaf trees (full lines) and grasslands (dashed lines) between 55-75°N and 45-270°E for the 1990–2008 period for simulations Off_Mine6 (red), Off_Mine47 (green), Off_OM47 (blue) and Off_OMSC47 (black). (d) Annual cycle of soil saturation for the first two soil layers: 0-10 cm (full lines) 10-30 cm (dashed lines) for needle leaf trees. Identical color codes are used to designate experiments.

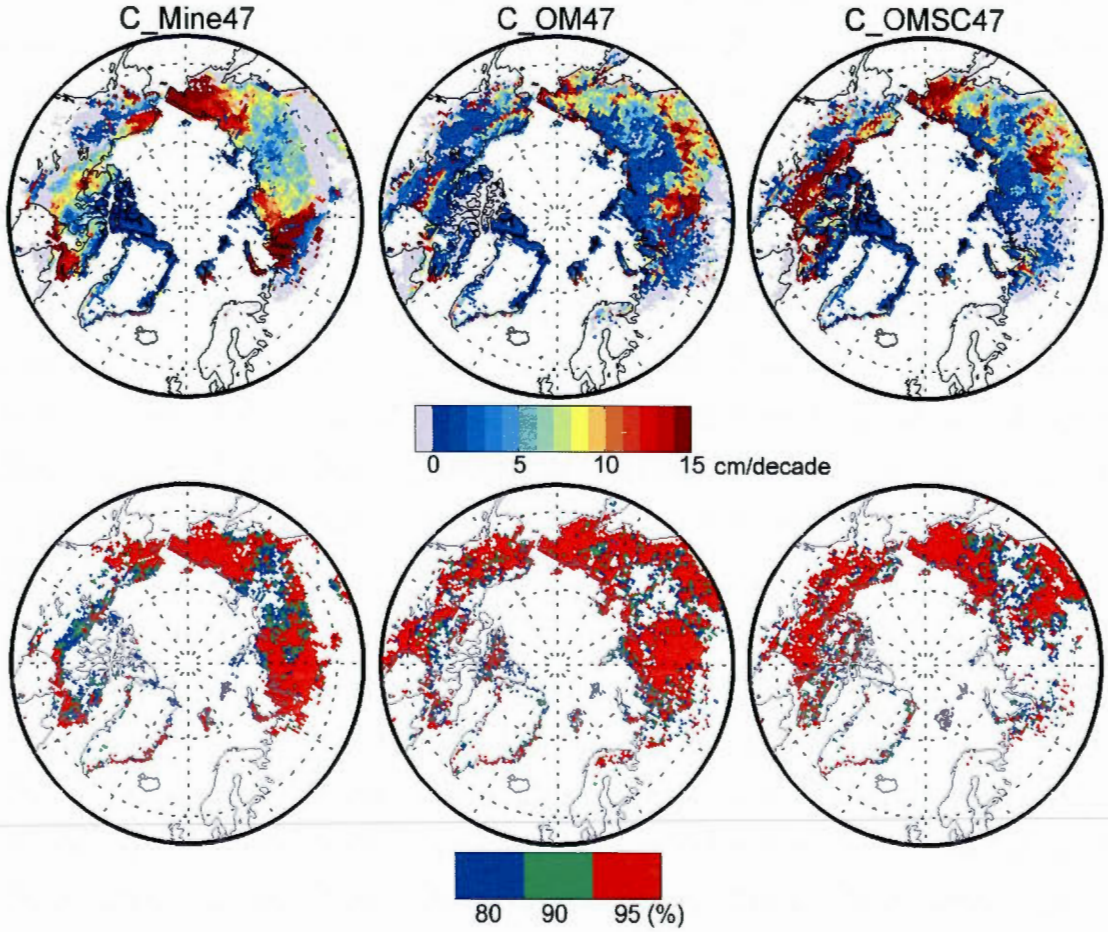

Figure 2.14: (top) Trends in ALT for the 1960–2008 period for C_Mine47 (left), C_OM47 (middle) and C_OMSC47 (right). Grey regions represent grid cells where permafrost is not present for the entire simulation period. (bottom) Statistical significance of the trends defined using the Mann-Kendall test.

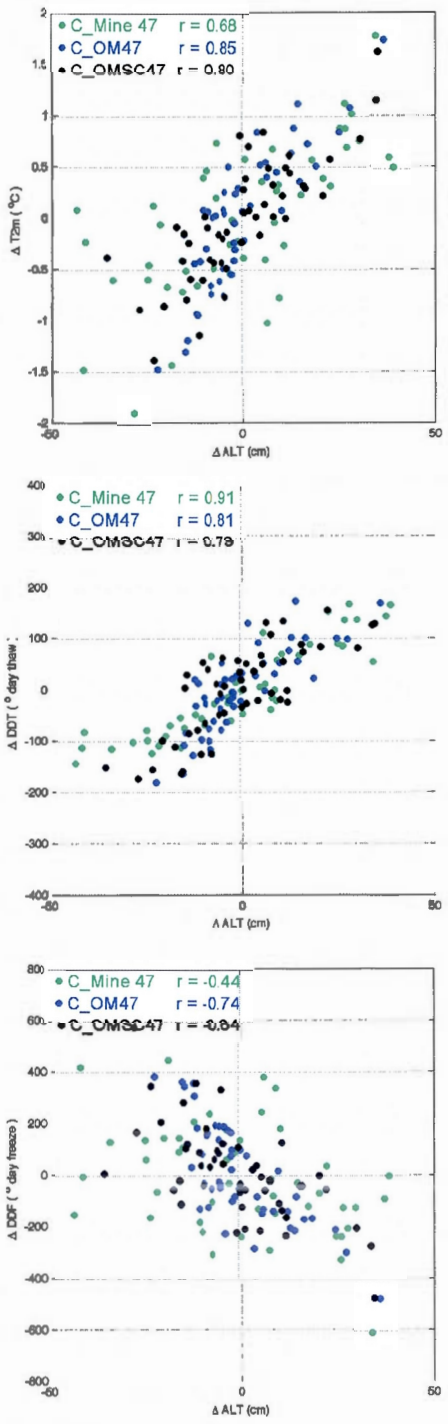

Figure 2.15: Relation between ALT departure and average annual 2 m-air temperature (top), degree-day thawing index (middle) and degree-day freezing index (bottom) for experiments: C_Mine47 (green), C_OM47 (blue) and C_OMSC47 (black) over the respective regions where ALT trends are significant at a 90% confidence level.

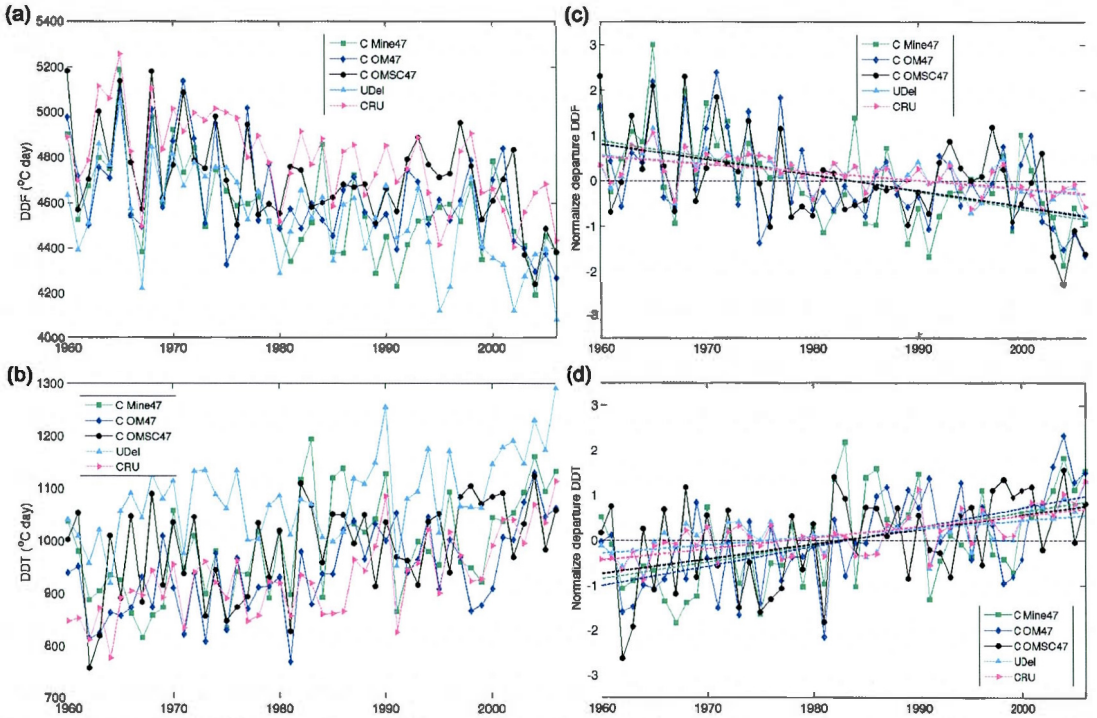

Figure 2.16: (left) Time series of degree-day freeze (a) and degree-day thaw (b) over grid points where all experiments shows statistically significant ALT trends at 90% confidence level. Experiments C_Mine47 (green), C_OM47 (blue), C_OMSC47 (black) and observations from UDel (cyan) and CRU (magenta) are presented. Normalized time series and statistically significant linear trends are presented for DDF (c) and DDT (d).

CONCLUSION

The overall objective of this thesis was to understand the large-scale control mechanisms for the arctic sea ice and near-surface permafrost using numerical models. The important results from this study are summarized here before providing thoughts on future scientific questions that need to be addressed. In the first chapter of this thesis, the goal was to understand the physical mechanisms leading to Rapid Ice Loss Events (RILEs) simulated by the the Rossby Centre Atmosphere-Ocean (RCAO) regional climate model. It was found that two major mechanisms were responsible for the occurrence of RILEs. The long-term thinning of the sea ice cover made the sea ice more vulnerable. The timing of the RILEs were determined by anomalies in the large-scale atmospheric and oceanic circulations, leading to enhanced heat transport mostly from the Nordic Seas towards the Atlantic Sector of the Arctic Ocean, melting the thin ice present over the area, resulting in abrupt reduction in the September sea ice cover. Over the Pacific Sector of the Arctic Ocean, anomalous sea ice motion from the coast of Alaska towards the centre of the Beaufort Sea triggered a sea ice-albedo feedback by increasing the absorbed solar radiation and increasing the bottom melt of the ice, further reducing the sea ice cover.

To the author's knowledge, the study of Döscher and Koenigk (2013) and the current work presented in this thesis are the only studies of RILEs occurring within an RCM. Moreover, the use of common atmospheric lateral boundary conditions (LBC) from a unique realization of a single AOGCM, ECHAM5/MPI-OM (hereafter ECHAM5), allowed to clearly identify the role played by the LBCs on the synchronicity of the events occurring around 2040 within each of the three RCAO climate projections. The results demonstrate the propagation of the driving model large-scale atmospheric circulation anomaly within the RCAO domain, triggering all the RILEs to occur within a short period, between 2036 and 2043. The differences in the oceanic LBCs and the internal variability within each projection altered the magnitude and geographic location of the maximum September sea ice cover loss.

Although the results show the important role of the large-scale atmospheric and oceanic circulations on the timing of the RILEs, a comparison of sea ice conditions between RCAO and ECHAM5 showed that the sensitivity of the sea ice cover is most likely related to

the simulated sea ice thickness by each model. Indeed, ECHAM5 generally simulates thicker ice compared to RCAO over the entire climate projection and no RILEs occurred within the ECHAM5 simulation.

Some deficiencies that could directly influence the sea ice cover and thickness in RCAO were identified. The atmospheric circulation in RCAO, as for many numerical models including ECHAM5, suffers from the quasi-permanent presence of an anticyclonic circulation over Beaufort Sea. This sea-level pressure bias causes erroneous forcing on the sea ice and is responsible for the displacement of the thickest sea ice towards the Eastern Siberian shores. This atmospheric circulation bias, combined with the presence of a closed oceanic boundary condition in Barents Sea, also reduces the sea surface height gradient between the Beaufort and Barents Seas, leading to an underestimation of the Bering Strait inflow. The Bering Strait inflow played an important role in the 2007 observed September sea ice cover minimum, and the enhanced heat transport by the Alaska current was most likely a trigger for a sea ice-albedo feedback over the Pacific Sector of the Arctic Ocean. Therefore, the underestimation of the Bering Strait inflow in RCAO deprives the region of heat transport and might help explain the absence of simulated RILEs of "Pacific Origin" within the climate projections, compared to recent observations.

The second chapter of this thesis focused on a different component of the Arctic climate, the study of near-surface permafrost and the interactions between the land surface and the atmosphere. Generally, numerical models employed for climate projections require improvements to adequately represent the high-latitude soil temperature and moisture regimes and the surface energy transfer between the land surface and the atmosphere. The first objective was to assess the sensitivity of near-surface permafrost and surface climate to soil and snow formulation, i.e. soil layer configuration and soil column depth, parameterization of the soil organic carbon (SOC) and changes in the formulation of the snow density-snow thermal conductivity relation using the Canadian LAnd Surface Scheme (CLASS) in stand-alone mode. The second objective was to assess the sensitivity of the surface climate, land-atmosphere interactions and near-surface permafrost sensitivity to land surface model formulation within the fifth-generation of the Canadian Regional Climate Model (CRCM5).

In accord with previous studies, results from the CLASS stand-alone experiment showed that a shallow soil configuration (3.5 m) combine to the zero-flux bottom boundary condition was not capable of realistically simulating the near-surface permafrost extent, leading to an overestimation of the annual cycle of soil temperatures. Deepening the soil column using only mineral soils, represented as percentage of sand and clay, did allow a greater area of near-surface permafrost to persist through summer, but the maximum annual thaw depth – the Active Layer Thickness (ALT) – was overestimated compared to observations and other modeling studies. The implementation of SOC, with its low thermal conductivity and relatively high heat content, reduced the summer soil temperatures by reducing the soil-atmosphere interactions. Decreasing the snow conductivity in parallel with the implementation of SOC tends to increase (decrease) the winter (summer) soil temperatures, decreasing temperature differences with observations.

The impact of the SOC implementation on the soil hydrological regime showed complex interactions between soil moisture, soil permeable depth, soil temperatures (hence permafrost) and the presence of peatlands. In summary, simulations with colder temperatures showed increased (decreased) surface runoffs (drainage) especially noticeable over peatlands. The regions where the ALT was shallower than the depth of the permeable soil column showed important signal since frozen ground does not allow infiltration and therefore no bottom drainage occurred over such regions.

The second section of this chapter addressed the ability of the fifth-generation Canadian Regional Climate Model (CRCM5) to represent the Arctic climate, near-surface permafrost and to evaluate the sensitivity of the surface climate to the implementation of the SOC parameterization. This was achieved by conducting CRCM5 experiments over the recent past period 1957–2008. The CRCM5 reproduced reasonably well the Arctic Climate despite some winter warm biases over Eastern Siberia and over the North American boreal forest. For precipitation and snow water equivalent, the CRCM5 biases were generally within the differences observed between different observation datasets and ERA-Interim reanalyses. The differences between various station-based datasets and reanalysis are an indication of the large uncertainties in measurements of the Arctic meteorological fields. For the CRCM5 experiments, similar conclusions to the CLASS stand-alone experiments were generally

noted for the simulated soil temperatures and hydrology in response to increased soil column depth, changes in snow conductivity and the implementation of SOC.

The surface turbulent heat fluxes showed important increase resulting from the SOC implementation, a direct response of the reduced ground heat flux. An important aspect of this work was to understand the response of the surface climate to the changes in the surface energy balance, in order to reduce the uncertainties raised by contradictory results obtained in previous studies by Lawrence and Slater (2008) and Rinke et al. (2008). Generally, the CRCM5 summer surface temperature response shows good agreement with results from both Lawrence and Slater (2008) and Rinke et al. (2008), with increases (decreases) in 2 m-air temperature where sensible (latent) heat flux increases. Despite significant changes in the surface turbulent fluxes, the 2 m-air temperature changes are generally not significant over the continuous permafrost region. Results from CRCM5 experiments show larger spatial heterogeneity compared to rather uniform signal presented in the two previous studies. The energy partitioning in the CRCM5 is directly related to the soil saturation and, over the Boreal forest, shows a distinct annual cycle with latent heat flux increasing in early summer when soil water is available from snow melt, a drying of the surface layers during the summer and marked increase in the sensible heat flux in mid-summer when soil moisture reaches minimal values.

The last section of the second chapter evaluated CRCM5's ability in reproducing the recent observed trends in the soil temperatures and sensitivity of the near-surface permafrost to changes in surface air temperatures. Although the simulated deepening trends are generally overestimated compared to observations, the experiments using the SOC generally shows smaller trends compared to the mineral formulation. This improvement in the simulated trends is a direct consequence of the insulative properties of the SOC and shows the necessity of including such parameterization into numerical models to increase the realism of the simulations. Two hypotheses were explored to explain the ALT trends: the presence of a warm bias in the CRCM5 climatology or an accelerated warming in the CRCM5 surface climate compared to observations. Results presented suggest that although the warming trends are slightly overestimated in the CRCM5 compared to observations, it is likely that the

CRCM5 warm bias also plays a significant role in the overestimation of the increasing ALT trends.

In summary, the implementation of SOC improves the representation of the thermal and moisture regimes of the Arctic soils. The CRCM5 shows great potential for the study of the Arctic region and its climate change. Despite the success in representing the Arctic climate and climate change, current model formulation needs further improvements. First and foremost, the SOC parameterization used in this study is based on the assumption (and approximation) that soil organic carbon is present in greater concentration near the surface rapidly decreasing with depth into the soil column. This assumption is reasonable in the Arctic and the observational data of the soil carbon concentration from IGBP-DIS represent only the first meter of the soil column. The vertical distribution of the SOC varies for other regions as shown by Jobaggy and Jackson (2000) and Lawrence and Slater (2008). Therefore, the author strongly recommends that the SOC parameterization, in its actual formulation, should solely be used over the high-latitude regions where Letts et al. (2000) peatland parameterization and approximation of the vertical distribution of SOC stays physically realistic.

Suggestions for future work

Although the RCAO version used in this study is no longer supported nor developed at the Swedish Meteorological and Hydrological Institute (SMHI), a version of RCA coupled to the Nucleus for European Modelling of the Ocean (NEMO) model is presently under development. The coupling was successful over the Baltic and North Seas and is currently in its final stage of evaluation over the Arctic. A study of RILEs using this new coupled system within a similar framework as presented in this study would be a valuable tool to understand the impact of using different ocean and sea ice model on the internal variability of the coupled system and help assess the relative role of the atmosphere and ocean.

The first chapter clearly demonstrated the influence of the LBCs from the driving AOGCM in triggering the RILEs. The logical next step would be to try to understand the relative contributions from the LBCs compared to the internal variability of the model itself.

To assess such question, it would be useful to perform an ensemble of regional climate projections using multiple AOGCMs to provide the LBCs to RCAO. In that sense, one could take advantage of the ongoing COordinated Regional Downscaling Experiment (CORDEX) that is presently underway, with the SMHI as one of the main participating institutions.

There are several limitations to the SOC parameterization implemented in the CRCM5, mostly related to the estimation of the soil carbon concentration and its horizontal and vertical distribution within the soil column. The spatial distribution of IGBP-DIS soil carbon assumes homogenous horizontal coverage of the model grid point if the soil carbon concentration is high enough to fill the first layer of the LSM. Although most of the modeling groups use this assumption, it does not take into account the large spatial variability and the natural distribution of soil carbon. In reality, the soil organic carbon tends to accumulate in valleys and peatlands while ridges or higher topographic areas tends to show lesser concentration of soil carbon. By assuming homogeneous distribution of the soil carbon, the model isn't capable of representing either regions adequately because of the large variability in the soil thermal and hydrologic properties. The author strongly recommends that future work should introduce updated databases of soil carbon and a measure of the fraction of the peatland coverage into CLASS using the already available "mosaic" option. The mosaic would allow distinguishing the fraction of both peatlands and region of lesser soil carbon concentration by defining different sub-grid soil column composition over each model grid point. The major challenge regarding this approach is access to such data that is, to the author's knowledge, available only for specific regions of the Arctic: over the Boreal forest of Canada (Figs C.1 and C.2) and over Western Siberia.

The improvements in spatial representation of the peatlands and other regions of moderate soil carbon concentration would further improve the realism of the simulation regarding the soil temperatures, hence permafrost and ALT, and hydrological variables required for multiple future projects within the Centre ESCER. Indeed, a more realistic representation of surface runoffs and drainage including the sub-grid scale heterogeneity might prove crucial inputs to the river-lake system actually being developed and implemented into CRCM5.

Similarly, subgrid-scale variability and the distinction between deep wetlands and other soils would also prove crucial in terrestrial ecosystem models for the evaluation of the carbon-climate feedbacks (Bohn et al. 2007). By allowing higher water table level within the soil column for wetlands (peatlands), soil organic carbon decomposition would result in methane emission while other dryer soils would release carbon dioxide, the former having a larger feedback on the greenhouse effect. Subgrid-scale heterogeneity would allow to better estimate future climate warming.

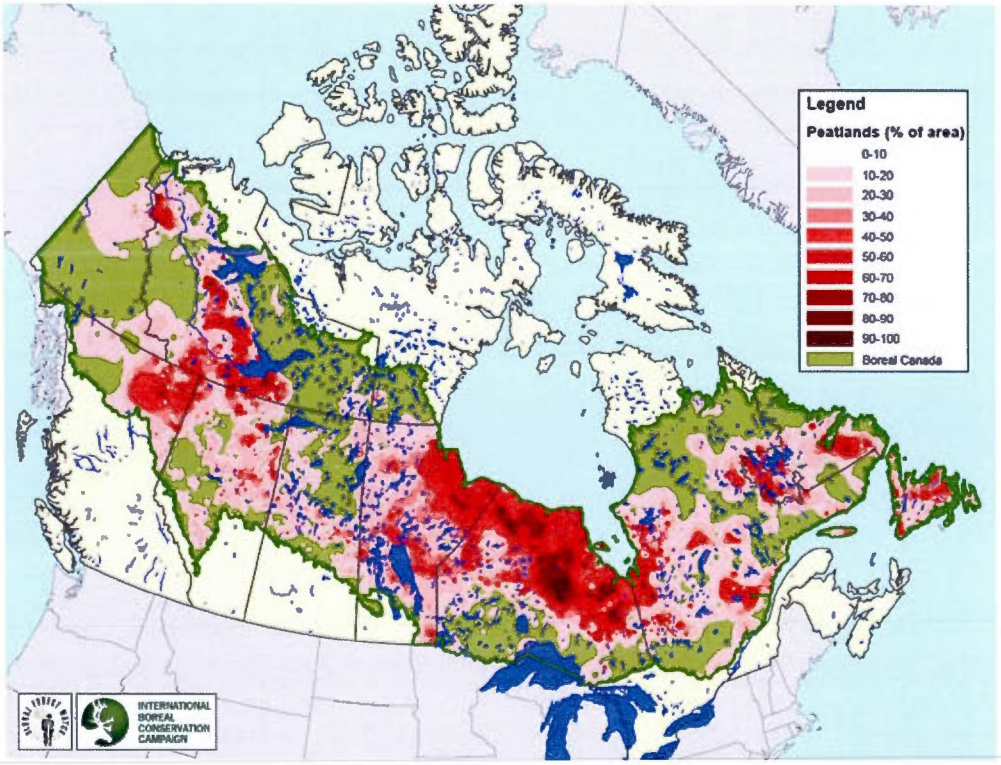

Figure C.1: Map of peatland coverage for the Canadian Boreal Forest. Data Source: Tarnocai, C., I.M. Kettles and B. Lacelle. 2002. Peatlands of Canada Database. Geological Survey of Canada, Open File 4002

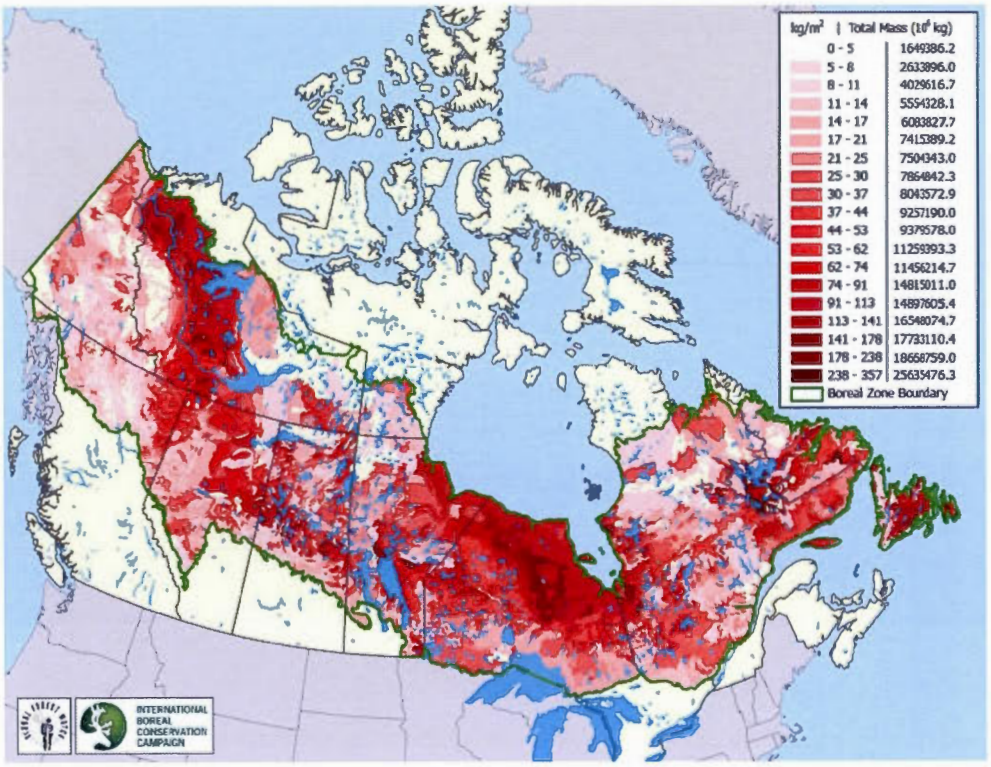

Figure C.2: Map of soil carbon density for the Canadian Boreal Forest. Data Source: Charles Tarnocai and Barbara Lacelle, Eastern Cereal and Oilseed Research Centre, Agriculture and Agri-Food Canada

REFERENCES

Alexeev, V. A., D. J. Nicolsky, V. E. Romanovsky, D. M. Lawrence. 2007. "An evaluation of deep soil configurations in the CLM3 for improved representation of permafrost.". *Geophys. Res. Lett.* 34(9): L09502.

Allard, M., B. Wang, J. A. Pilon. 1995. "Recent cooling along the Southern Shore of Hudson Strait, Quebec, Canada, Documented from Permafrost Temperature Measurements.". *Arctic and Alpine Res.* 27(2): 157-166.

AMAP, 1998.AMAP Assessment Report: Arctic Pollution Issues. Arctic Monitoring and Assessment Programme, Oslo, Norway, xii+859 pp.

Arctic Climate Impact Assessment (ACIA). 2004. "Impacts of a Warming Arctic: Arctic Climate Impact Assessment". New York: Cambridge Univ. Press

Bélair, S., J. Mailhot, C. Girard, P. Vaillancourt. 2005. "Boundary layer and shallow cumulus clouds in a medium-range forecast of a large-scale weather system". *Mon. Weather Rev.* 133:1938-1960.

Benoit R., J. Côté, J. Mailhot. 1989. "Inclusion of a TKE boundary layer parameterization in the Canadian regional finite-element model". *Mon. Weather Rev.* 117:1726-1750.

Berezovskaya, S., D. Yang, D. L. Kane. 2004. "Compatibility analysis of precipitation and runoff trends over the large Siberian watersheds". *Geophys. Res. Lett.*: L21502.

Beringer, J., A. H. Lynch, F. Stuart Chapin III, M. Mack, G. B. Bonan. 2001. "The Representation of Arctic Soils in the Land Surface Model: The Importance of Mosses". *J. of Climate* 14: 3324-3335.

Bitz, C. M., J. C. Fyfe, G. M. Flato. 2002. "Sea Ice Response to Wind Forcing from AMIP Models". *J. Clim.,* 15, 522-536.

Bourke, R. H., R. P. Garrett. 1987. "Sea ice thickness distribution in the Arctic Ocean". *Cold Regions Sci. Technol.* 13: 259-280.

Brown, J. 1998. *Circumpolar Active-Layer Monitoring (CALM) Program: Description and data. In Circumpolar active-layer permafrost system, version 2.0.* (ed.) M. Parsons and T. Zhang, (comp.) International Permafrost Association Standing Committee on Data Information and Communication. Boulder, CO: National Snow and Ice Data Center.

Brown, J., K. Hinkel, F. Nelson. 2003. *Circumpolar Active Layer Monitoring (CALM) Program Network.* Boulder, Colorado USA: National Snow and Ice Data Center.

Brown, J., O. J. Ferrians, Jr., J. A. Heginbottom, E.S. Melnikov. 1998 (revised February 2001). *Circum-arctic map of permafrost and ground ice conditions.* Boulder, CO: National Snow and Ice Data Center. Digital media.

Brown, R. D., B. Brasnett. 2010 (updated annually). *Canadian Meteorological Centre (CMC) Daily Snow Depth Analysis Data.* [indicate subset used]. Boulder, Colorado USA: National Snow and Ice Data Center.

Burke, E. J., R. Dankers, C. D. Jones, A. J. Wiltshire. 2013. "A retrospective analysis of pan Arctic permafrost using the JULES land surface model". *Clim. Dyn.*: 14. 10.1007/s00382-012-1648-x

Chapman, W. L., J.E. Walsh. 2007. "Simulations of Arctic temperatureand pressure by global coupled models". *J. Clim.* 20, 609–632.

Collins, W. D., C. M. Bitz, M. L. Blackmon, G. B. Bonan and co-authors. 2006. "The Community Climate System Model Version 3 (CCSM3)". *J. Clim.*, 19, 2122-2143

Comiso, J. C., C. L. Parkinson, R. Gersten, L. Stock. 2008. "Accelerated decline in the Arctic sea ice cover". *Geophys. Res. Lett.* 35. , doi:10.1029/2007GL031972.

Condron, A., P. Windsor, C. Hill, D. Menemenlis. 2009. "Simulated Response of the Arctic Freshwater Budget to Extreme NAO Wind Forcing". *J. Clim.* 22: 2422-2437.

Côté, J., S. Gravel, A. Méthot, A. Patoine, M. Roch, A. Staniforth. 1998 "The operational CMC-MRB Global Environmental Multiscale (GEM) model. Part I: design considerations and formulation". *Mon. Weather Rev.* 126:1373-1395.

Dankers, R., E. J. Burke, J. Price. 2011. "Simulation of permafrost and seasonal thaw depth in the JULES land surface scheme". *The Cryosphere* 5: 773-790. 10.5194/tc-5-773-2011

Dee, D.P., S. M. Uppala, A. J. Simmons and 33 co-authors. 2011. "The ERA-Interim reanalysis: configuration and performance of the data assimilation system". *Q. J. R. Meteorol. Soc.* 137: 553-597. 10.1002/qj.828

Delage, Y. 1997. "Parameterising sub-grid scale vertical transport in atmospheric models under statically stable conditions". *Bound. Layer Meteor.* 82:23-48.

Delage, Y., C. Girard. 1992 "Stability functions correct at the free convection limit and consistent for both the surface and Ekman layers". *Bound. Layer Meteor.* 58:19-31.

Déry, S. J., E. F. Wood. 2005. "Decreasing river discharge in northern Canada." *Geophys. Res. Let.* 32: L10401.

Déry, S. J., M. Stieglitz, E. C. McKenna, E.F. Wood. 2005. "Characteristics and Trends of River Discharge into Hudson, James, and Ungava Bays, 1964–2000". *J. Clim.* 18: 2540-2557.

Déry, S. J., M. A. Hernandez-Henriquez, J. E. Burford, E. F. Wood. 2009. "Observational evidence of an intensifying hydrological cycle in northern Canada". *Geophys. Res. Lett.* 36.

Deser, C., H. Teng. 2008. "Evolution of Arctic sea ice concentration trends and the role of atmospheric circulation forcing, 1979–2007". *Geophys. Res. Lett.* 35: L02504.

Deser, C., R. Tomas, M. Alexander, D. M. Lawrence. 2010. "The Seasonal Atmospheric Response to Projected Arctic Sea Ice Loss in the Late Twenty-First Century". *J. Clim.*, 23, 333-351. 10.1175/2009JCLI3053.1

DeWeaver, E., C. M. Bitz. 2006. "Atmospheric Circulation and Its Effect on Arctic Sea Ice in CCSM3 Simulations at Medium and High Resolution". *J. Clim.*, 19: 2415-2436.

Dickson, R. R., and Coauthors. 2000. "The Arctic Ocean response to the North Atlantic oscillation". *J. Clim.*, 13, 2671–2696.

Dickson, R., B. Rudels, S. Dye, M. Karcher, J. Meincke, I. Yashayaev. 2007. "Current estimates of freshwater flux through Arctic and subarctic seas". *Progress in Oceanography* 73: 210-230.

Döscher, R., T. Koenigk. 2013. "Arctic rapid sea ice loss events in regional coupled climate scenario experiments", *Ocean Sci.*, 9: 217-248, doi:10.5194/os-9-217-2013

Döscher, R., U. Willén, C. Jones, A. Rutgersson, H. E. M. Meier and co-authors. 2002. "The development of the regional coupled ocean-atmosphere model RCAO". *Boreal Environ. Res.*, 7, 183-192.

Döscher, R., K. Wyser, H. E. M. Meier, M. Qian, R. Redler. 2009. "Quantifying Arctic contributions to climate predictability in a regional coupled ocean-ice-atmosphere model". *Clim. Dyn.*, 10.1007/s00382-009-0567-y 1-20.

Fetterer, F., K. Knowles, W. Meier, M. Savoie. 2002 (updated 2011). *Sea Ice Index*, Boulder, Colorado USA: National Snow and Ice Data Center. Digital Media.

Francis, J. A., E. Hunter. 2006. "New Insight Into the Disappearing Arctic Sea Ice". *EOS* 87(46): 3.

Frauenfeld, O. W., J. Zhang. 2011. "An observational 71-year history of seasonally frozen ground changes in the Eurasian high latitudes". *Environ. Res. Lett.* 6. 10.1088/1748-9326/6/4/044024

Gilichinsky, D., R. Barry, S. Bykhovets, V. Sorokovikov, T. Zhang, S. Zudin, D. Fedorov-Davydov 1998. "A century of temperature observations of soil climate: methods of analysis and long-term trends". In: *Proceedings of the 7th international conference on permafrost*, 23–27

Gillet, N. P., M .P. Baldwin, M. R. Allen. 2003. "Climate change and the North Atlantic Oscillation". In: *The North Atlantic Oscillation: Climate Significance and Environmental Impacts*. 134: 193-209.

Gold, L. W. 1958. "Changes in a shallow snow cover subject to a temperate climate". *J. Glaciol.*, 3, 218-222.

Harvey, R., D. Houle, L. Duchesne, A. Bouffard, T. Logan. 2010. "Impact du couvert nival et des sols organiques sur la simulation des régimes thermiques et hydriques des sols de trois bassins forestiers du Québec à l'aide de CLASS". 3rd Ouranos Symposium, Montréal

Hilmer, M., T. Jung. 2000. "Evidence for a recent change in the link between the North Atlantic oscillation and Arctic sea ice export". *Geophys. Res. Lett.*, 27, 989–992.

Hinzman, L. D., D. L. Kane, R. E. Gieck, K. R. Everett. 1991. "Hydrologic and thermal-properties of the active layer in the Alaskan Arctic". *Cold Reg. Sci. Technol.* 19: 95-110.

Hinzman, L. D., N. D. Bettez, W. R. Boltonet and 32 co-authors. 2005. "Evidence and implications of recent climate change in Northern Alaska and other Arctic regions". *Clim. Change* 72(3): 251-298.

Holland, M. M., C. M. Bitz, B. Tremblay. 2006. "Future abrupt reductions in the summer Arctic sea ice". *Geophys. Res. Lett.*, 33, doi:10.1029/2006GL028024.

Holland, M. M., C. M. Bitz, L.-B. Tremblay, D. A. Bailey. 2008. "The Role of Natural Versus Forced Change in Future Rapid Summer Arctic Ice Loss". In: *Arctic Sea Ice Decline: Observations, Projections, Mechanisms, and Implications* (ed. E.T. DeWeaver, C.M. Bitz, and L.-B. Tremblay). Geophysical Monograph Series no.180, 133-150.

Hunke, E. C., J. K. Dukowicz. 1997. "An Elastic-Viscous-Plastic Model for Sea Ice Dynamics". *J. Phys. Oceanogr.*, 27, 1849-1867.

Hurrell, J. W., Y. Kushnir, and co-authors. 2003. "An Overview of the North Atlantic Oscillation". In: *The North Atlantic Oscillation: Climate Significance and Environmental Impact*. A. G. Union. 34: 1-35.

Intergov. Panel Clim. Change (IPCC). 2007. "Climate Change 2007: Synthesis report. Contribution of Working Groups I, II and III to the Fourth Assessment Report of the Intergovernmental Panel on Climate Change", ed. Core Writing Team, R. K. Pachauri, A. Reisinger. Geneva: IPCC. 104 pp.

Jones, C. G., U. Willén, A. Ullerstig, U. Hansson. 2004a. "The Rossby Centre Regional Atmospheric Climate Model Part I: Model Climatology and Performance for the Present Climate over Europe". *Ambio*, 33(4/5), 199-210.

Jones, C. G., K. Wyser, A. Ullerstig, U. Willén. 2004b. "The Rossby Centre Regional Atmospheric Climate Model Part II: Application to the Arctic Climate". *Ambio,* 33(4/5), 211-220.

Jones, P. D., D. E. Parker, T. J. Osborn, and K. R. Briffa. 2006. "Global and hemispheric temperature anomalies: Land and marine instrumental records, in Trends: A Compendium of Data on Global Change". http://cdiac.esd.ornl.gov/trends/temp/jonescru/jones.html, Carbon Dioxide Inf. Anal. Center, Oak Ridge Natl. Lab., U.S. Dep. of Energy, Oak Ridge, Tenn.

Jorgenson, M. T., Y. L. Shur, E. R. Pullman. 2006. "Abrupt increase in permafrost degradation in Arctic Alaska". *Geophys. Res. Lett.* 33: 4.

Jung, T., M. Hilmer. 2001. "The Link between the North Atlantic Oscillation and Arctic Sea Ice Export through Fram Strait". *J. Clim.* 14. 3932-3943

Kain, J. S., J. M. Fritsch. 1990. "A one-dimensional entraining/detraining plume model and application in convective parameterization". *J Atmos. Sci.* 47:2784-2802.

Karcher, M., R. Gerdes, F. Kauker, C. Köberle, I. Yashayaev. 2005. "Arctic Ocean change heralds North Atlantic freshening". *Geophys. Res. Lett.* 32: L21606.

Kay, J. E., T. L'Ecuyer, A. Gettelman, G. Stephens, C. O'Dell. 2008. "The contribution of cloud and radiation anomalies to the 2007 Arctic sea ice extent minimum". *Geophys. Res. Lett.* 35: L08503. doi:10.1029/2008GL033451.

Kjellström, E., L. Bärring, S. Gollvik, U. Hansson, C. Jones and co-authors. 2005. "A 140-year simulation of the European climate with the new version of the Rossby Centre regional atmospheric climate model (RCA3)". *SMHI reports meteorology and climatology,* RMK No. 108, 54.

Koenigk, T., R. Döscher, G. Nikulin. 2011. "Arctic future scenario experiments with a coupled regional climate model". *Tellus*, 63, 69-86.

Koldunov, N.V., D. Stammer, J. Marotzke. 2010. "Present-Day Arctic Sea Ice Variability in the Coupled ECHAM5/MPI-OM Model". *J. Climate,* 23, 2520-2543.

Koltzow, M. 2007. "The effect of a new snow and sea ice albedo schème on regional climate model simulations". *J. Geophys. Res.*, 112, D07110, doi:10.1029/2006JD007693.

Koven, C. D., B. Ringeval, P. Friedlingstein, and co-authors. 2011. "Permafrost carbon-climate feedbacks accelerate global warming". *PNAS* 108:14769–14774. doi:10.1073/pnas.1103910108

Kuo, H. L. 1965. "On formation and intensification of tropical cyclones through latent heat release by cumulus convection". *J Atmos. Sci.* 22:40– 63.

Kwok, R., D. A. Rothrock. 1999. "Variability of Fram Strait ice flux and North Atlantic oscillation". *J. Geophys. Res.*, 104, 5177–5189.

Kwok, R., G. F.Cunningham, M. Wensnahan, I. Rigor, H. J. Zwally, D. Yi. 2009. "Thinning and volume loss of the Arctic Ocean sea ice cover: 2003–2008". *J. Geophys. Res.* 114:C07005

Kwok, R., D. A. Rothrock. 2009. "Decline in Arctic sea ice thickness from submarine and ICESat records: 1958–2008". *Geophys. Res. Lett.* 36:L15501

Lawrence, D. M., A. G. Slater. 2008. "Incorporating organic soil into a global climate model". *Clim. Dyn.* 30: 145-160.

Lawrence, D. M., A. G. Slater, R. A. Tomas, M. M. Holland, C. Deser. 2008. "Accelerated Arctic land warming and permafrost degradation during rapid sea ice loss". *Geophys. Res. Lett.,* 35, doi:10.1029/2008GL033985.

Lawrence, D. M., A. G. Slater, V. E. Romanovsky, D. J. Nicolsky. 2008. "Sensitivity of a model

projection of near-surface permafrost degradation to soil column depth and representation of soil organic matter". *J. Geophys. Res.* 113: F02011. 10.1029/2007JF000883

Lemke, P., J. Ren, R. B. Alley, I. Allison and co-authors. 2007. "Observations: changes in snow, ice and frozen ground". *In: Climate change 2007: the physical science basis.* Contribution of Working Group I to the fourth assessment report of the intergovernmental panel on climate change [Solomon, S., D. Qin, M. Manning, Z. Chen, M. Marquis, K.B. Averyt, M. Tignor and H.L. Miller (eds.)]. Cambridge University Press, Cambridge, United Kingdom and New York, NY

Letts, M. G., N. T. Roulet, N. T. Comer, M.R. Skarupa, D.L. Verseghy. 2000. "Parametrization of Peatland Hydraulic Properties for the Canadian Land Surface Scheme". *Atmosphere-Ocean* 38(1): 141-160.

Li, J., H. W. Barker. 2005. "A radiation algorithm with correlated-k distribution. Part I: local thermal equilibrium". *J. Atmos. Sci.* 62:286-309.

Lindsay R. W., J. Zhang. 2005. "The thinning of Arctic sea ice, 1988–2003: have we passed a tipping point?". *J Clim.* 18:4879–4894

Longley, R. W. 1960. "Snow depth and snow density at Resolute, Northwest Territories". *J. Glaciol.*, 3, 733-738.

Luojus, K., J. Pulliainen, M. Takala, J. Lemmetyinen, C. Dersken, L. Wang. 2010. *Global Snow Monitoring for Climate Research - Snow Water Equivalent (SWE) product guide*, European Space Agency: 15. ESRIN Contract 21703/08/I-EC

Maslanik, J. A., C. Fowler, J. Stroeve, S. Drobot, H. J. Zwally, D. Yi, W. J. Emery. 2007. "A younger, thinner ice cover: increased potential for rapid, extensive ice loss". *Geophys Res Lett.* 34:L24501. doi:10.1029/2007GL032043

Markus T, J. C. Stroeve, J. Miller. 2009. "Recent changes in Arctic sea ice melt onset, freezeup, and melt season length". *J Geophys Res.* 114:C12024. doi:10.1029/2009JC005436

Mårtensson, S., H. E. M.Meier, P. Pemberton, J. Haapala. 2012. "Simulated long-term variability of ridged sea-ice in the Arctic Ocean using a coupled multi-category sea-ice ocean model". *J. Geophys. Res.*, 117, doi:10.1029/2010JC006936.

Martynov, A., R. Laprise, L. Sushama, K. Winger, L. Šeparović and B. Dugas. "Reanalysis-driven climate simulation over CORDEX North America domain using the Canadian Regional Climate Model, version 5: Model performance evaluation". *Clim. Dyn.* (in revision).

McClelland, J. W., S. J. Déry, B. J. Peterson, R. M. Holmes, E. F. Wood. 2006. "A Pan-Arctic Evaluation of Changes in River Discharge During the Latter Half of the 20th Century". *Geophys. Res. Lett.* 33: L06715.

McFarlane, N. A. 1987. "The effect of orographically excited gravity-wave drag on the circulation of the lower stratosphere and troposphere". *J. Atmos. Sci.* 44:1175-1800.

Meehl, G. A., W. M. Washington, B. D. Santer, W. D. Collins, J. M. Arblaster, A. Hu, D. M. Lawrence, H. Teng, L. E. Buja, and W. G. Strand. 2006. "Climate change in the 20th and 21st centuries and climate change commitment in the CCSM3". *J. Clim.*, 19: 2597 – 2616, doi:10.1175/JCLI3746.1.

Meier, H. E. M., R. Döscher, T. Faxén. 2003. "A multiprocessor coupled ice-ocean model for the Baltic Sea: application to salt inflow". *J. Geophys. Res.* 108(C8), 3273, doi:10.1029/2000JC000521.

Meier, H. E. M. 2007. "Modeling the pathways and ages of inflowing salt- and freshwater in the Baltic Sea". *Estuarine, Coastal and Shelf Science*, 71: 610-627.

Mellor, M. 1977. "Engineering properties of snow", *J. Glaciol.*, 19, 15-66.

Mitchell, T. D., P. D. Jones. 2005. "An improved method of constructing a database of monthly climate observations and associated high-resolution grids". *Int. J. Climatol.* 25:693-712. doi: 10.1002/joc.1181

Nelson, F. E. (ed). 2004. "Circumpolar active layer monitoring (CALM) Workshop". *Permaf. Periglac. Process* 15(2):99–188

Nghiem, S. V., I. G. Rigor, D. K. Perovich, P. Clemente-Colo, J. W. Weatherly, G. Neumann. 2007. "Rapid reduction of Arctic perennial sea ice." *Geophys. Res. Lett.* 34: L19504. doi:10.1029/2007GL031138

Nicolsky, D.J., V. E. Romanovsky, V. A. Alexeev, D. M. Lawrence. 2007. "Improved modeling of permafrost dynamics in a GCM land-surface scheme". *Geophys. Res. Lett.* 34: L08501. 10.1029/2007GL029525

O'Connor, F. M., O. Boucher and co-authors. 2010. "Possible role of wetlands, permafrost, and methane hydrates in the methane cycle under future climate: A Review". *Reviews of Geophysics* 48: 33.

Oelke, C., T. Zhang, M. C. Serreze, R. L. Armstrong. 2003. "Regional-scale modeling of soil freeze/thaw over the Arctic drainage basin". *J. Geophys. Res.* 108(D10): 19. 10.1029/2002JD002722

Oelke, C., T. Zhang, M. C. Serreze. 2004. "Modeling evidence for recent warming of the Arctic soil thermal regime". *Geophys. Res. Lett.* 31: 4. 10.1029/2003GL019300

Oleson, K. W., ßG.-Y. Niu, Z.-L. Yang, D. M. Lawrence, P. E. Thornton, P. J. Lawrence, R. Stöckli, R. E. Dickinson, G. B. Bonan, S. Levis, A. Dai, T. Qian. 2008. "Improvements to the Community Land Model and their impact on the hydrological cycle". *J. Geophys. Res.* 113: G01021, doi:10.1029/2007JG000563.

Osterkamp, T. E., J. C. Jorgenson. 2006. "Warming of permafrost in the Arctic National Wildlife Refuge, Alaska". *Permafr. Periglac. Proc.* 17:65–69

Osterkamp, T. E. 2007. "Characteristics of the recent warming of permafrost in Alaska". *J. Geophys. Res.* 112. 10.1029/2006JF000578

Pavelsky, T. M., J. Boé and co-authors. 2011. "Atmospheric inversion strength over polar oceans in winter regulated by sea ice". *Clim. Dyn.*, 36, 945-955, DOI 10.1007/s00382-010-0756-8.

Payette, S., A. Delwaide, M. Caccianiga, M. Beauchemin. 2004. "Accelerated thawing of subarctic peatland permafrost over the last 50 years". *Geophys. Res. Lett.* 18:L18208. doi:10.1029/2004GL020358

Peixoto, J., A. H. Oort. 1992. *Physics of Climate*. Springer-Verlag. New York.

Perovich, D. K., J. A. Richter-Menge, K. F. Jones, B. Light. 2008. "Sunlight, water, and ice: Extreme Arctic sea ice melt during the summer of 2007". *Geophys. Res. Lett.* 35: L11501. doi:10.1029/2008GL034007.

Peterson, B. J., J. McClelland, R. Curry, R. M. Holmes, J.E. Walsh, K. Aagaard. 2006. "Trajectory Shifts in the Arctic and Subarctic Freshwater Cycle". *Science* 313(1061).

Peterson, B. J., R. M. Holmes, J. W. McClelland, C. J. Vörösmarty, R. B. Lammers, A. I. Shiklomanov, I. A. Shiklomanov, S. Rahmstorf. 2002. "Increasing River Discharge to the Arctic Ocean". *Science* 298: 2171-2173.

Proshutinsky, A., R. Krishfield, D. Barber. 2009a. "Preface to special section on Beaufort Gyre

Climate System Exploration Studies: Documenting key parameters to understand environmental variability". *J. Geophys. Res.* 114: C00A08.

Rigor, I. G., J. M. Wallace, R. L. Colony (2002). "Response of sea ice to the Arctic Oscillation". *J. Clim.* 15: 2648-2663.

Rinke, A., P. Kuhry, K. Dethloff. 2008. "Importance of a soil organic layer for Arctic climate: A sensitivity study with an Arctic RCM". *Geophys. Res. Lett.* 35: L13709. 10.1029/2008GL034052

Romanovsky, V. E., T. E. Osterkamp. 2000. "Effects of unfrozen water on heat and mass transport processes in the active layer and permafrost". *Permafr. Periglac. Process.* 11: 219–239.

Royer, J. F., P. Samuelsson, S. Gollvik, A. Ullerstieg. 2006. "The land-surface scheme of the Rossby Centre regional atmospheric climate model (RCA3)". Norrköping, SMHI: 38.

Samuelsson, P., S. Gollvik, A. Ullerstieg. 2006. "The land-surface scheme of the Rossby Centre regional atmospheric climate model (RCA3)". *Report in meteorology 122*, SMHI. SE-60176, Norrköping, Sweden.

Schaefer, K., T. Zhang, L. Bruhwiler, A. P. Bareett. 2011. "Amount and timing of permafrost carbon release in response to climate warming". *Tellus B* 63:165–180. 10.1111/j.1600-0889.2011.00527.x

Schneider, U., A. Becker, P. Finger, A. Meyer-Christoffer, B. Rudolf, M. Ziese. 2011. *GPCC Full Data Reanalysis Version 6.0 at 0.5°: Monthly Land-Surface Precipitation from Rain-Gauges built on GTS-based and Historic Data.* 10.5676/DWD_GPCC/FD_M_V6_050

Schuur, E. A. G., J. Bockheim, J. G. Canadell, E. Euskirchen, C. B. Field, and co-authors. 2008. "Vulnerability of Permafrost Carbon to Climate Change: Implications for the Global Carbon Cycle". *BioScience* 58(8): 701-714.

Screen, J. A., I. Simmonds. 2010. "The central role of diminishing sea ice in recent Arctic temperature amplification." *Letters to Nature* 464(29): 1334-1337.

Semtner, A. J. J. 1976. "A Model for the Thermodynamics Growth of Sea Ice in Numerical Investigation of Climate". *J. Phys. Oceanogr.* 6(5), 379-389.

Serreze, M. C., R. G. Barry 2005. *The Arctic Climate System*. Cambridge, Cambridge University Press.

Serreze, M. C., A. P. Barrett. 2008. "The Summer Cyclone Maximum over the Central Arctic Ocean." *J. Clim.* 21: 1048-1065.

Serreze, M. C., A. P. Barrett, J. C. Stroeve, D. N. Kindig, M. M. Holland. 2009. "The emergence of surface-based Arctic amplification". *The Cryosphere* 3: 11-19.

Simmonds, I., C. Burke, K. Keay. 2008. "Arctic Climate Change as Manifest in Cyclone Behavior." *J. Clim.* 21: 5777-5796.

Smerdon, J. E., M. Stieglitz. 2006. "Simulating heat transport of harmonic temperature signals in the Earth's shallow subsurface: Lower-boundary sensitivities." *Geophys. Res. Lett.* 33: L14402. 10.1029/2006GL026816

Smith, L., Y. Sheng, G.M. MacDonald, L. D. Hinzman. 2005. "Disappearing Arctic Lakes". *Science* 308.

Solomon, S., D. Qin, M. Manning, Z. Chen, M. Marquis, K.B. Averyt, M. Tignor, H.L. Mill (Eds.): *Climate Change 2007: The Physical Science Basis*, Cambridge University Press, Cambridge, United Kingdom and New York, NY, USA, 2007.

Steele, M., R. Morley, W. Ermold. 2001. "PHC: A Global Ocean Hydrography with a High-Quality Arctic Ocean". *J. Clim.* 14, 2079-2087.

Steele, M., W. Ermold. 2004. "Salinity trends on the Siberian shelves." *Geophys. Res. Lett.* 31: L24308.

Steele, M., J. Zhang, W. Ermold. 2010. "Mechanisms of summertime upper Arctic Ocean warming and the effect on sea ice melt". *J. Geophys. Res.*, 115, C11004, 10.1029/2009JC005849

Stevens, D. P. 1991. "The Open Boundary Condition in the United Kingdom Fine-Resolution Antarctic Model". *J. Phys. Oceanogr.*, 21, 1494-1499.

Stroeve, J., M. M. Holland, W. Meier, T. Scambos, M. Serreze. 2007. "Arctic sea ice decline: Faster than forecast". *Geophys. Res. Lett.*, 34: L09501, 10.1126/science

Stroeve , J., V. Kattsov, A. Barrett, M.C. Serreze, T. Pavlova, M. M. Holland, W. N. Meier. 2012. "Trends in Arctic sea ice extent from CMIP5, CMIP3 and observations". *Geophys. Res. Lett.* 39: L16502.

Sturm, M., J. Holmgren, M. König, K. Morris. 1997 "The thermal conductivity of seasonal snow". *J. Glaciol.* 43:26-41.

Sundqvist, H., E. Berge, J. E. Kristjansson. 1989. "Condensation and cloud parameterization studies with a mesoscale numerical weather prediction model". *Mon. Weather. Rev.* 117:1641-1657

Tarnocai, C., J. G. Canadell, E. A. G. Schuur, P. Kuhry, G. Mazhitova, S. Zimov. 2009. "Soil organic carbon pools in the northern circumpolar permafrost region". *Global Biogeochem. Cyc.* 23: GB2023. 10.1029/2008GB003327, 2009.

Tremblay, L.-B. (2001). "Can we consider the Arctic Oscillation independently from the Barents Oscillation?". *Geophys. Res. Lett.* 28(22): 4227-4230.

Tsukernik, M., C. Deser, M. Alexander, R. Tomas. 2010. "Atmospheric forcing of Fram Strait sea ice export: a closer look". *Clim. Dyn.* 35: 1349-1360.

Undén, P., L. Rontu, H. Järvinen, P. Lynch, J. Calvo and co-authors. 2002. *HIRLAM-5 Scientific Documentation*. Norrköping, SMHI 144.

Uppala, S. M., P.W. Kållberg, A. J. Simmons, U. Andrae, da Costa and co-authors. 2005. "The ERA-40 re-analysis". *Quart. J. R. Meteorol. Soc.* 131: 2961-3012.

Verseghy, D. L. 1991. "CLASS – a Canadian land surface scheme for GCMs: I. Soil model". *Int. J. Climatol.* 11:111-133.

Verseghy, D.L., N.A. McFarlane, M. Lazare. 1993. "CLASS - A Canadian Land Surface Scheme for GMCs II. Vegetation Model and Coupled Runs". *Int. J. Climatol.* 13: 347-370.

Verseghy, D. L. 2008. "CLASS - The Canadian Land Surface Scheme (Version 3.4) – technical documentation (version 1.1)". *Internal report, Climate Research Division, Science and Technology Branch*, Environment Canada, 183p.

Wang, M., J. E. Overland, V. Kattsov, J. E. Walsh, X. Zhang, T. Pavlova. 2007. "Intrinsic versus Forced Variation in Coupled Climate Model Simulations over the Arctic during the Twentieth Century." *J. Clim.* 20.

Wang, J., J. Zhang, E. Watanabe, M. Ikeda, K. Mizobata, J. E. Walsh, X. Bai, B. Wu (2009), Is the Dipole Anomaly a major driver to record lows in Arctic summer sea ice extent?, Geophys. Res. Lett., 36, L05706, doi:10.1029/2008GL036706.

Wang, M., J.E. Overland. 2009. "A sea ice free summer Arctic within 30 years?". *Geophys. Res. Lett.*, L07502, 10.1029/2009GL037820.

Washington, W. M. , G. A. Meehl. 1996. "High-latitude climate change in a global coupled ocean-

atmosphere-sea ice model with increased atmospheric CO2". *J. Geophys. Res. Atmos.* 101:12795–801

Webb, D. J., A. C. Coward, B. A. De Cuevas, C. S. Gwilliam. 1997. "A Multiprocessor Ocean General Circulation Model Using Message Passing". *J Atmos. Oceanic Technol.*, 14, 175–183

Webb, R. W., C. E. Rosenzweig, E. R. Levine. 2000. *Global Soil Texture and Derived Water-Holding Capacities (Webb et al.). Data set.* Available on-line [http://www.daac.ornl.gov] from Oak Ridge National Laboratory Distributed Active Archive Center, Oak Ridge, Tennessee, U.S.A. 10.3334/ORNLDAAC/548.

Willmott, C. J., K. Matsuura. 1995. "Smart interpolation of annually averaged air temperature in the United States". *J. App. Meteorol.* 34:2577-2586.

Wilson, M. F., A. Henderson-Sellers. 1985 "A global archive of land cover and soils data for use in general circulation climate models". *J. Climatol.* 5:119–143

Woodgate, R., T. Weingartner, R. Lindsay. 2010. "The 2007 Bering Strait oceanic heat flux and anomalous Arctic sea-ice retreat." *Geophys. Res. Lett.* 37.

Yoshikawa, K., L. Hinzman. 2003. "Shrinking thermokarst ponds and groundwater dynamics in discontinuous permafrost". *Permafr. Periglac. Process.* 14(2), 151–160.

Zadra, A., D. Caya, J. Côté, B. Dugas, C. Jones, R. Laprise, K. Winger, L.-P. Caron. 2008 "The next Canadian regional climate model". *Phys. Canada* 64:74-83.

Zhang, T., R. G. Barry, K. Knowles, J. A. Heginbottom, J. Brown. 1999. "Statistics and characteristics of permafrost and ground-ice distribution in the Northern Hemisphere". *Polar Geogr.* 23(2):132–154

Zhang, T., R. Barry, D. Gilichinsky. 2001. *Russian historical soil temperature data.* Digital media. National Snow and Ice Data Center, Boulder

Zhang, T. 2005. "Influence of the seasonal snow cover on the groundthermal regime: an overview". *Rev. Geophys.* 43 RG4002